UNIVERSITY OF CALIFORNIA
SANTA CRUZ

AGB STARS IN THE DISK, SATELLITES, AND HALO OF M31

A dissertation submitted in partial satisfaction of the
requirements for the degree of

Doctor of Philosophy

in

ASTRONOMY & ASTROPHYSICS

by

Katherine M. Hamren

June 2016

The Dissertation of Katherine M. Hamren
is approved:

_____
Professor Puragra GuhaThakurta, Chair

_____
Professor Constance Rockosi

_____
Professor Graeme Smith

_____
Dean Tyrus Miller
Vice Provost and Dean of Graduate Studies

Table of Contents

List of Figures

List of Tables

Abstract

AGB Stars in the Disk, Satellites, and Halo of M31

by

Katherine M. Hamren

Asymptotic giant branch (AGB) stars are simultaneously one of the most important and least well understood phases of stellar evolution. Luminous, red, AGB stars are excellent tracers of kinematical and morphological structure, and track the presence of intermediate age populations. In addition, they contribute significantly to the near-infrared flux and gas/dust budgets of galaxies. As a result, they are essential for studying galaxies in both the local and distance universe. However, their observable properties depend on complicated physical processes, including dredge-up, dust production, and stellar pulsations. As a result, they are difficult to model on both the individual and population-level scales. Homogenous samples of AGB stars are necessary to calibrate ever improving models. In this thesis I use data from the Spectroscopic and Photometric Landscape of Andromeda's Stellar Halo survey to identify and characterize clean, homogenous samples of carbon- and oxygen-rich AGB stars (carbon stars and M-stars, respectively) in the disk, satellites and halo of the Andromeda galaxy (M31). Using these stars, I constrain the ratio (C/M) of carbon- to oxygen-rich in fields throughout the M31 system, compare the AGB stars to their observationally similar contaminants (extrinsic carbon stars and oxygen-rich red giant branch stars), and discuss major physical properties (color, temperature, metallicity, dust production, and variability).

Let's think the unthinkable, let's do the undoable. Let us prepare to grapple with the ineffable itself, and see if we may not eff it after all.

–Douglas Adams–

Acknowledgments

The text of this dissertation includes material previously published (or soon to be published) in astronomical journals. Chapter 2 was published as Hamren et al., ApJ 2015, 810, 60, in collaboration with members of both the SPLASH and PHAT teams. Chapter 3 was submitted to the Astrophysical Journal in February, 2016. The data used in this thesis were taken by members of the SPLASH and PHAT teams, led by Puragra GuhaThakurta (SPLASH spectroscopy), Steven Majewski (SPLASH photometry), and Julianne Dalcanton (PHAT photometry). The observations were conducted by (in alphabetical order) Rachael Beaton, Claire Dorman, Marla Geha, Karoline Gilbert, Puragra GuhaThakurta, Jason Kalirai, Steven Majewski, and Erik Tollerud. I led the analysis and presentation of the AGB stars in these data, and am the principal investigator of the papers that comprise this thesis. This research was conducted with support from the people listed above as well as Bernhard Aringer, Martha Boyer, Julianne Dalcanton, Leo Girardi, Dylan Gregersen, Alexia Lewis, Constance Rockosi, Anil Seth, Graeme Smith, Elisa Toloba and Benjamin Williams. I thank all of these collaborators for their help and hard work.

Chapter 1

Introduction

The asymptotic giant branch (AGB) is simultaneously one of the most important and one of the most uncertain phases of stellar evolution. Despite playing a major role in the integrated light of galaxies, the production of gas and dust, and the chemical enrichment of the interstellar medium (ISM), neither the interior physical processes nor the population properties of AGB stars are completely understood.

1.1 The physics of AGB stars

The asymptotic giant branch (AGB) is the final evolutionary stage for low to intermediate mass ($0.8 < M_{\odot} < 8$) stars. It can be described as two phases, the early (E-AGB) phase followed by the thermally pulsating (TP-AGB) phase. They begin once a star on the red giant branch (RGB) has exhausted the He in its core.

The E-AGB phase begins with He-burning in a shell around the inert CO core and an outer H-burning shell. The He-burning causes the He-rich intershell region to expand, which

lowers the temperature of the H-burning shell until it is extinguished. At this point, the 'double mirror' effect caused by two concentric shells disappears, and the entire stellar envelope expands. In stars with $M > 4M_{\odot}$, the outer convective envelope can extend below the now inert H-shell, bringing He-enriched material to the surface. This is known as the second dredge-up (2DU). In stars of all masses, the He-burning shell continues to expand until the H-burning shell is reignited. This ends the E-AGB phase.

The TP-AGB stage is characterized by both the H and the He shells burning at uneven and unstable rates, giving rise to thermal pulses. The H-burning shell adds mass to the intershell region, which in turn increases the pressure and temperature on the now geometrically thin He-burning shell. At some critical temperature, the He-burning shell ignites in a flash and a thermal pulse begins. This release of energy expands the intershell region, extinguishing the H-shell and mixing the intershell material. Without the H-burning shell to act as a barrier, the outer convective envelope can penetrate into the intershell region, dredging up the enriched material. This is referred to as the third dredge-up (3DU), and occurs whether or not there had been a 2DU event. Eventually (after $\sim$ 100 years), the H-burning shell re-ignites, and the process begins again.

This thermal pulse cycle has an important effect on the chemical makeup of the star. The intershell region is primarily composed of He and ^{12}C , while the outer convective atmosphere contains a great deal of ^{16}O . The 3DU brings ^{12}C to the surface, where it binds with ^{16}O to form CO. Over successive dredge ups, all free ^{16}O is caught up in CO, and additional ^{12}C remains free. The star can thus transition from an M-star with C/O$<$ 1 and oxygen absorption features in its observable spectrum to a carbon star with C/O$>$ 1 and carbon absorption features

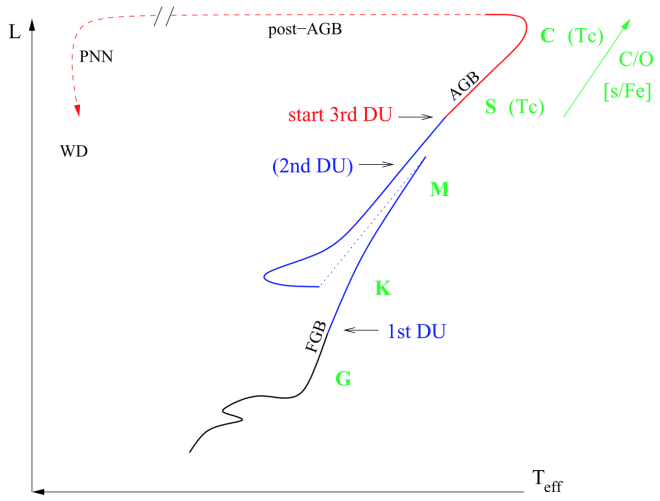

Figure 1.1: Post-main sequence HR diagram[2], annotated with the dredge up events discussed in the text, as well as the spectral type of the star (G, K, M, S, C) in green. The start of the TP-AGB phase is marked as a shift from blue to red, and the end of the AGB phase is marked as a shift from solid to dashed line.

in its observable spectrum. This transition occurs faster for metal-poor stars, in which there is less oxygen and the 3DU is more efficient (Karakas *et al.*, 2002).

While undergoing 3DU on the TP-AGB phase, these stars also undergo a tremendous amount of mass loss. The stellar winds that drive this mass loss are believed to occur due to a combination of dynamic pulsations and radiation pressure on dust that condenses in the relatively cool stellar atmospheres. TP-AGB stars can lose up to $10^{-5} M_{\odot}$ per year (Srinivasan *et al.*, 2009; Boyer *et al.*, 2011). This means that the lifetime of a TP-AGB star is typically governed by its mass-loss rate rather than the rate at which the core mass increases (Marigo and Girardi, 2001).

Figure 1.1 illustrates the effect that the processes outlined above have on the temper-

[2]Figure from lecture notes written by Dr. Onno Pols, available at http://www.astro.ru.nl/~onnop/education/stev_utrecht_notes/

ature and luminosity of a $1M_{\odot}$ star. While the precise position on the H-R diagram changes with mass and metallicity, E-AGB stars are typically found in the same temperature-luminosity space (or color-magnitude space) as red giant branch (RGB, or in Figure 1.1, FGB) stars. TP-AGB stars are typically more luminous than the tip of the red giant branch (TRGB). Stars just beginning the TP-AGB phase and stars experiencing a thermal pulse driven luminosity dip may be fainter than the TRGB, but contamination of TP-AGB stars in the RGB is modeled to be at most a few percent (Girardi *et al.*, 2010; Rosenfield and Marigo, 2014), even at low metallicity.

1.2 Observations of AGB Stars in the Local Group

The earliest work on AGB stars in the Local Group relied on prisms, gratings, and GRISMS to identify carbon stars by their spectra (e.g., Aaronson *et al.*, 1982; Azzopardi *et al.*, 1985; Azzopardi *et al.*, 1986; Kontizas *et al.*, 2001). These surveys focused on locating carbon stars, and proving that while they were not seen in globular clusters, they were not uncommon in satellite galaxies.

The development of the four-band photometry system (FBPS; Richer *et al.*, 1984; Aaronson *et al.*, 1985; Richer and Crabtree, 1985; Cook *et al.*, 1986) opened up the Local Group to more efficient AGB surveys. This system employs four filters; two broad-band filters to establish a color baseline (e.g., $V-I$, $R-I$), and two narrow-band filters centered on the optical CN and TiO bands (8120.5 and 7778.4Å, respectively). CN–TiO color can separate cool M- and C-stars very efficiently, and so FBPS has been used to identify and differentiate these stars in many galaxies throughout the Local Group (e.g., Albert *et al.*, 2000; Nowotny *et al.*,

2001; Letarte *et al.*, 2002; Cioni and Habing, 2005; Brewer *et al.*, 1995, and subsequent papers in these surveys). The authors used the identified AGB populations to compute the ratio (C/M) of C- to M-type AGB stars, and showed that it correlates with satellite metallicity (Battinelli and Demers, 2005, and references therein). However, these surveys suffer from two issues. The first is that the intense mass-loss on the AGB renders many AGB stars invisible in the optical (Boyer *et al.*, 2009), and the second is that photometric surveys cannot distinguish between distant M-giants and foreground M-dwarfs.

As observational capabilities in the near to far-infrared increased, observations of AGB stars shifted into the NIR and MIR. Broad-band JHK photometry (occasionally adding an optical magnitude) has been used to identify and distinguish between different AGB stars (e.g., Cioni and Habing, 2005; Cioni *et al.*, 2006; Davidge, 2005; Groenewegen, 2006; Whitelock *et al.*, 2006; Sohn *et al.*, 2006; Menzies *et al.*, 2007; Mauron, 2008; Sibbons *et al.*, 2012). The C/M ratios derived from these surveys allowed the visualization of spatial variations in metallicity (Cioni, 2009) and a deeper understanding of the carbon star luminosity function CSLF, and a quantification of the contribution of TP-AGB stars to the integrated NIR light of galaxies (Melbourne *et al.*, 2012; Melbourne and Boyer, 2013).

The launch of the *Spitzer Space Telescope* made it possible to observe AGB stars in the infrared without complication from the Earth's atmosphere. Thorough surveys have been conducted of galaxies in the Local Group (Blum *et al.*, 2006; Boyer *et al.*, 2011; Jones *et al.*, 2015) searching for dust-enshrouded AGB stars. These surveys have identified new types of AGB stars, including "extreme" stars (x-AGB; Boyer *et al.*, 2011, 2014) likely undergoing a "superwind" phase, and stars with anomalous abundances (a- or aO-AGB; Boyer *et al.*, 2015).

These surveys have quantified typical mass-loss rates as a function of composition (C versus O; Srinivasan *et al.*, 2009; Riebel *et al.*, 2012) and metallicity (Boyer *et al.*, 2012; Sloan *et al.*, 2012).

In parallel with these primarily photometric surveys, increasing numbers of AGB spectra have also been obtained. Spectra have constrained carbon isotopic ratios (Abia and Isern, 1997, 2000; Lebzelter *et al.*, 2008) and peculiar abundances (Brewer *et al.*, 1996), and several databases now exist (Fluks *et al.*, 1994; Lanï£¡on and Wood, 2000; Chen and Shan, 2012; Zhong *et al.*, 2015) for comparison to ever-improving models.

1.3 Outstanding Questions

Despite this wealth of observations, there are still a number of outstanding questions that impede our understanding of both the AGB stars themselves and other astronomical subfields that rely heavily on AGB stars (e.g., Maraston, 2005; Conroy, 2013).

There are uncertainties at both the level of individual stars and the level of the AGB population as a whole. On the small scale, a number of the internal AGB processes are poorly understood. This includes their lifetimes (Girardi *et al.*, 2010; Rosenfield and Marigo, 2014), the dependence of the M- to C-star transition on metallicity (Boyer *et al.*, 2013; Karakas, 2014), the initial-final mass relation (Kalirai *et al.*, 2014), and the details of dust production and mass loss for C-, M-, and x-AGB stars. On the global scale, the contribution of AGB stars to a galaxy's dust budget (Matsuura *et al.*, 2009; Srinivasan *et al.*, 2016) and integrated NIR flux (Melbourne *et al.*, 2012; Girardi *et al.*, 2013; Salaris *et al.*, 2014) are also not well constrained.

These uncertainties stem from the fact that these stars are extraordinarily difficult to model. Even dust-free, hydrostatic models require thorough treatment of complicated opacities and dredge-up processes (Loidl and Lan, 2001; Aringer *et al.*, 2009; Aringer *et al.*, 2016). As the models become more realistic, they must take into account deviations from spherical symmetry, pulsations, dust production, and stellar winds (Nowotny *et al.*, 2011, 2013). Even with all these processes properly accounted for, the calibration of the TP-AGB models to match a particular set of observations often does not generalize to other environments (Marigo *et al.*, 2013, and references therein).

In addition to improved AGB models, large datasets of homogenous observations in different environments are necessary to tackle some of these questions.

1.4 Why M31?

The M31 system is a perfect laboratory for studying stellar populations. The disk of M31 is the only Milky Way-like environment that we can observe in its entirety while still resolving individual stars. It is comparatively metal-rich, with age and metallicity gradients (Sanders *et al.*, 2012; Gregersen *et al.*, 2015) and a complicated star formation history (Lewis *et al.*, 2015; Williams *et al.*, 2015). The halo of M31 features remnants of historical accretion events (Kalirai *et al.*, 2006a; Gilbert *et al.*, 2007, 2009a) on top of the smooth, virialized background (Guhathakurta *et al.*, 2005; Gilbert *et al.*, 2012). Within the halo there are (as of this writing) 31 identified satellite galaxies, including dwarf spheroidals (dSphs), dwarf ellipticals (dEs) and the Local Group's only compact elliptical (cE). The satellites exhibit a range of sizes,

metallicities, star formation histories, and miscellaneous quirks.

Recent large-scale surveys have opened up the vast majority of the M31 system to thorough, uniform analysis. The Spectroscopic and Photometric Landscape of Andromeda's Stellar Halo (SPLASH; Guhathakurta *et al.*, 2005, 2006; Gilbert *et al.*, 2006, 2012; Dorman *et al.*, 2013; Dorman *et al.*, 2015) has obtained optical photometry and moderate-resolution optical spectra in $\sim$ 100 fields across the satellites, halo, and disk of M31. SPLASH spectroscopy has been obtained using the DEIMOS multi-object spectrograph on the Keck II 10-m telescope. The disk of M31 has also been imaged by the Panchromatic Hubble Andromeda Treasury (PHAT; Dalcanton *et al.*, 2012), one of the largest HST programs to date. Combining these surveys gives us six-filter (UV, optical, and NIR) PHAT photometry of $\sim$ 117 million stars in the disk of M31, and state-of-the-art spectra and photometry of 25000 stars in the disk, halo, and satellites.

This represents an unprecedented amount of data on M31, a dataset that allows for a more comprehensive look at the TP-AGB population than has yet been attempted. Until now, observational coverage of AGB stars in M31 has been patchy. In the disk, crowding and distance mean work on the AGB population has been limited to relatively shallow ground-based surveys (Brewer *et al.*, 1995, 1996; Battinelli and Demers, 2005), Hubble Space Telescope (HST) pencil beams (Stephens *et al.*, 2003; Boyer *et al.*, 2013), or adaptive-optics assisted observation (Davidge, 2001, 2005). Work on the satellites has been equally inconsistent. Some larger, brighter examples have been probed in great detail (for example, the dEs; Nowotny *et al.*, 2003; Battinelli and Demers, 2004b,a; Jung *et al.*, 2012). Others have been surveyed photometrically (Harbeck *et al.*, 2004, 2005), but conclusions have been hampered by the difficulty in

distinguishing M31 giants from foreground MW dwarfs. Many dwarfs have only been verified in the last few years (Tollerud *et al.*, 2013), and so have escaped scrutiny altogether. AGB observations in the halo have been largely serendipitous (Koch and Rich, 2010).

1.5 Chapter Descriptions

In this thesis, I use spectroscopic and photometric data from the SPLASH survey to compile and characterize a clean and homogenous samples of C- and M-type AGB stars throughout the M31 system. Chapters 2 and 3 were originally prepared for submission to astronomical journals. They are presented here in their original format.

1.5.1 The C/M ratio in the disk of M31

In Chapter 2 I explore the ratio (C/M) of carbon-rich to oxygen-rich TP-AGB stars in the disk of M31 using a combination of moderate-resolution optical spectroscopy from the SPLASH survey and six-filter *Hubble Space Telescope* photometry from the PHAT survey. Carbon stars were identified spectroscopically by comparison against a suite of MW templates. Oxygen-rich M-stars were identified using three different photometric definitions designed to mimic, and thus evaluate, selection techniques common in the literature. I calculate the C/M ratio as a function of galactocentric radius, present-day gas-phase oxygen abundance, stellar metallicity, age (via proxy defined as the ratio of TP-AGB stars to red giant branch, RGB, stars), and mean star formation rate over the last 400 Myr. I find statistically significant correlations between log(C/M) and all parameters. These trends are consistent across different

M-star selection methods, though the fiducial values change. Of particular note is our observed relationship between log(C/M) and stellar metallicity, which is fully consistent with the trend seen across Local Group satellite galaxies. The fact that this trend persists in stellar populations with very different star formation histories indicates that the C/M ratio is governed by stellar properties alone.

1.5.2 Carbon stars in the satellites and halo of M31

In Chapter 3 I spectroscopically identify a sample of carbon stars in the satellites and halo of M31 using moderate-resolution optical spectroscopy from the SPLASH survey. I present the photometric properties of my sample of 41 stars, including their brightness with respect to the tip of the red giant branch (TRGB) and their distributions in various color-color spaces. This analysis reveals a bluer population of carbon stars fainter than the TRGB and a redder population of carbon stars brighter than the TRGB. I then apply Principal Component Analysis (PCA) to determine the sample's eigenspectra and eigencoefficients. Correlating the eigencoefficients with various observable properties reveals the spectral features that trace effective temperature and metallicity. Putting the spectroscopic and photometric information together, I find the carbon stars in the satellites and halo of M31 to be minimally impacted by dust and internal dynamics. I also find that while there is evidence to suggest that the sub-TRGB stars are extrinsic in origin, it is also possible that they are are particularly faint members of the asymptotic giant branch.

1.5.3 M-giants in the satellites and halo of M31

In Chapter 4 I spectroscopically identify a sample of M-giants in the satellites and halo of M31. I develop a random forest to classify spectra in the SPLASH survey as M-type stars, and then use SPLASH photometry to separate the resulting sample of 533 M-giants into those on the AGB and those on the RGB. I present the spatial distribution of these stars, and calculate the C/M ratio in those fields which also harbor carbon stars. The photometric and spectroscopic properties of the M-giant sample allow me to evaluate the stars' effective temperatures ($T_{\rm eff}$), variability and mass loss, and metallicity. This analysis highlights uncertainties in the models and empirical relationships that are often used to characterize cool stars, including inconsistencies between different determinations of spectral type, and the unreliability of the CaT in AGB stars or samples that contain AGB stars. I also apply PCA to attempt to identify spectroscopic methods of distinguishing AGB and RGB stars. PCA analysis reveals that the major differences between AGB and RGB stars are at the population level, and that while small differences in spectra are prevalent they are extremely difficult to interpret physically.

Chapter 2

The C/M Ratio in the Disk of M31

2.1 Introduction

Asymptotic giant branch (AGB) stars are important for understanding galaxies' integrated light and resolved stellar populations. They are major contributors of near-infrared (NIR) flux, contributing $\sim 20\%$ of a galaxy's NIR light in the local universe, and up to 70% at high-redshift (Boyer *et al.*, 2011; Melbourne *et al.*, 2012; Conroy, 2013; Melbourne and Boyer, 2013; Villaume *et al.*, 2015). They also remain one of the least understood phases of stellar evolution, with outstanding questions regarding calibration of the thermally-pulsating AGB (TP-AGB) phase, dredge-up, opacities and mass loss (e.g., Marigo *et al.*, 2013, and references therein).

AGB stars are broadly characterized by whether their ae.g.,]tmospheres contain excess carbon or excess oxygen. Stars with free oxygen (C/O < 1) are deemed M-type AGB stars, or M-stars. These stars undergo the third dredge-up (3DU), which brings newly formed

carbon and s-process elements to the surface. This pollution alters the atmospheric chemistry, and causes the star to transition first to S-type (C/O$\sim$ 1) and finally to C-type (C/O $>$ 1). The C-type stars with free carbon are also known as carbon stars.

Because the transition from M-star to C-star depends on metallicity and stellar mass, the ratio (C/M) of carbon-rich to oxygen-rich AGB stars is a useful tool for studying the evolution of TP-AGB stars, and the galactic environment in which the stars formed. For example, C/M ratios obtained for galaxies throughout the Local Group (e.g., Cioni and Habing, 2003; Battinelli and Demers, 2004b; Cioni *et al.*, 2008; Battinelli and Demers, 2009; Boyer *et al.*, 2013), have been used to constrain models of AGB stars (Karakas, 2014) and metallicity gradients of the host galaxies (e.g., Cioni *et al.*, 2008; Feast *et al.*, 2010).

With its complicated star formation history (SFH) and metal-rich environment, M31 is a particularly powerful laboratory for continuing this work. Due to its size and distance, past work on the AGB population in M31 has been limited to relatively shallow ground-based surveys (Brewer *et al.*, 1995, 1996; Battinelli and Demers, 2005), Hubble Space Telescope (HST) pencil beams (Stephens *et al.*, 2003; Boyer *et al.*, 2013), or adaptive-optics assisted observation (Davidge, 2001, 2005). Fortunately, recent large-scale surveys have opened up the AGB stars of M31 to the same scrutiny as elsewhere in the Local Group.

In this work, we use data from both the Panchromatic Hubble Andromeda Treasury (PHAT; Dalcanton *et al.*, 2012) and the Spectroscopic and Photometric Landscape of Andromeda's Stellar Halo (SPLASH; Guhathakurta *et al.*, 2006) surveys. The pairing of HST photometry and Keck spectroscopy across the disk of M31 allows us to not only distinguish carbon-rich and oxygen-rich AGB stars, but also to evaluate the C/M ratio as a function of a

wide variety of parameters. We can, for the first time, self-consistently evaluate the C/M ratio across a variety of age, metallicity and SFH environments.

Section 2.2 describes our data, including the surveys from which we obtain our spectra and photometry, and our method of distinguishing between carbon-rich and oxygen-rich AGB stars. Section 2.3 examines the effect of different possible AGB classifications on the C/M ratio. Section 2.4 presents the resulting C/M ratios as a function of radius, metallicity, and star formation history (SFH). Section 2.5 discusses these results and possible biases.

2.2 Data

2.2.1 Photometry

The photometry used in this work is from the PHAT survey, which resolved $\sim$ 117 million stars in the disk of M31 (Williams *et al.*, 2014). Images were taken with UV ($F275W$ and $F336W$), optical ($F475W$ and $F814W$) and NIR ($F110W$ and $F160W$) filters, using HST WFC3/UVIS, ACS/WFC and WFC3/IR, respectively. The photometry was performed using DOLPHOT (Dolphin, 2002), and "good star" (gst) cuts were made using the signal-to-noise (S/N), sharpness, and crowding parameters output by the photometry pipeline. For further details, we refer the reader to Dalcanton *et al.* (2012) and Williams *et al.* (2014).

When comparing the C/M ratio to the stellar metallicity in § 2.4.2.2 and the age proxy in § 2.4.3, we use the single camera ACS photometry (Dalcanton *et al.*, 2012) further corrected for bias, completeness, and foreground extinction by Gregersen *et al.* (2015, hereafter G15). Photometric bias is caused by the effect of unresolved and bright stars in crowded regions,

which leads stars to appear brighter and with a color closer to the mean color of the region. Completeness, the fraction of stars observed vs. the number of stars present, has a color dependent effect on the stellar population. While completeness does not impact the magnitude of a star, it does impact quantities derived from the population (e.g. median metallicity). To correct for foreground extinction, G15 assume $A_V = 0.17$ mag. For further details on these corrections, we refer the reader to the original paper.

2.2.2 Spectroscopy

The complete spectroscopic observations are documented elsewhere (e.g., Guhathakurta *et al.*, 2006; Gilbert *et al.*, 2009a; Dorman *et al.*, 2012; Gilbert *et al.*, 2012; Dorman *et al.*, 2015), but those specific to the disk are briefly summarized here.

Our spectroscopic targets were selected from optical photometry. The majority ($\sim$ 63%) were targeted using HST photometry from PHAT. The rest were targeted using CFHT i' photometry (discussed in Gilbert *et al.*, 2012). In all cases, stars were selected to be isolated, without close, bright neighbors (see Dorman *et al.*, 2012, for details).

The disk dataset contains 10,619 optical spectra taken with the DEIMOS spectrograph (Faber *et al.*, 2003) on the Keck II 10-m telescope. Approximately half (5323) of these spectra were observed with the 1200 line mm^{-1} grating, which has a dispersion of 0.33Å pixel^{-1} and a central wavelength of 7760Å. The rest (5296) were taken with the 600 line mm^{-1} grating, which has a dispersion of 0.65Å pixel^{-1} and a central wavelength of 7000Å.

The spectra were reduced using the `spec2d` and `spec1d` software modified for the SPLASH survey (Cooper *et al.*, 2012; Newman *et al.*, 2013). The `spec2d` routine firsts

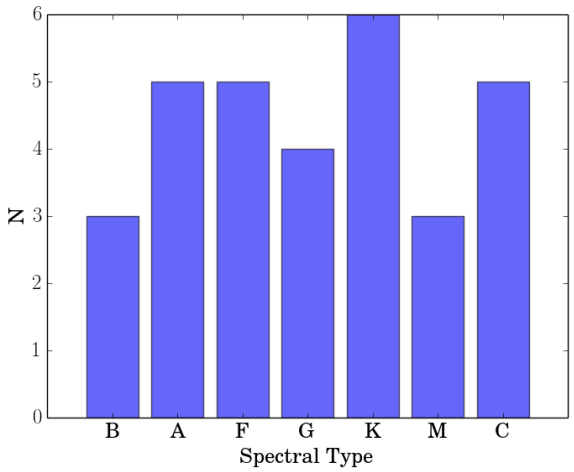

Figure 2.1: Distribution of spectral types represented in our suite of high S/N Milky Way template spectra. “C" denotes carbon stars.

extracts a one-dimensional spectrum from the two-dimensional spectral data, and the `spec1d` routine determines the redshift of this spectrum by cross-correlating with a series of templates. This cross-correlation also serves to distinguish galaxies and failed observations that returned no flux.

We refer to these 10619 spectra as our “science spectra," and they have a median S/N of 3.4 pix^{-1}.

2.2.3 Spectroscopic Templates

To complement the Milky Way spectroscopic templates included in the `spec2d` pipeline, we observed a series of Milky Way carbon stars to use as radial velocity and spectral type templates. The stars were selected from the SIMBAD database (Wenger *et al.*, 2000) based on magnitude, position, and spectral type. Their apparent magnitudes are in the range

$7.74 > V > 6.21$ and their spectral types span C5 to C8 based on the Keenan and Morgan classification scheme (Keenan and Morgan, 1941).

The observations were carried out using the 600 line mm^{-1} DEIMOS grating centered at 7000Å and the GG455 filter to block shorter wavelength light. We use the long-slit mask LVMslits with a 0.8" wide slit. This instrumental configuration provides a wavelength coverage of 4800-9500Å with a spectral resolution of 0.65Å pixel^{-1}. The raw two-dimensional spectra were reduced and extracted in the same manner as the science spectra.

Our final suite of spectroscopic templates contains 31 stars with a median S/N of 43 pix^{-1}, significantly higher than our 10619 M31 spectra. The distribution of template spectral types is shown in Figure 2.1. When referring to these spectra, we will use the term“template spectra" to distinguish them from the “science spectra."

2.2.4 AGB Identification

We use position on the PHAT color-magnitude diagrams (CMDs) identify stars at different evolutionary stages. The regions discussed in this section are illustrated in Figure 2.2.

Stars on the red giant branch (RGB) were identified using optical ($F475W$ and $F814W$) Padova PARSEC1.2s isochrones (Bressan *et al.*, 2012). The RGB boundaries, and most importantly the tip of the red giant branch (TRGB), were defined using isochrones with $-2.1 <$ [M/H] < 0.6 and a fiducial age of 10 Gyr. We assumed a foreground reddening of A_V = 0.17 mag and a distance to M31 of 776 ± 18 kpc (Dalcanton *et al.*, 2012). For an example of the RGB footprint, see Figure 1 of G15. Super giants (SG) were identified as a distinct branch in $F336W - F475W$ vs. $F110W - F160W$ color-color space. All objects not classi-

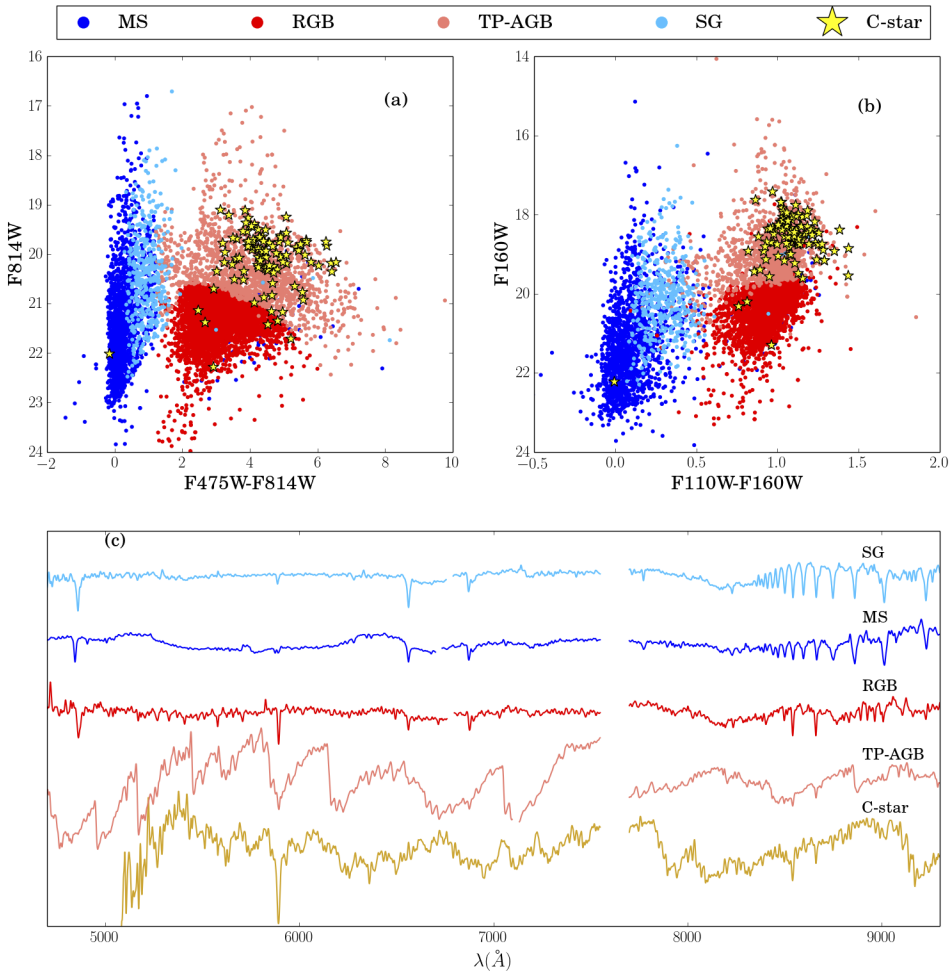

Figure 2.2: Panel (a) shows an optical ($F814W$ vs. $F475W-F814W$) CMD of stars in the SPLASH sample, color-coded by evolutionary stage as determined from the photometry. Main sequence stars are plotted in blue, super giants in cyan, RGB stars in red, and AGB stars in pink. We show those stars identified as spectroscopically as carbon stars as yellow stars. Panel (b) shows the same stars on a NIR ($F160W$ vs. $F110W-F160$) CMD. Panel (c) shows a representative DEIMOS spectrum of each of the color-coded populations in the top panels. Spectra are normalized, smoothed by a Gaussian with $\sigma \sim 3$ pixels, and plotted with a vertical offset. We also mask the telluric A band at 7600Å.

fied as SG or RGB were classified based on optical color and magnitude. Those stars with $F475W - F814W < 1.2$ are assumed to be main sequence (MS) stars, and those stars brighter than the TRGB with $F475W - F814W > 1.2$ are assumed to be AGB stars. These designations are purely photometric, with no reliance on spectral features. Our spectroscopic sample is dominated by RGB stars (5680), with 2489 MS stars and 1867 AGB stars. The remaining 583 objects are classified as either SG or PNe.

These designations are such that the bluest AGB stars may be bright supergiants and/or core helium-burning stars. We cannot distinguish between these objects and early-type AGB stars photometrically or spectroscopically at our resolution (Melbourne *et al.*, 2012; Dalcanton *et al.*, 2012). Alternatively, some may be the reddest (and relatively few) Milky Way stars that are observed at very red colors (Williams *et al.*, 2014). In addition, the distinction between RGB and AGB stars means our AGB sample is dominated by TP-AGB stars.

2.2.5 Carbon Star Identification

Our primary method of identifying carbon stars compares each science spectrum to our suite of 31 Milky Way template stars. To compute whether a science spectrum is best fit by a carbon template or a non-carbon template, we use a simple classification statistic K defined as:

$$K = \min\left(\chi^2(\theta_{NC})\right) - \min\left(\chi^2(\theta_C)\right) \tag{2.1}$$

where θ_{NC} denotes the suite of non-carbon template stars, and θ_C is the suite of carbon template

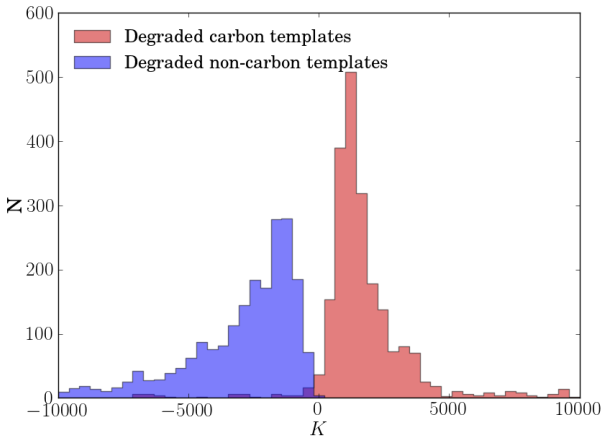

Figure 2.3: Evaluation of the K-statistic based carbon star identification method. The solid histograms show the distribution of K values for our degraded templates with S/N>2. For ease of visualization, we truncate the x-axis, and note that templates degraded to a relatively high S/N often have K values beyond these bounds.

stars. K is the difference between the χ^2 statistic for the best fitting non-carbon template and the χ^2 statistic for the best fitting carbon template. By this definition, those stars with $K > 0$ are likely carbon stars. This metric is loosely based on the ratio of evidence, or Bayes Factor, with a minimization rather than a sum.

We verify this method by degrading the S/N of each template to mimic the range of S/N present in our data, and then computing the degraded template's K value by comparing it to the remaining 30 templates. This process is repeated until there are ~ 3000 degraded carbon templates and ~ 3000 degraded non-carbon templates. Figure 2.3 shows the distribution of K for our degradation tests. They indicate that this method is $\sim 88\%$ accurate across the full range of S/N, and $\sim 95\%$ accurate for those stars with S/N ≥ 2 pix^{-1}.

We apply our classification statistic to the 7903 stellar spectra with S/N pix$^{-1} > 2$,

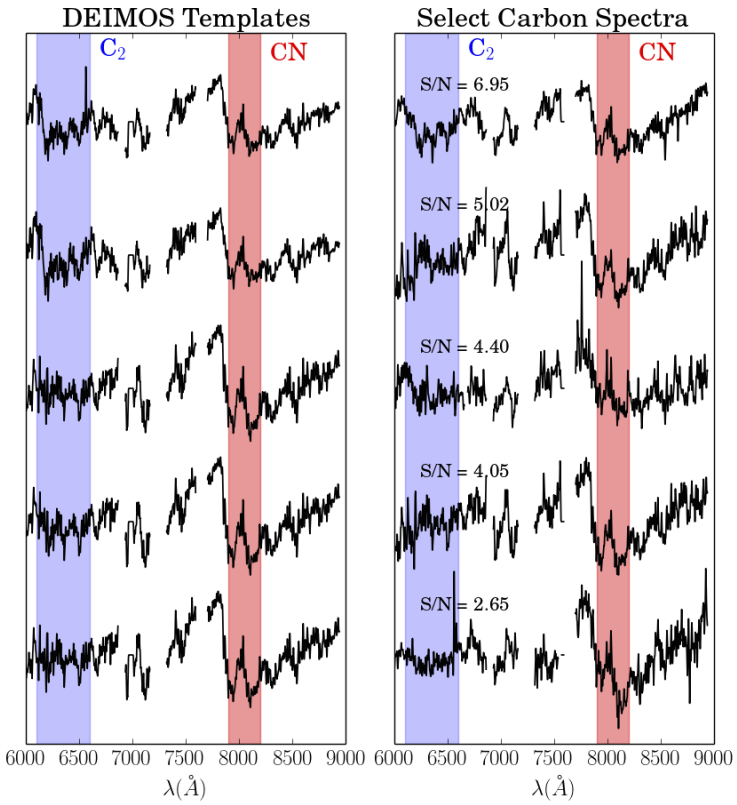

Figure 2.4: The left panel shows the five MW carbon stars used as templates for identification via K-statistic. The right panel shows five M31 carbon stars chosen to demonstrate a range of S/N. Spectra are smoothed by a Gaussian with $\sigma \sim 3$ pixels, and the telluric A band at 7600Å is masked. The science spectra are labeled with their S/N pix^{-1}. On both panels we have labeled the region where C_2 is prominent in blue ($\sim 6100-6600$ Å), and the region where CN is prominent in red $\sim 7900-8200$Å). These are the features we look for during the visual inspection that follows any automated carbon star detection method.

and visually inspect the spectra that return $K > 0$. Specifically, we look for the CN features at $\sim$ 7900Å and C_2 features between 6100 and 6600Å, shown in Figure 2.4 for the five carbon templates and five randomly chosen carbon science spectra. We find a total of 94 carbon stars. There are 316 objects whose spectra return $K > 0$ but upon inspection do not have the carbon features highlighted in Figure 2.4. This is a higher false-positive rate than our tests predicted,

because our tests did not simulate the bad sky subtraction or untrustworthy radial velocity measurements common for a multi-slit spectrograph.

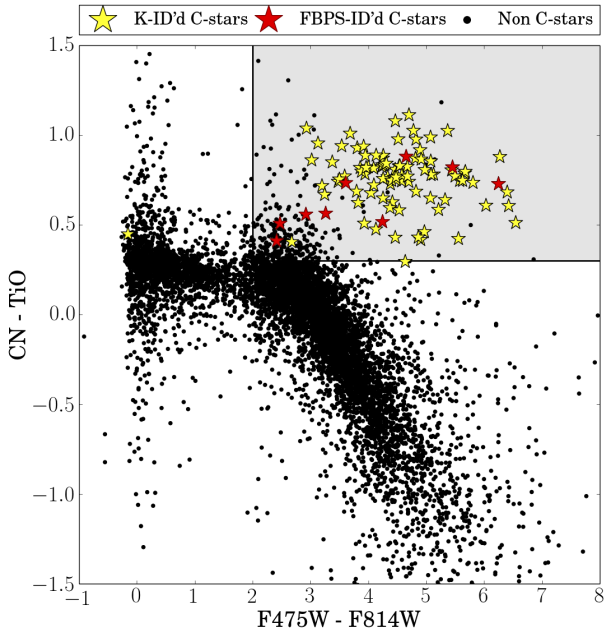

Figure 2.5: FBPS Color-color diagram ($F475W-F814W$ vs. synthetic CN–TiO) used to identify potential carbon stars. The grey shaded region is defined by the bounds $F475W-F814W >$ 2.0 and CN–TiO$>$ 0.3, and represents where carbon stars are likely to lie. Carbon stars identified by the K classification statistic are plotted as yellow stars, and carbon stars identified using this FBPS photometry (plus visual inspection of the spectra) are plotted as red stars. All other stars are plotted as black points.

To catch carbon stars that may have escaped identification by the K-statistic, we run a separate identification using synthetic narrow-band photometry modeled on the four band photometry system (FBPS). FBPS has been used extensively throughout the Local Group (e.g., Nowotny *et al.*, 2003; Battinelli and Demers, 2004a,b; Wing, 2007; Battinelli and Demers, 2009). FBPS uses broad band color (i.e. $R-I$, $V-I$) in conjunction with the color defined by the narrow band CN and TiO filters (centered at 8120.5Å and 7778.4Å, respectively) to

separate C- and O-rich AGB stars. It is one of two preferred photometric techniques for this separation (the other being NIR J and K_s photometry, whose reliability has recently been called into question; Menzies *et al.*, 2015).

To compute synthetic CN and TiO magnitudes from our spectra, we perform a first-order flux calibration. We create a transmission curve by dividing our MW template spectrum of HD52005 with the fully flux-calibrated spectrum of HD52005 from the X-shooter Spectral Library (Chen *et al.*, 2014), and use this transmission curve to correct the shape of our spectra. We then weight the spectra by the CFHT/CFH12k CN and TiO throughput curves to generate synthetic photometry.[1] We use $F475W - F814W$ as our broad band color.

Because this method is computationally inexpensive, we run it on all stellar spectra to catch any carbon stars whose S/N excluded them from the K-statistic method. The resulting FBPS diagram is shown in Figure 2.5. We define the region of likely carbon stars using the position of carbon stars identified by the K classification statistic. The bounds are $F475W - F814W > 2.0$ and CN–TiO > 0.3, which is fully consistent with the bounds used throughout the literature. We visually inspect the spectra of each star in the bounded region, and find an additional 9 carbon stars.

In total, we find 103 carbon stars in our sample of stars in the disk of M31. By using this combination of two automated-detection techniques plus visual inspection, we are confident that these 103 stars represent the vast majority of carbon stars in our spectroscopic sample. Their positions and magnitudes are listed in Table 2.1.

[1] http://svo2.cab.inta-csic.es/svo/theory/fps3/

Table 2.1: Positions and Magnitudes of Carbon Stars in the M31 Disk

Object name	RA	DEC	F275W	F336W	F475W	F814W	F110W	F160W
632832	00:44:34.87	+41:22:56.4	...	...	26.50 ± 0.068	20.93 ± 0.004	19.14 ± 0.003	17.90 ± 0.002
1114302	00:45:7.40	+41:35:45.5	...	28.97 ± 3.814	25.98 ± 0.046	20.65 ± 0.003	18.90 ± 0.002	17.61 ± 0.001
957290	00:45:16.32	+41:31:41.0	...	...	24.45 ± 0.017	20.22 ± 0.003	18.63 ± 0.002	17.56 ± 0.001
1218429	00:45:31.09	+41:38:22.1	...	...	25.11 ± 0.026	20.98 ± 0.004	19.61 ± 0.003	18.46 ± 0.002
1812722	00:45:25.51	+41:53:58.4	...	...	24.72 ± 0.020	20.26 ± 0.003	18.69 ± 0.002	17.59 ± 0.001
1838301	00:45:41.87	+41:54:40.7	...	27.60 ± 0.902	26.18 ± 0.048	21.35 ± 0.005	19.16 ± 0.002	17.87 ± 0.001
1917632	00:46:1.98	+41:56:56.9	27.29 ± 1.949	28.34 ± 1.783	26.78 ± 0.087	20.35 ± 0.003	18.71 ± 0.002	17.48 ± 0.001
1979836	00:46:31.73	+41:58:44.8	...	...	26.14 ± 0.055	21.17 ± 0.005	19.48 ± 0.002	18.36 ± 0.002
2099025	00:46:6.86	+42:02:18.6	...	26.99 ± 0.540	24.52 ± 0.018	20.27 ± 0.003	19.05 ± 0.002	18.05 ± 0.002
1144396	00:44:58.75	+41:36:32.0	26.31 ± 0.895	...	26.33 ± 0.067	20.77 ± 0.004	18.76 ± 0.002	17.50 ± 0.001
1494	00:44:38.22	+41:34:11.8	28.45 ± 4.180	...	25.29 ± 0.030	20.88 ± 0.004	19.17 ± 0.002	18.13 ± 0.002
1838301	00:45:41.87	+41:54:40.7	...	27.60 ± 0.902	26.18 ± 0.048	21.35 ± 0.005	19.16 ± 0.002	17.87 ± 0.001

Table 2.1 (cont'd): Positions and Magnitudes of Carbon Stars in the M31 Disk

Object name	RA	DEC	F275W	F336W	F475W	F814W	F110W	F160W
1834050	00:44:42.40	+41:54:37.9	...	26.66 ± 0.402	25.80 ± 0.039	21.16 ± 0.004	19.55 ± 0.002	18.11 ± 0.002
serendip1	00:00:00	00:00:00	...	...	24.33 ± 0.014	20.27 ± 0.003	18.91 ± 0.002	17.86 ± 0.001
2470661	00:46:50.73	+42:16:7.3	28.70 ± 6.427	28.04 ± 1.429	24.94 ± 0.022	20.25 ± 0.003	18.76 ± 0.002	17.63 ± 0.001
b9rgb3481	00:44:35.91	+41:34:21.7	28.60 ± 4.537	26.09 ± 0.242	23.64 ± 0.011	20.70 ± 0.004	19.44 ± 0.002	18.58 ± 0.002
b9rgb11510	00:44:40.33	+41:28:41.4	...	26.48 ± 0.396	24.06 ± 0.014	21.38 ± 0.005	20.32 ± 0.004	19.56 ± 0.004
serendip1	00:00:00	00:00:00	...	...	26.18 ± 0.049	20.62 ± 0.003	19.14 ± 0.002	17.80 ± 0.001
b21rgb7503	00:46:19.03	+42:12:58.7	...	...	26.93 ± 0.098	21.72 ± 0.006	18.93 ± 0.002	17.58 ± 0.001
14702	00:43:18.68	+41:05:31.8	...	...	...	...	...	...
AGB101937	00:44:32.06	+41:14:54.3	...	...	24.76 ± 0.030	20.29 ± 0.003	18.83 ± 0.002	17.75 ± 0.001
AGB104081	00:44:33.09	+41:15:1.2	27.97 ± 3.127	...	24.95 ± 0.024	20.06 ± 0.003	18.55 ± 0.002	17.51 ± 0.001
AGB113694	00:44:35.25	+41:15:32.9	26.51 ± 0.767	27.32 ± 0.727	23.23 ± 0.009	19.97 ± 0.003	18.71 ± 0.002	17.73 ± 0.001
AGB130086	00:44:29.58	+41:16:31.4	27.34 ± 1.756	...	24.05 ± 0.014	20.51 ± 0.003	19.39 ± 0.002	18.50 ± 0.002

Table 2.1 (cont'd): Positions and Magnitudes of Carbon Stars in the M31 Disk

Object name	RA	DEC	F275W	F336W	F475W	F814W	F110W	F160W
AGB130345	00:44:26.77	+41:16:32.4	...	26.94 ± 0.493	23.97 ± 0.013	19.91 ± 0.002	18.38 ± 0.001	17.40 ± 0.001
AGB200857	00:44:43.95	+41:20:31.3	28.33 ± 3.877	...	24.32 ± 0.016	19.25 ± 0.002	17.42 ± 0.001	16.45 ± 0.001
AGB123999	00:44:39.97	+41:16:8.9	...	28.91 ± 3.159	24.31 ± 0.016	20.06 ± 0.003	18.76 ± 0.002	17.76 ± 0.001
AGB183868	00:44:36.11	+41:19:35.2	28.42 ± 4.466	...	24.53 ± 0.018	19.63 ± 0.002	17.99 ± 0.001	16.86 ± 0.001
AGB207577	00:44:49.56	+41:20:54.0	...	...	22.59 ± 0.006	19.21 ± 0.002	18.39 ± 0.002	17.00 ± 0.001
AGB228315	00:44:54.10	+41:22:1.3	27.31 ± 1.531	29.20 ± 3.450	24.84 ± 0.023	20.32 ± 0.003	18.70 ± 0.002	17.74 ± 0.001
AGB264645	00:44:54.23	+41:23:27.9	26.66 ± 0.886	29.57 ± 5.029	24.37 ± 0.017	20.04 ± 0.003	18.72 ± 0.002	17.59 ± 0.001
AGB275033	00:44:54.60	+41:23:48.0	26.79 ± 1.073	...	25.24 ± 0.033	19.87 ± 0.002	18.75 ± 0.002	17.47 ± 0.001
AGB435917	00:44:42.01	+41:27:41.8	...	...	23.97 ± 0.013	19.51 ± 0.002	18.06 ± 0.001	16.90 ± 0.001
AGB525239	00:44:35.23	+41:31:19.6	25.30 ± 0.323	26.65 ± 0.461	22.98 ± 0.008	19.78 ± 0.002	18.56 ± 0.002	17.68 ± 0.001
AGB60410	00:44:32.06	+41:12:25.8	25.43 ± 0.397	26.60 ± 0.375	25.37 ± 0.031	19.91 ± 0.002	18.29 ± 0.001	17.15 ± 0.001
AGB136920	00:44:24.53	+41:16:56.7	...	...	23.75 ± 0.011	19.50 ± 0.002	18.05 ± 0.001	16.93 ± 0.001

Table 2.1 (cont'd): Positions and Magnitudes of Carbon Stars in the M31 Disk

Object name	RA	DEC	F275W	F336W	F475W	F814W	F110W	F160W
AGB362536	00:43:58.57	+41:26:0.6	26.83 ± 1.143	...	26.10 ± 0.058	19.83 ± 0.002	17.68 ± 0.001	16.66 ± 0.001
AGB646685	00:45:48.08	+41:39:7.2	25.48 ± 0.354	...	24.33 ± 0.016	20.52 ± 0.003	19.14 ± 0.002	18.21 ± 0.002
AGB700036	00:46:3.72	+41:42:7.5	...	...	23.83 ± 0.013	19.83 ± 0.002	18.36 ± 0.002	17.42 ± 0.001
AGB721183	00:45:51.24	+41:44:0.9	...	...	25.49 ± 0.033	20.83 ± 0.004	19.23 ± 0.002	18.13 ± 0.002
AGB786679	00:46:1.83	+41:50:2.9	26.27 ± 0.651	...	24.90 ± 0.022	19.77 ± 0.002	18.02 ± 0.001	16.84 ± 0.001
AGB733399	00:45:57.92	+41:45:15.3	...	26.55 ± 0.339	23.37 ± 0.009	20.35 ± 0.003	18.92 ± 0.002	18.10 ± 0.002
AGB737588	00:45:29.77	+41:45:40.4	26.46 ± 0.899	...	23.46 ± 0.009	19.54 ± 0.002	18.06 ± 0.001	17.03 ± 0.001
AGB761210	00:45:35.86	+41:47:54.2	...	29.41 ± 5.800	23.84 ± 0.011	19.75 ± 0.002	18.19 ± 0.001	17.17 ± 0.001
AGB768789	00:45:28.15	+41:48:38.1	26.58 ± 0.963	...	24.17 ± 0.014	20.35 ± 0.003	19.01 ± 0.002	17.94 ± 0.002
AGB807017	00:45:25.31	+41:51:10.3	...	27.02 ± 0.509	25.13 ± 0.026	20.32 ± 0.003	18.56 ± 0.001	17.42 ± 0.001
AGB325404	00:44:22.14	+41:25:9.8	...	...	24.03 ± 0.013	19.65 ± 0.002	18.03 ± 0.001	16.94 ± 0.001
AGB344610	00:44:15.78	+41:25:36.7	28.56 ± 5.650	...	24.62 ± 0.020	19.76 ± 0.002	18.18 ± 0.001	16.95 ± 0.001

Table 2.1 (cont'd): Positions and Magnitudes of Carbon Stars in the M31 Disk

Object name	RA	DEC	F275W	F336W	F475W	F814W	F110W	F160W
AGB608579	00:44:12.91	+41:37:42.9	...	26.59 ± 0.439	23.22 ± 0.008	19.27 ± 0.002	17.83 ± 0.001	16.80 ± 0.001
AGB635297	00:45:1.47	+41:38:40.8	...	...	24.76 ± 0.020	19.98 ± 0.002	18.13 ± 0.001	17.05 ± 0.001
AGB916458	00:46:16.80	+41:57:6.4	...	26.64 ± 0.418	24.58 ± 0.017	19.66 ± 0.002	18.49 ± 0.001	17.32 ± 0.001
AGB927616	00:46:16.20	+41:57:51.0	...	28.96 ± 2.985	24.86 ± 0.021	20.33 ± 0.003	19.00 ± 0.002	17.92 ± 0.001
AGB941170	00:46:12.80	+41:58:49.7	...	...	25.38 ± 0.030	19.72 ± 0.002	18.40 ± 0.001	17.17 ± 0.001
AGB950342	00:46:16.70	+41:59:31.9	29.46 ± 9.999	...	24.12 ± 0.013	19.87 ± 0.002	18.52 ± 0.001	17.39 ± 0.001
AGB958857	00:45:59.97	+42:00:15.5	...	28.74 ± 2.434	25.09 ± 0.029	20.02 ± 0.002	18.59 ± 0.002	17.51 ± 0.001
AGB984469	00:45:55.26	+42:03:32.5	27.13 ± 1.433	28.31 ± 1.750	23.41 ± 0.009	20.17 ± 0.003	18.93 ± 0.002	18.01 ± 0.001
AGB991275	00:46:2.31	+42:04:52.1	...	...	25.37 ± 0.031	19.93 ± 0.002	18.40 ± 0.001	17.28 ± 0.001
AGB1001917	00:45:55.16	+42:06:42.4	...	28.36 ± 2.114	25.44 ± 0.035	19.76 ± 0.002	18.02 ± 0.001	16.96 ± 0.001
AGB308200	00:44:42.77	+41:24:43.5	...	26.14 ± 0.282	23.94 ± 0.012	19.69 ± 0.002	17.90 ± 0.001	16.71 ± 0.001
MS782319	00:45:29.84	+41:49:46.5	...	...	25.08 ± 0.034	20.38 ± 0.003	18.64 ± 0.002	17.49 ± 0.001

Table 2.1 (cont'd): Positions and Magnitudes of Carbon Stars in the M31 Disk

Object name	RA	DEC	F275W	F336W	F475W	F814W	F110W	F160W
AGB811994	00:45:21.69	+41:51:25.2	27.09 ± 1.339	27.49 ± 0.786	23.69 ± 0.011	19.76 ± 0.002	18.21 ± 0.001	17.15 ± 0.001
AGB868679	00:44:59.51	+41:54:12.7	27.37 ± 1.779	...	23.30 ± 0.009	19.69 ± 0.002	18.33 ± 0.001	17.36 ± 0.001
x12_18	00:44:50.30	+41:52:42.0	...	29.13 ± 3.725	24.65 ± 0.018	19.57 ± 0.002	18.30 ± 0.001	17.15 ± 0.001
AGB877820	00:45:55.77	+41:54:43.8	27.04 ± 2.678	...	26.58 ± 0.072	20.18 ± 0.003	18.47 ± 0.001	17.21 ± 0.001
AGB897095	00:45:55.49	+41:55:55.2	...	...	26.00 ± 0.051	19.75 ± 0.002	18.30 ± 0.001	17.12 ± 0.001
AGB928293	00:46:16.55	+41:57:54.0	...	...	25.30 ± 0.028	19.80 ± 0.002	17.76 ± 0.001	16.65 ± 0.001
AGB954883	00:46:14.35	+41:59:54.4	...	...	24.16 ± 0.014	19.90 ± 0.002	18.22 ± 0.001	17.20 ± 0.001
AGB1019165	00:47:34.41	+42:08:52.5	26.05 ± 0.527	...	23.33 ± 0.009	19.54 ± 0.002	18.13 ± 0.001	17.09 ± 0.001
AGB1033441	00:47:8.22	+42:10:52.7	...	...	25.27 ± 0.026	20.19 ± 0.003	18.67 ± 0.002	17.54 ± 0.001
AGB1011804	00:47:36.12	+42:07:57.5	26.98 ± 1.101	...	23.53 ± 0.010	19.39 ± 0.002	17.92 ± 0.001	16.88 ± 0.001
AGB1013255	00:47:7.76	+42:08:8.2	...	...	26.27 ± 0.074	20.23 ± 0.003	18.75 ± 0.002	17.55 ± 0.001
AGB1018949	00:47:36.61	+42:08:50.8	...	...	24.38 ± 0.016	19.93 ± 0.003	18.34 ± 0.001	17.26 ± 0.001

Table 2.1 (cont'd): Positions and Magnitudes of Carbon Stars in the M31 Disk

Object name	RA	DEC	F275W	F336W	F475W	F814W	F110W	F160W
AGB885533	00:46:25.99	+41:55:11.5	26.92 ± 1.264	...	23.48 ± 0.010	19.44 ± 0.002	17.95 ± 0.001	16.89 ± 0.001
AGB912171	00:46:16.69	+41:56:50.3	...	...	25.26 ± 0.026	20.59 ± 0.003	18.75 ± 0.002	17.61 ± 0.001
AGB912271	00:46:17.30	+41:56:50.7	...	...	26.71 ± 0.098	20.17 ± 0.003	18.85 ± 0.002	17.42 ± 0.001
AGB919772	00:46:6.27	+41:57:19.9	...	...	23.95 ± 0.012	19.66 ± 0.002	18.15 ± 0.001	17.11 ± 0.001
AGB984897	00:45:38.64	+42:03:37.4	...	27.59 ± 0.946	24.31 ± 0.015	19.77 ± 0.002	18.36 ± 0.001	17.30 ± 0.001
AGB989533	00:45:24.03	+42:04:31.2	...	27.48 ± 0.850	24.31 ± 0.015	19.94 ± 0.002	18.47 ± 0.002	17.28 ± 0.001
AGB991661	00:45:41.16	+42:04:57.0	27.62 ± 2.680	...	24.81 ± 0.020	20.23 ± 0.003	18.59 ± 0.002	17.50 ± 0.001
AGB1003784	00:45:30.23	+42:06:57.6	...	27.97 ± 1.250	23.78 ± 0.011	19.84 ± 0.002	18.29 ± 0.001	17.23 ± 0.001
AGB1041472	00:45:42.92	+42:11:58.3	26.48 ± 0.837	26.84 ± 0.474	23.69 ± 0.010	20.21 ± 0.003	18.69 ± 0.002	17.75 ± 0.001
MS1046642	00:46:9.10	+42:12:49.4	20.16 ± 0.014	20.46 ± 0.009	21.86 ± 0.004	22.02 ± 0.007	22.23 ± 0.010	22.23 ± 0.018
AGB1051246	00:46:7.87	+42:13:42.0	...	...	23.68 ± 0.011	20.09 ± 0.002	18.49 ± 0.001	17.51 ± 0.001
AGB1052705	00:45:55.27	+42:13:59.7	27.26 ± 1.699	...	24.55 ± 0.016	20.07 ± 0.002	18.73 ± 0.002	17.67 ± 0.001

Table 2.1 (cont'd): Positions and Magnitudes of Carbon Stars in the M31 Disk

Object name	RA	DEC	F275W	F336W	F475W	F814W	F110W	F160W
AGB1060489	00:46:32.55	+42:15:55.5	...	28.06 ± 1.272	23.80 ± 0.012	19.71 ± 0.002	18.57 ± 0.002	17.50 ± 0.001
AGB1015684	00:46:15.03	+42:08:26.7	26.48 ± 0.966	28.31 ± 1.705	25.65 ± 0.033	20.02 ± 0.003	18.39 ± 0.001	17.18 ± 0.001
AGB1021614	00:46:12.77	+42:09:11.8	...	...	25.97 ± 0.046	20.17 ± 0.003	18.52 ± 0.001	17.30 ± 0.001
AGB1051056	00:46:58.21	+42:13:39.8	25.67 ± 0.409	...	24.35 ± 0.016	19.78 ± 0.002	18.44 ± 0.001	17.35 ± 0.001
AGB1016791	00:46:19.04	+42:08:34.8	...	28.77 ± 2.498	24.44 ± 0.016	20.13 ± 0.003	18.62 ± 0.001	17.50 ± 0.001
AGB1053711	00:47:17.40	+42:14:10.3	...	...	22.98 ± 0.008	19.12 ± 0.002	17.69 ± 0.001	16.67 ± 0.001
AGB1054258	00:47:7.53	+42:14:16.8	27.74 ± 2.297	...	25.14 ± 0.025	20.16 ± 0.003	18.54 ± 0.001	17.44 ± 0.001
AGB1060656	00:47:22.12	+42:15:58.7	...	...	23.76 ± 0.011	20.08 ± 0.003	18.81 ± 0.002	17.89 ± 0.001
RGB1068713	00:47:21.37	+42:18:44.2	...	...	25.96 ± 0.043	21.43 ± 0.005	19.57 ± 0.002	18.62 ± 0.002
AGB989067	00:46:19.85	+42:04:26.0	...	...	24.14 ± 0.014	19.74 ± 0.002	18.39 ± 0.002	17.36 ± 0.001
AGB998005	00:46:7.82	+42:06:6.4	28.49 ± 5.763	27.81 ± 1.643	23.25 ± 0.009	19.37 ± 0.002	18.26 ± 0.001	17.26 ± 0.001
AGB998781	00:46:7.57	+42:06:13.9	...	...	24.52 ± 0.017	19.84 ± 0.002	18.18 ± 0.001	17.12 ± 0.001

Table 2.1 (cont'd): Positions and Magnitudes of Carbon Stars in the M31 Disk

Object name	RA	DEC	F275W	F336W	F475W	F814W	F110W	F160W
AGB1000094	00:45:58.56	+42:06:26.1	26.59 ± 0.872	27.61 ± 0.919	24.42 ± 0.017	19.94 ± 0.003	18.45 ± 0.001	17.34 ± 0.001
RGB1001683	00:46:8.92	+42:06:40.5	28.02 ± 2.864	26.59 ± 0.375	23.61 ± 0.011	21.14 ± 0.005	20.20 ± 0.003	19.39 ± 0.003
AGB1002819	00:46:2.64	+42:06:49.4	...	27.50 ± 0.811	23.70 ± 0.011	19.74 ± 0.002	18.16 ± 0.001	17.10 ± 0.001
AGB1015589	00:46:5.81	+42:08:25.8	28.55 ± 5.189	25.64 ± 0.183	22.24 ± 0.005	19.10 ± 0.002	17.63 ± 0.001	16.76 ± 0.001
AGB1019465	00:46:9.98	+42:08:54.7	...	26.11 ± 0.262	23.17 ± 0.008	19.67 ± 0.002	18.35 ± 0.001	17.40 ± 0.001
PC819	00:45:57.96	+42:08:41.1	...	...	25.21 ± 0.025	22.28 ± 0.008	21.30 ± 0.006	20.34 ± 0.005
serendip2	00:00:00	00:00:00	...	27.91 ± 1.187	24.85 ± 0.020	19.99 ± 0.002	18.43 ± 0.001	17.27 ± 0.001

While the majority of these carbon stars lie predictably above the TRGB, four are found in other areas of the CMD (see Figure 2.2). Three have colors and magnitudes matching the RGB population, and one lies in the MS. To verify that these stars are members of the M31 disk rather than foreground MW carbon dwarfs, we compute their line-of-sight (LOS) velocities. We convert each star's redshift measurement to a velocity, then apply a telluric A-band correction and a correction for heliocentric motion on the date the spectrum was obtained (for further details see Dorman *et al.*, 2012, and references therein). These four carbon stars have LOS velocities between −85 km/s and −300 km/s, making them likely M31 members. Their unusual colors and magnitudes are likely due to a mismatch between the SPLASH and PHAT catalogs.

2.3 Defining M

Our spectroscopic identification gives us an uncontaminated sample of unambiguous carbon stars. There exists no equivalent spectroscopic selection that can separate M-type TP-AGB stars from the RGB. And while the C/M ratio has been computed across the Local Group, there is no standard photometric definition for M-stars. Even within M31, multiple criteria have been devised to isolate M-stars based on available data. We examine three criteria based on the work by Boyer *et al.* (2013, hereafter B13), Brewer *et al.* (1995, hereafter B95), and Battinelli and Demers (2005, hereafter BD05). Our goal is not to define a single, "correct" method, but rather to investigate the differences in results returned by each of these methods.

2.3.1 Boyer et al. 2013

The first definition of M that we apply to our data is one modified from B13. As they use WFC3/IR medium-band filters to discriminate between C- and M-type TP-AGB stars, our dataset is certainly not identical. IR filters are far more sensitive to dust-enshrouded stars than optical filters, and so the B13 sample will be substantially more complete. However, they make two major assumptions that we can emulate: TP-AGB stars are brighter than TRGB, and all AGB stars not classified as C-stars are M-stars. Their definition of the TRGB also comes from PHAT photometry, so this identification of AGB stars matches our own. If we too take all non-carbon AGB stars to be M-type, we get a sample of 1605 stars from our original sample of 10619 spectra.

Whenever this particular sample is used, it will be denoted by a red diamond and will be referred to as the B13 method.

2.3.2 Brewer et al. 1995

B95 is one of the few large-scale AGB surveys of M31. The authors used FBPS in five regions located along the southern major axis. They define M by the following criteria: $V-I > 1.8$, CN–TiO < -0.2, $I > 18.5$, and $M_{bol} < -3.5$ (where $M_{bol} = I + 0.3 + 0.34(V-I) - 0.14(V-I)^2 - (m-M)_0$). They assume a distance modulus of 24.41, adopted from Freedman and Madore (1990).

To replicate these criteria for our sample, we convert our $F475W$ and $F814W$ magnitudes to V and I. To convert from $F814W$ to I we use the 97 M-giant spectral templates presented by Fluks *et al.* (1994). We convolve the Fluks et al. spectra with the HST/ACS

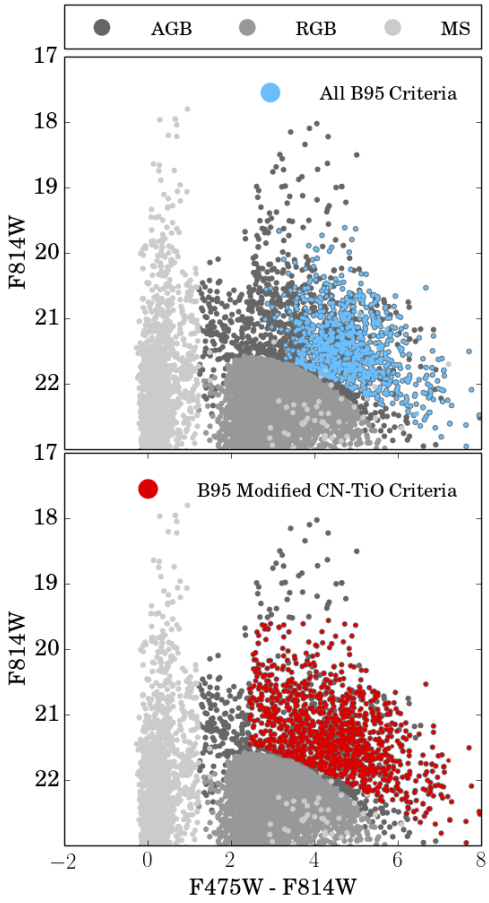

Figure 2.6: The results of applying the FBPS-based M-giant selection criteria of Brewer et. al 1995 to our spectroscopic sample. The top panel includes all selection criteria; $V-I > 1.8$, CN–TiO < -0.2, $I > 18.5$, and $M_{\rm bol} < -3.5$. $M_{\rm bol} = I + 0.3 + 0.34(V-I) - 0.14(V-I)^2 - (m-M)_0$. The bottom panel includes all broad-band color and magnitude cuts but replaces the CN–TiO with the criterium that a star not be a spectroscopically-identified carbon star. AGB, RGB, and MS stars (denoted in grays) come from PHAT CMD-based identification. We adopt the cuts in the top panel for the B95 selection used in the rest of this paper.

$F814W$ bandpass and the CFHT/CFH12k I bandpass. The offset between $F814W$ and I is a function of color/spectral type. We fit a fourth-order polynomial to this relationship to determine a conversion function, getting residuals less than 0.002 magnitudes. To derive $V-I$ we

use the published transformations from Sirianni *et al.* (2005).

The application of B95 selection criteria is shown in Figure 2.6. When we apply all selection criteria from B95, our final sample contains 843 M-stars (shown in blue in the top panel of Fig 2.6). The sample is relatively uncontaminated, with only 2 stars having been identified by PHAT as RGB stars rather than AGB stars. However, it misses the bluest AGB stars ($F475W - F814W < 3$), the brightest AGB stars, and those stars close to the TRGB. The latter effect grows more pronounced at redder colors, and thus the more metal-rich populations. If we were to remove the CN−TiO criterium and replace it with the requirement that no star be a spectroscopically identified carbon star (see § 2.2.5), the sample would increase to 1218 (shown in red in the bottom panel of Fig 2.6), decreasing the resulting C/M ratio. This expands the sample to include many of the bluer AGB stars left out of the B95 sample.

In the remainder of the paper, we will use the unmodified B95 selection of 843 stars. Whenever this sample is used it will be denoted by a blue square and will be referred to as the B95 method.

2.3.3 Battinelli & Demers 2005

A common way to express the C/M ratio in the Local Group is C/M0+; i.e. the M-type AGB stars counted are those with a spectral type of M0 or later. This spectral-type selection is often defined photometrically using a color cut (e.g. $R - I > 0.9$). We can apply a color cut and determine spectral types from the spectra themselves. However, we must first note that the PHAT photometric observations and SPLASH spectroscopic observations were taken several months (or in some cases years) apart. Since a significant fraction of TP-AGB stars are long-

period variables of sizable amplitude, the measured PHAT colors may not reflect the colors of the star at the time the spectrum was taken.

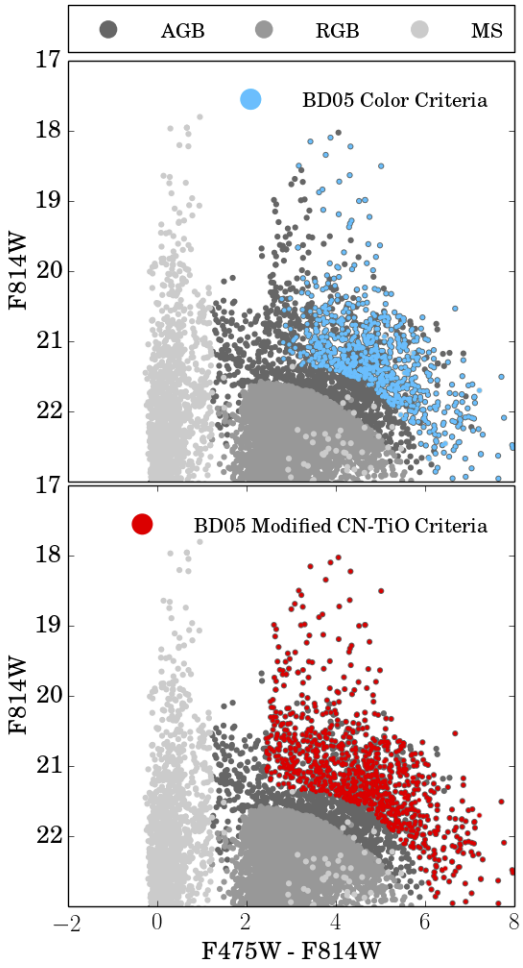

Figure 2.7: The results of applying the FBPS-based M-giant selection criteria of Battinelli & Demers 2005 to our spectroscopic sample. The top panel includes all BD05 selection criteria; $R-I > 0.9$, CN–TiO < 0, and $M_{\rm bol} < -3.5$. Here, $M_{\rm bol} = I + 1.7103 - 2.2968(R-I) + 1.66464(R-I)^2 - 0.43399(R-I)^3 - (m-M)_0$. The bottom panel replaces the CN–TiO criteria with the requirement that a star not be a spectroscopically identified carbon star. AGB, RGB, and MS stars (denoted in grays) come from PHAT CMD-based identification. We adopt the cuts in the top panel for the B05 selection used in the rest of this paper.

BD05 define M0+ to be those stars with $R-I > 0.9$ and CN–TiO < 0. This broad-band color criterium matches that used by B95, as $R-I = 0.9$ corresponds to $V-I = 1.8$. To distinguish M-type AGB stars, they use a bolometric magnitude limit of $M_{\rm bol} < -3.5$, where they adopt a slightly different definition of $M_{\rm bol}$ than B95: $M_{\rm bol} = I + 1.7103 - 2.2968(R-I) + 1.66464(R-I)^2 - 0.43399(R-I)^3 - (m-M)_0$. BD05 adopt a distance modulus $(m-M)_0 = 24.41$. To apply these same criteria we first transform $F475W$ and $F814W$ magnitudes into I (using the method outlined in the previous section), and then derive R using the transformations by (Sirianni *et al.*, 2005). The resulting sample is shown in blue in the top panel of Figure 2.7. It contains only 736 stars, as the sample stops half a magnitude above the TRGB. This sample also omits the bluest AGB stars, but unlike B95, it does contain the brightest. As with the B95 criteria, if we were to replace the CN–TiO limit with the requirement that no star be a spectroscopically identified carbon star the sample would increase to 960 stars (shown in red in the bottom panel of Fig 2.7), decreasing the resulting C/M ratio. As before, this would extend the sample in the blue but would have no effect on the proximity of the sample to the TRGB.

Since we have spectra in addition to photometry, we can also spectroscopically determine which stars have a subtype of M0 or later. We use the TiO-based spectral parameters, $S_{1/2,S_p}, S_{1/3,S_p}$, and $S_{2/3,S_p}$ defined in Fluks *et al.* (1994). These three parameters are calculated by integrating over the various TiO absorption features, and are monotonic functions of spectral type. Stars with subtype M0 or later have $S_{1/2,S_p} < 0.517, S_{1/3,S_p} < 0.754$, and $S_{2/3,S_p} < 1.458$. There is no spectroscopic distinction between AGB and RGB stars at this resolution, so we again apply the bolometric magnitude limit from BD05. This returns a sample of 773 M-stars, shown in yellow on Figure 2.8. The 736 M-stars identified by the photometric M0+ criteria are

plotted in red.

The sample of M-stars identified as M0+ by spectroscopic criteria are almost identical to those identified by the photometric criteria. The top and right panels of Figure 2.8 shows the marginal distributions of both the spectroscopic and photometric sample in color and magnitude. The color criteria are slightly less sensitive to fainter and bluer stars ($F814W > 18$).

In the remainder of the paper, we will use the unmodified BD05 photometric selection of 736 stars. Whenever this sample is used it will be denoted by a green circle and will be referred to as the BD05 method.

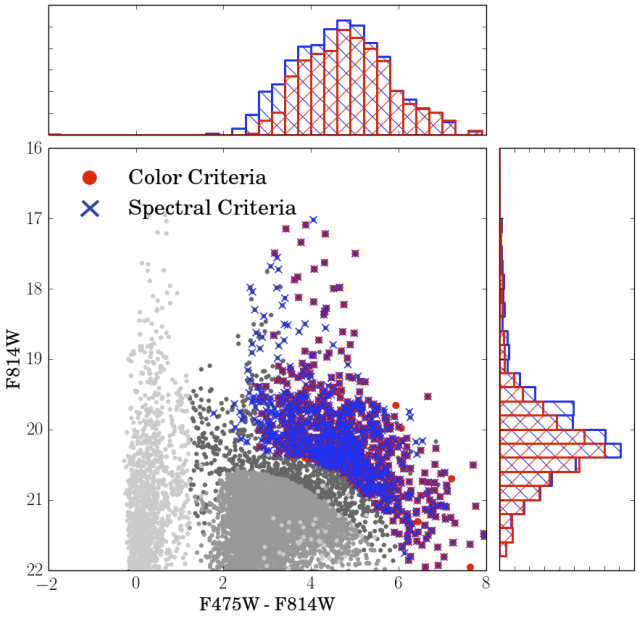

Figure 2.8: The result of a spectrum-based M-giant selection criterion applied to our sample. As in Figures 2.7 and 2.6, AGB, RGB, and MS stars are in greys. Yellow crosses represent those stars with spectral types of M0 or later, as determined by the indices from Fluks *et al.* (1994)

2.4 C/M ratio across M31

The broad range of environments in M31 mean that we can compute the C/M ratio as a function of a variety of properties. In this section we look at the C/M ratio as a function of galactocentric radius (R_g, § 2.4.1), metallicity (§ 2.4.2), and SFH (§ 2.4.3) in spatial bins.

We create the spatial bins used throughout this section beginning with equal-area bins on a flat circle with a radius of 20 kpc (roughly the outer limit of our data). We then incline the bins to match M31's inclination of 74° (Barmby *et al.*, 2006) and tilt the bins to match M31's position angle of 50° (determined empirically). The final positions of these bins are shown along with the positions of our C- and M-stars in Figure 2.9.

2.4.1 As a function of galactocentric radius

Using the bins shown in Figure 2.9, we determine the change in the C/M ratio as a function of radius. We compute the center radius of each bin by taking the average R_g of all PHAT stars within that bin. When computing this average, we leave out PHAT "Brick 1." Brick 1 covers the extremely crowded bulge region, extending only $\sim$ 2.7 kpc from the center of M31, where we have no spectroscopic coverage. Leaving those stars out of our average ensures that the resulting distances represent the regions in which our AGB stars lie. The resulting C/M ratios for each of the selection criteria discussed in §2.3 are shown in Figure 2.10.

There is a clear positive trend. A weighted least squares fit to the eight bins along

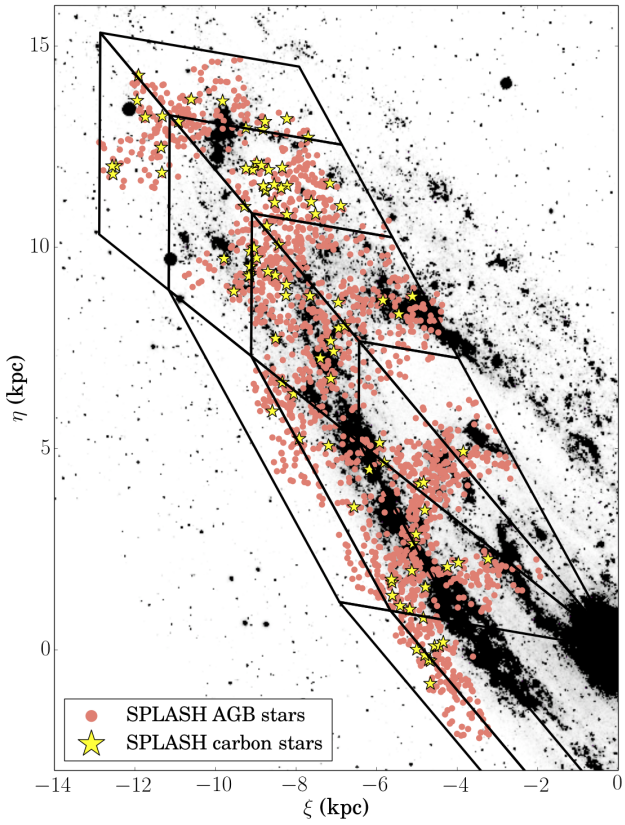

Figure 2.9: Positions of all AGB stars in the SPLASH sample (pink points), with carbon stars (yellow stars), overlaid on a GALEX image of M31. The spatial bins used throughout §2.4.1, §2.4.2 and §2.4.3 are marked with black lines. Apparent structure in the positions of the AGB stars is due to the SPLASH selection function, and is not a true physical effect.

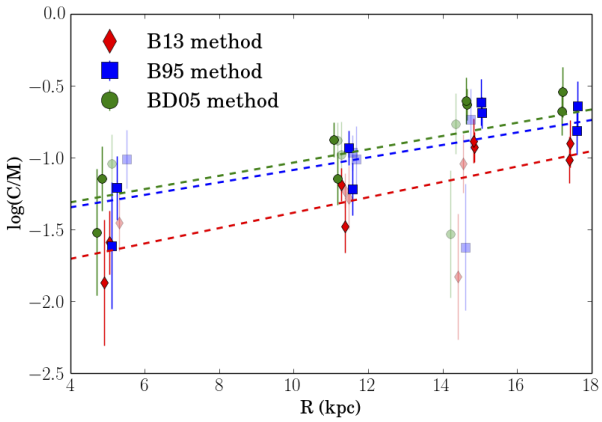

Figure 2.10: Log(C/M) ratio in bins of R_g. The radii are those of the mean stellar distance in each bin. Red diamonds represent points calculated using the B13-based definition of M, blue squares represent the B95-based definition of M, and green diamonds represent the BD05-based definition of M. For ease of visualization, B95 and BD05 points are artificially offset from the B13 points by 0.2 and -0.2 kpc, respectively. Bins along the major axis are shown as solid points and bins along the minor axis are shown as transparent points.

major axis bins determines the following gradients:

$$\log(\mathrm{C/M_{B13}}) = (0.06\pm0.016)\times R_g - (1.92\pm0.22) \tag{2.2}$$

$$\log(\mathrm{C/M_{B95}}) = (0.05\pm0.016)\times R_g - (1.56\pm0.23) \tag{2.3}$$

$$\log(\mathrm{C/M_{BD05}}) = (0.06\pm0.017)\times R_g - (1.53\pm0.23) \tag{2.4}$$

This trend is likely to be driven not by the radius itself, but by other quantities that vary with radius. We consider correlations with these quantities in the following two sections.

2.4.2 As a function of metallicity

We are in a unique position to compute the C/M ratio as a function of metallicity calculated using different techniques and for different tracer populations. In this section we focus on gas-phase metallicity, as determined from HII regions, and on photometrically derived stellar metallicity.

2.4.2.1 Gas-phase metallicity

We first look at the gas-phase metallicities from Sanders *et al.* (2012). The authors measure the oxygen abundance ([O/H]) in HII regions using strong-line diagnostics from Zaritsky *et al.* (1994), Kewley and Dopita (2002), Nagao *et al.* (2006), and Pilyugin and Thuan (2005). They find the first three methods very consistent, but note that the method from Pilyugin and Thuan (2005) has a median offset $\sim 5\times$ that of the others. In light of this, when compiling the data from Sanders *et al.* (2012) we disregard the measurements from Pilyugin and Thuan (2005) and take a weighted average of the rest. The positions of the HII regions are shown with respect to our data in Figure 2.11.

We compute the C/M ratio as a function of gas-phase [O/H] using the bins shown in Figure 2.9. The [O/H] value for each bin is defined as the [O/H] value of the HII region closest to the average position of all PHAT stars within the bin. We chose this method rather than an interpolation because Sanders *et al.* (2012) find that the [O/H] distribution is quite clumpy. While there is a global metallicity gradient of -0.0195 ± 0.0055 dex kpc^{-1}, HII regions even ~ 2 kpc apart may have dramatically different abundances.

Panel (a) of Figure 2.12 show the resulting relationship between log(C/M) and [O/H].

Panel (b) shows the same relationship for only those bins along the major axis. There is a negative gradient, with the C/M ratio decreasing with increasing metallicity. We find the weighted

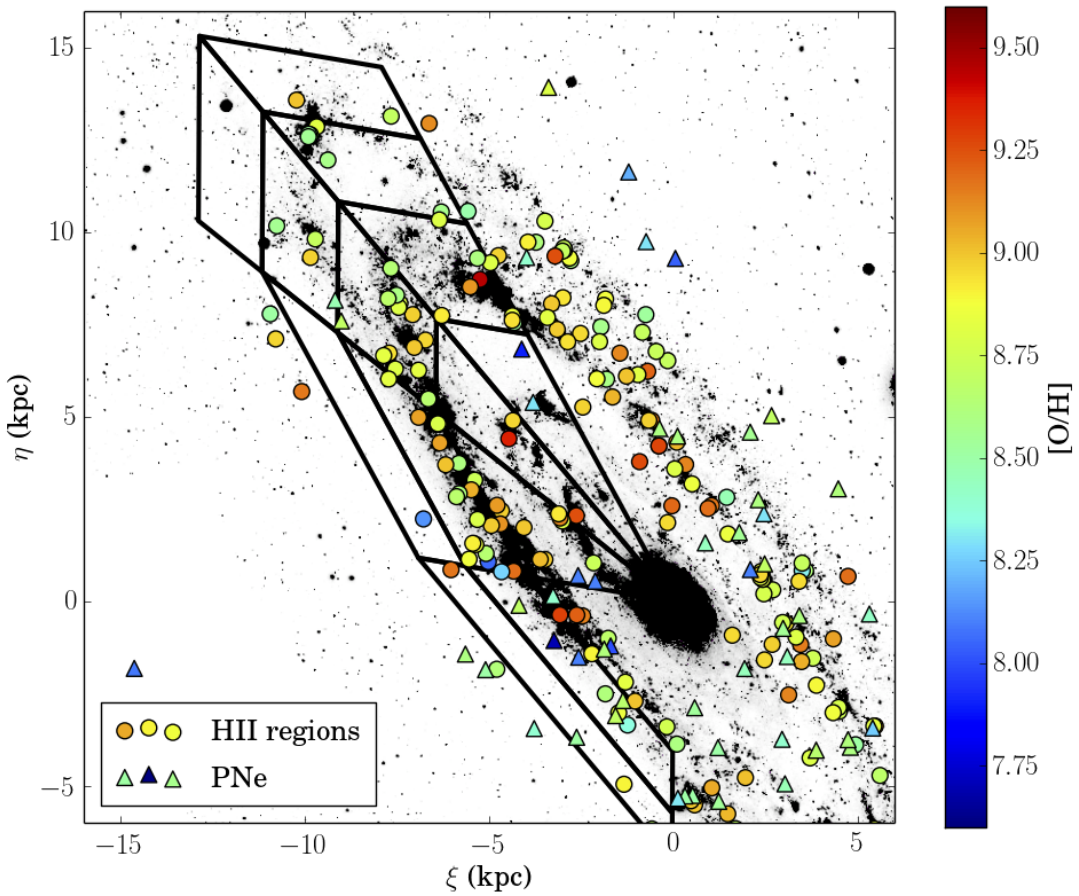

Figure 2.11: Positions of HII regions (circles) and PNe (triangles) from Sanders et al. 2012, with respect to our spatial bins (black lines). Points are colored by their oxygen abundance.

best-fit to the major axis bins to be:

$$\log(C/M_{B13}) = (-0.96\pm0.28)\times[O/H]+(7.31\pm2.48) \quad (2.5)$$

$$\log(C/M_{B95}) = (-0.95\pm0.29)\times[O/H]+(7.53\pm2.55) \quad (2.6)$$

$$\log(C/M_{BD05}) = (-0.90\pm0.29)\times[O/H]+(7.10\pm2.58) \quad (2.7)$$

HII regions probe the metallicity of present-day star forming regions and young stars, not the relevant fraction of AGB stars that formed several Gyr ago. As a result, correlations between [O/H] in HII regions and the C/M ratio tell us more about the metallicity evolution of the galaxy than the formation and evolution of the AGB stars themselves. An alternative source of gas-phase oxygen abundances are planetary nebulae (PNe), whose ages are much closer to those of AGB stars.

Sanders *et al.* (2012) compute the oxygen abundance of PNe in the disk of M31. Unfortunately, there are not enough PNe in the vicinity of our data for us to look at the C/M ratio as a function of their [O/H] measurements (see Figure 2.11). Recent work by Kwitter *et al.* (2012) and Balick *et al.* (2013) compute oxygen abundances for PNe in the outer disk of M31 ($R_g > 18$ kpc). Upcoming spectroscopic follow-up of the many PNe in the PHAT footprint (Veyette *et al.*, 2014) will provide reliable [O/H] measurements against which we can compare the C/M ratio.

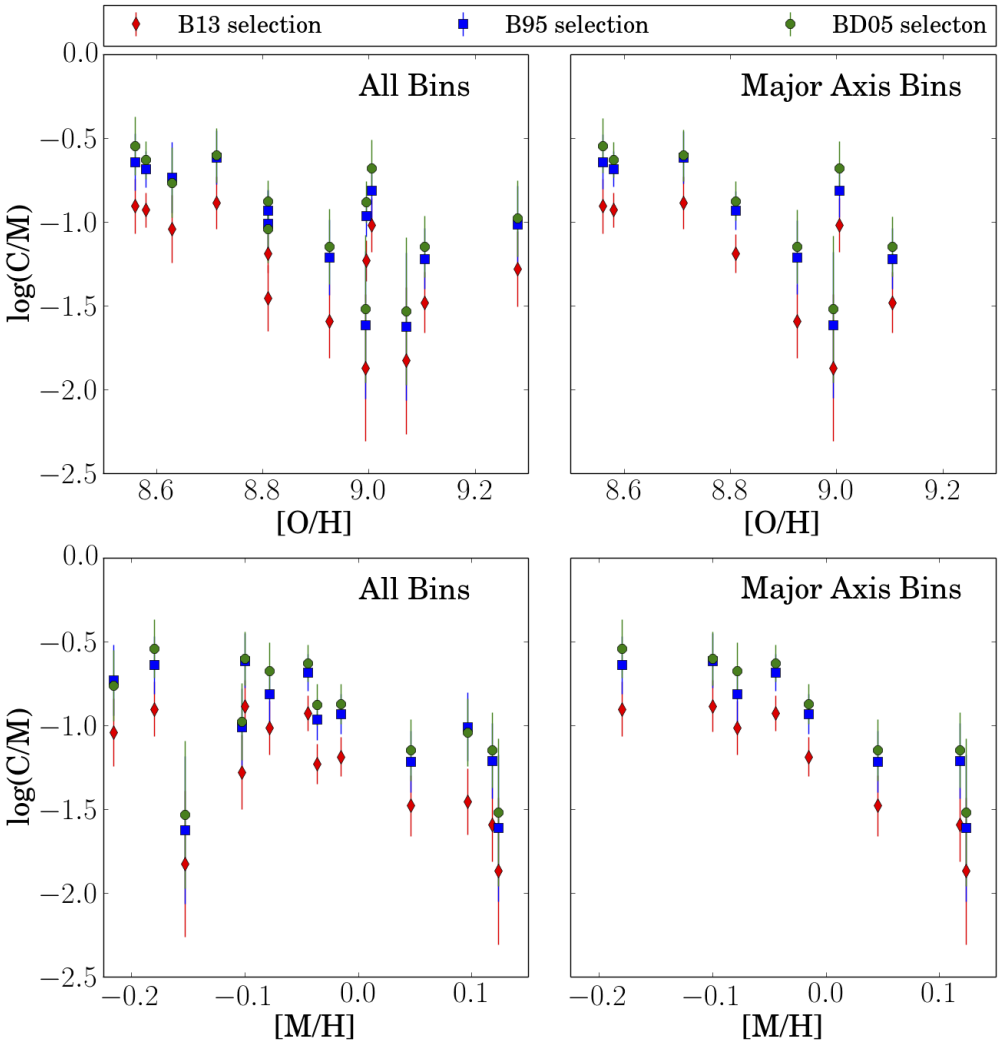

Figure 2.12: Log(C/M) vs various properties of the M31 disk. In each panel, red diamonds are calculated using the B13-based definition of M, blue squares represent the B95-based definition of M, and green diamonds represent the BD05-based definition of M. Panel (a) shows the C/M ratio vs. approximate [O/H] value at the center of each spatial bin. Panel (b) shows the C/M ratio vs approximate [O/H] value at the center of bins along the major axis only. Panel (c) shows the C/M ratio vs. mean photometric metallicity for all bins. Panel (d) shows the C/M ratio vs. mean photometric metallicity for bins along the major axis only.

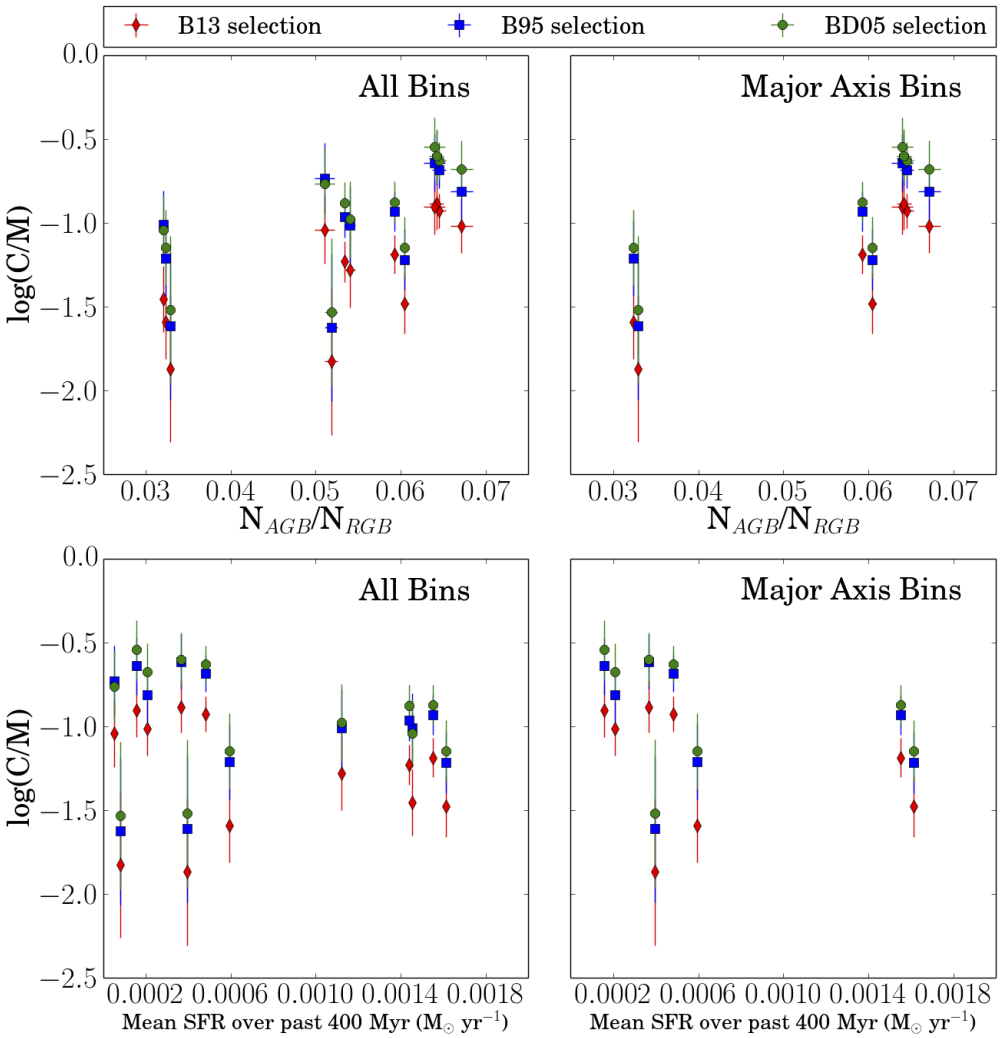

Figure 2.13: Panel (e) shows the C/M ratio vs. our age proxy, N_{AGB}/N_{RGB}, for all spatial bins. Panel (f) shows the C/M ratio against bins along the major axis only. Panel (g) shows the C/M ratio vs. the mean SFR over the past 400 Myr for all spatial bins. Panel (h) shows the C/M ratio against the mean recent SFR for bins along the major axis only.

2.4.2.2 Stellar metallicity

In addition to a gas-phase metallicity, we can study the C/M ratio as a function of stellar metallicity. We use the photometric metallicity estimates derived for RGB stars in the PHAT fields by G15. While the photometric metallicity of the RGB population may not exactly match the metallicity of the AGB population, it is a far better tracer than HII regions. In addition, we find that the combination of many more stars and more robust models makes photometric metallicity estimates derived from the RGB stars much more reliable than those we can derive using the spectra of our AGB stars.

G15 determine stellar metallicities by interpolating bias and completeness corrected photometry onto Padova PARSEC1.2s isochrones (Bressan *et al.*, 2012), with a fixed age of 4 Gyr and a metallicity range $-2.18 < [\mathrm{M/H}] < 0.6$ ($0.0001 < \mathrm{Z} < 0.06$). To avoid being heavily biased by very crowded regions, they restrict their interpolation to those stars with $F814W < 23$. In the outer regions of the disk this cut corresponds to 100% completeness, while in innermost regions it marks $\sim 50\%$ completeness. Within the spatial bins shown in Figure 2.9, we compute the mean metallicity of all RGB stars satisfying the aforementioned magnitude and metallicity criteria. We leave out the metallicities of stars in PHAT Brick 1, where we have no spectra, so as not to artificially boost the average metallicity of the innermost bins beyond what is representative of our spectral data.

Figure 2.12, panel (c), shows log(C/M) as a function of mean metallicity for all spatial bins. Panel (d) shows the relationship for only those bins along the major axis. We see a statistically significant negative gradient in C/M with photometric metallicity. A weighted best-

fit to the spatial bins along the major axis returns

$$\log(C/M_{B13}) = (-2.84\pm0.75)\times[M/H]-(1.21\pm0.06) \quad (2.8)$$

$$\log(C/M_{B95}) = (-2.63\pm0.78)\times[M/H]-(0.95\pm0.07) \quad (2.9)$$

$$\log(C/M_{BD05}) = (-2.71\pm0.79)\times[M/H]-(0.89\pm0.07) \quad (2.10)$$

G15 note that the radial metallicity gradient computed from photometric RGB metallicities depends on the underlying age distribution, and provide median metallicity measurements for several fiducial ages. To test the dependence of the C/M ratio on age assumptions, we compute the gradient in log(C/M) with photometric metallicity for fiducial ages of 6 Gyr and 8 Gyr. For the B13 method, we find slopes of -2.78 ± 0.73 and -2.73 ± 0.72, respectively, which is perfectly consistent with the slope determined for a fiducial age of 4 Gyr.

In addition to depending on the underlying age distribution, the metallicity determinations from G15 are affected by the choice of isochrones, low level dust extinction throughout the survey region, and any uncorrected photometric bias and completeness. As a result, the absolute metallicity measurements have large uncertainties.

2.4.3 As a function of SFH

In addition to being a function of metallicity, the C/M ratio should depend on a galaxy's SFH. For a single-burst stellar population, the C/M ratio begins to increase from zero once turn-off masses reach 3-4 $M_{\odot}$. For ages older than a few Gyr, carbon stars are no longer produced and the C/M ratio falls again to zero. The exact age at which the C/M ratio peaks

is determined by star formation rate (SFR) and metallicity (Cioni *et al.*, 2006; Marigo *et al.*, 2013). In a galaxy, this behavior is convolved with the SFH and smoothed. Using PHAT data, we can evaluate the C/M ratio as a function of population age and SFR.

While the exact ages of the AGB stars in M31 are difficult to compute, we can use the PHAT data to define a rough proxy. Again, we use the spatial bins shown in Figure 2.9. We define our proxy to be the number of TP-AGB stars in a given bin divided by the number of RGB stars (N_{AGB}/N_{RGB}). The value of this quantity as an age proxy relies on the fact that the mean progenitor mass of TP-AGB stars is larger, and hence younger, than that of RGB stars. A higher number ratio of TP-AGB stars to RGB stars implies a younger average population.

In order to be sensitive to the relative numbers of AGB and RGB stars independent of photometric completeness, we set a lower magnitude limit of $F814W = 23$. We also leave out the data from PHAT Brick 1, so as not to be biased by the crowded bulge in which we have no spectra. With the crowded regions inward of $R_g \sim 4$ kpc left out, our magnitude limit represents 100% completeness in our bins. We also set a color limit of $F475W - F814W \geq 2$ to mitigate contamination by younger helium burning stars (see § 2.2.4).

A plot of our age proxy as a function of R_g is shown in Figure 2.14. As this verification does not require SPLASH data, whose smaller numbers limit how small we can bin, Figure 2.14 is made with polar bins created by splitting M31 into 31 equal-area bins rather than the thirteen shown in Figure 2.9. As expected in the regime of hierarchical galaxy formation, we see that populations are younger as you move farther out in the disk.

Figure 2.12, panel (e), shows log(C/M) as a function of this age proxy computed in all spatial bins shown in Figure 2.9 . Panel (f) shows the same for bins along the major axis.

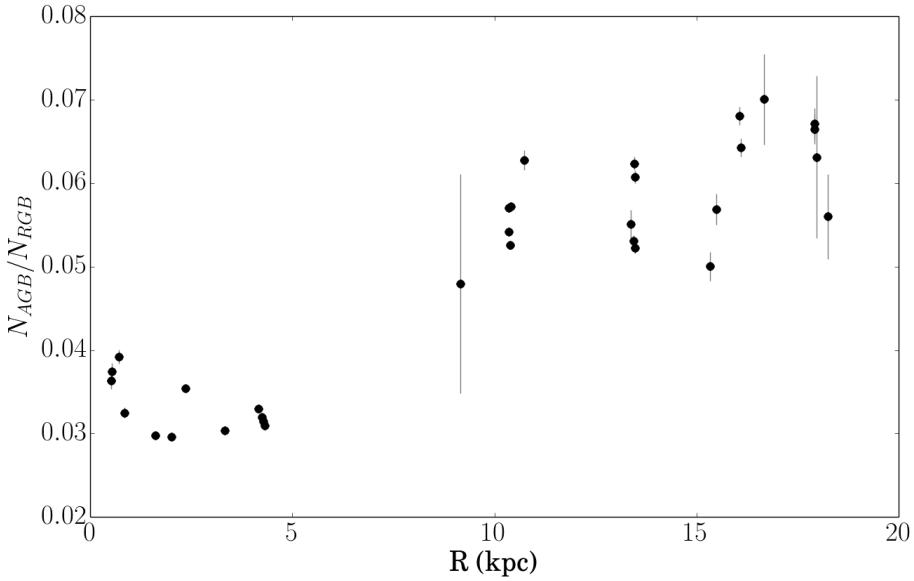

Figure 2.14: Age proxy (N_{AGB}/N_{RGB}) as a function of R_g in kpc. Error bars represent 1σ Poisson uncertainties.

The weighted best-fit lines to bins along the major axis are:

$$\log(C/M_{B13}) = (22.5\pm6.5)\times\frac{N_{AGB}}{N_{RGB}}-(2.46\pm0.40) \quad (2.11)$$

$$\log(C/M_{B95}) = (18.8\pm6.6)\times\frac{N_{AGB}}{N_{RGB}}-(1.98\pm0.40) \quad (2.12)$$

$$\log(C/M_{BD05}) = (19.1\pm6.6)\times\frac{N_{AGB}}{N_{RGB}}-(1.93\pm0.40) \quad (2.13)$$

We next look at the C/M ratio as a function of recent SFR, using data from Lewis *et al.* (2015, hereafter L15). L15 apply the CMD fitting program MATCH (Dolphin, 2002) to PHAT data in over 9000 regions in the disk of M31, and compute SFRs and cumulative stellar mass formation. To minimize the effect of model uncertainties their analysis focuses solely on

the main sequence, and so probes the SFH of M31 over the last 400 Myr. While this timescale does not match the period during which the bulk of the AGB stars formed, both models and observations predict TP-AGB stars in populations as young as 100 Myr (e.g., Frogel *et al.*, 1990).

We take each of the 9000 regions investigated by L15 and group them by the spatial bins shown in Figure 2.9 to compute a mean SFR. Log(C/M) as a function of mean recent SFR is shown in Figure 2.12 for all bins (panel g) and for bins along the major axis (panel h). There is considerably more scatter in these relationships than we saw for gas-phase oxygen abundance, stellar metallicity, or age proxy. However a weighted best-fit line to major axis bins indicates a statistically significant negative correlation.

$$\log(\mathrm{C/M_{B13}}) = (-238\pm95)\times\overline{\mathrm{SFR}}-(0.91\pm0.09) \quad (2.14)$$

$$\log(\mathrm{C/M_{B95}}) = (-229\pm98)\times\overline{\mathrm{SFR}}-(0.67\pm0.09) \quad (2.15)$$

$$\log(\mathrm{C/M_{BD05}}) = (-241\pm99)\times\overline{\mathrm{SFR}}-(0.59\pm0.09) \quad (2.16)$$

2.5 Discussion

2.5.1 The C/M ratio vs. environment

We find statistically significant trends between log(C/M) and each of the five properties we investigate: R_g, present-day gas-phase [O/H], stellar [M/H], age proxy, and recent SFR. In each case, the gradient is made clearer by restricting the analysis to the eight spatial bins along the major axis. This is likely due to the increased uncertainty in the deprojection along

Table 2.2: Coefficients of Multiple Regression Models

	[O/H]	[M/H]	N_{AGB}/N_{RGB}	SFR	R
Model 1		-2.25 ± 0.95	9.61 ± 7.7		
Model 2	-0.59 ± 0.24	-0.99 ± 0.86	11.4 ± 4.9		
Model 3		-1.79 ± 1.48	12.5 ± 9.8	-67.6 ± 149	
Model 4		-1.72 ± 1.54			0.04 ± 0.03
Model 5	-0.64 ± 0.17				0.05 ± 0.01
Model 5		-2.38 ± 1.92	10.6 ± 16.2		-0.01 ± 0.07

Note. — Rows separate individual regression models, and columns represent which parameters were used in each model (gas-phase oxygen abundance [O/H], stellar metallicity [M/H], age N_{AGB}/N_{RGB}, mean SFR over the past 400 Myr, or galactocentric radius R_g). A blank entry indicates that the parameter was not used in that particular regression model.

the minor axis rather than an azimuthal change in the behavior of the C/M ratio.

The clearest trend we see is between log(C/M) and radius. Our slopes (~ 0.06) are perfectly in line with the gradients observed by B95 (excluding their measurement at ~ 30 kpc) and Battinelli *et al.* (2003) along the opposite axis of the M31 disk. While there is no reason the C/M ratio should depend on geometry, this correlation points to a significant relationship between the C/M ratio and properties that themselves vary with radius.

B13 measure the C/M ratio in the inner disk of M31 ($R_g = 2$ kpc), and find a C/M ratio much lower than predicted given the metallicity at that radius. They interpret this as an indication of a metallicity ceiling above which carbon stars do not form. If we extrapolate our radial gradient to $R_g = 2$ kpc, we calculate log(C/M)$= -1.81 \pm 0.22$. This is considerably higher than the value measured by B13 (log(C/M)$= -3.48^{+0.85}_{-0.01}$). If the paucity of carbon stars observed in the inner disk by B13 was due to a gradual fall off in carbon star production with increasing metallicity, then our radial gradient should extrapolate to their measurement. The fact that the

C/M ratio measured by B13 is so low is consistent with the suggestion that there is a hard metallicity limit above which carbon stars do not form.

While stellar oxygen abundance is the major driver of whether a TP-AGB star can become a carbon star, it is interesting that the [O/H] measurements from HII regions in the disk of M31 show the expected trend when they themselves do not probe the metallicity of the AGB stars. One possible explanation for the observed gradient is that the metallicities of present-day star forming regions are correlated with the metallicities of star forming regions a few Gyr ago. This would indicate that the metallicity gradient in M31 is long lived. Alternatively, the C/M ratio and present-day gas-phase [O/H] may be independent, and the observed gradient is an artifact of their shared relationship with radius.

The clear gradients we observe in log(C/M) with stellar metallicity and age are predicted by models and previous observations (e.g., Mouhcine and Lancon, 2003; Feast *et al.*, 2010; Held *et al.*, 2010; Marigo *et al.*, 2013). Our observed relationship between log(C/M) and age indicates that young populations produce more M- than C-type TP-AGB stars, which could be explained by hot bottom burning operating on the most massive TP-AGB stars. The fact that the C/M ratio increases monotonically with our age proxy indicates that the average age of the populations in all our bins are older than a few Gyr. If this were not the case, then we would see the C/M ratio turn over and begin to decrease at the bins dominated by very young populations, where stars evolving off the main sequence do not become AGB stars or remain M-type due to hot bottom burning. Average ages consistently greater than a few Gyr is consistent with recent work showing a disk-wide burst of star formation 2-4 Gyr ago (Williams *et al.*, 2015), and the age calculations by Dorman *et al.* (2015) and G15.

Our derived trend with metallicity is fully consistent with the relationship established across the Local Group ($\log(\mathrm{C/M}) \sim (-2.12 \pm 0.04) \times [\mathrm{Fe/H}]$; Cioni, 2009). The trend observed in Local Group satellites appears to extend smoothly to the metal-rich regime of M31, irrespective of their drastically different SFHs. This implies that the C/M ratio is strongly determined by the same population of intermediate-age stars in all environments, and depends only on stellar properties (metallicity and age).

This interpretation of the log(C/M)-metallicity relationship would imply that our observed gradient in the C/M ratio with recent SFR is driven by correlations between SFR, age and metallicity rather than the impact of SFR itself on AGB evolution. The alternative explanation for that trend is that star formation in M31 is long lived, and the SFR of the past 400 Myr correlates with the SFR a few Gyr ago. This correlation could occur if the global burst of star formation 2-4 Gyr ago (Williams *et al.*, 2015) was spatially heterogeneous, and the regions of the disk producing the most stars 2-4 Gyr ago also have the highest recent SFR.

To investigate whether we can decouple the effects of metallicity and age on the C/M ratio and determine the dominant factor, we construct a series of multiple regression models. Beginning with a simple linear relationship between log(C/M) and any property of the disk, analysis of variance finds that the model improvement from the addition of a second (or third) variable is insignificant. The coefficients of a sample of these models are shown in Table 2.2; none are non-zero with high confidence. This is indicative of collinearity, and that age and metallicity are so tightly coupled that we cannot claim that statistically one is more important to the C/M ratio than the other.

2.5.2 Possible effects of dust

Both ISM extinction within M31 and circumstellar dust may affect the measurement of the C/M ratio, and ISM extinction may affect our metallicity, age proxy and SFR measurements.

The C/M ratio will be affected by dust if it causes carbon stars or M-stars to be preferentially excluded from the SPLASH sample. Since we identify carbon stars spectroscopically, veiling of the prominent CN and C_2 features would make the stars unidentifiable. This is not the case for M-stars, as we identify them photometrically. However, recent models show that even the dustiest carbon stars do not have their ~ 7900Å CN feature completely veiled (Aringer et. al, private communication). It is far more likely that carbon stars escape our selection by being too dust-reddened to be visible in the optical, and are thus not targeted for spectroscopy.

To investigate the effects of interstellar dust, we use the M31 dust maps from Dalcanton *et al.* (2015) to determine the average extinction (A_V) at the position of each star. We compare the distributions of A_V at the locations of the carbon stars and M-stars via a Kolmogorov-Smirnov (KS) test, and find no significant difference. Interstellar dust is thus not likely to have a significant effect on our selection.

Circumstellar dust is known to have a major impact on the completeness of optical AGB surveys (e.g., Boyer *et al.*, 2011). Correcting for AGB stars reddened out of the optical by circumstellar dust would steepen our measured age and metallicity gradients. In the case of metallicity, this is because while dust production in carbon stars stays constant as metallicity increases, dust production in M-stars goes up (Sloan *et al.*, 2008). As metallicity increases the

number of M-stars reddened from our sample will increase faster than the number of carbon stars reddened from our sample. The gradient with age proxy will steepen because carbon stars are typically more massive than M-stars, and produce more dust. Thus as the population gets younger, and has more massive stars climbing the AGB, the fraction of carbon stars invisible in the optical will be increasingly larger than the fraction of M-stars invisible in the optical.

Because both age and metallicity decrease with radius in M31, both effects discussed above will contribute to our measuring a shallower gradient than reality.

By analyzing the A_V and the fraction of reddened stars (f_{red}) G15 determine that their median metallicity measurements are generally not dependent on dust. They do find that the high metallicities found for stars along the north-west edge of the PHAT footprint track regions of higher dust extinction, however our spatial bins are large enough that these regions make up a small fraction of the stars do not substantially bias our median metallicities.

To evaluate the effect of dust on our age proxy, we first compare the distribution of extinction values in the vicinity of the AGB and RGB stars of the PHAT sample using the dust map from Dalcanton *et al.* (2015). A KS-test indicates that we can reject the hypothesis that these populations are drawn from the same distribution of A_V. AGB stars are found in slightly dustier regions. However, we find no trend between age proxy and A_V ($R^2 = 0.09$), which indicates that this does not heavily impact our results.

L15 have taken dust into account when determining SFRs, so we will not further analyze the effect of dust on these measurements.

2.5.3 Comparing definitions of M

Throughout Section 2.4 we see that the definition of M in the C/M ratio has a significant impact on the intercept of gradients but a minimal impact on the slope. Consistently, the B95 and BD05 methods return very similar results, despite having rather different effective TRGBs. The B13 method, on the other hand, always counts more M giants and returns a lower C/M ratio. This result indicates that care must be taken when comparing values within the literature, as inhomogeneous methods lead to different absolute values of log(C/M). The fact that slopes are consistent between different selection methods while intercepts are not tells us that the population of stars not being included – the bluer "AGB" stars – are distributed evenly across the disk. As we see gradients in log(C/M) with both age proxy and metallicity, this blue population is likely not the youngest or most metal poor AGB stars, but is instead either foreground contamination or supergiants.

The major result from B13, that the C/M ratio calculated ~ 2 kpc from the center of M31 is highly discrepant with values calculated farther out in the disk, stems from a comparison between the C/M ratios calculated by the B13 and B95 methods. B13 thoroughly investigate whether this discrepancy stems from an underestimation of the number of C-stars, but do not consider whether they are overestimating the number of M-stars (relative to the studies to which they compare). We can estimate how much the B13 data point would change if the B95 criteria were applied. In our data, using the B13 definition rather than the B95 definition amounts to a difference of ~ 800 M stars, or a difference of ~ 0.35 in log(C/M). While this moves the B13 point closer to the trend fit to B95 data, it is still significantly discrepant (off by ~ 1 in

log(C/M)). However, this rough approximation does not take into account the fact that B13 use medium-band NIR photometry to count M-stars while we use optical photometry. We cannot reproduce the effectiveness of medium-band NIR photometry, which is centered on distinctive absorption features present in either C or M stars, with PHAT wide-band NIR photometry.

2.6 Conclusion

We have computed the C/M ratio in the disk of M31 using spectroscopic and photometric data from the SPLASH and PHAT surveys. An uncontaminated sample of carbon stars was identified using moderate-resolution optical spectra. M-stars were identified photometrically in three different ways, following methods used by Boyer *et al.* (2013), Brewer *et al.* (1995) and Battinelli and Demers (2005). We have calculated the C/M ratio as a function of galactocentric radius, present-day gas-phase metallicity, stellar metallicity, age (via proxy N_{AGB}/N_{RGB}), and mean SFR over the past 400 Myr.

From this, we conclude:

- The definition of “M" has a minimal effect on the slope of a relationship, but a substantial effect on the fiducial value. This adds to the body of evidence that stresses the need for homogenous samples when studying the C/M ratio as a function of other parameters.

- There are statistically significant correlations between log(C/M) and $R_{\rm g}$, present-day gas-phase [O/H], stellar [M/H], age proxy, and recent SFR.

- We reproduce the relationship between log(C/M) and stellar metallicity stated in Cioni (2009), despite working in a substantially more metal-rich environment with a drastically

different SFH.

- Age and metallicity are too closely connected to state that one is more important to the C/M ratio in M31 than the other.

Chapter 3

Carbon stars in the Satellites and Halo of M31

3.1 Introduction

Carbon stars are nominally defined as stars with more free carbon than free oxygen in their atmospheres. This excess carbon builds up via the third dredge up (TDU) process in thermally pulsating asymptotic giant branch (TP-AGB) stars. The TP-AGB stage is characterized by unstable double shell burning. TDU occurs when the He-burning shell around the AGB star's inert C+O core ignites and extinguishes the outer H-burning shell. This allows the star's outer convective envelope to penetrate the intershell region and "dredge" ^{12}C up to the surface. Over time and successive dredge ups, the ratio (C/O) of ^{12}C to ^{16}O increases, eventually exceeding unity. The stars in which C/O$>$ 1 are carbon stars (C-stars).

However, carbon stars have been observed at luminosities below the (mass) limit necessary for TDU. This ever growing population of faint carbon stars includes CH stars, dwarf carbon (dC) stars, and carbon enhanced metal poor (CEMP) stars. These faint stars are the-

orized to have received their carbon via accretion from a carbon-rich AGB companion rather than internal processes (de Kool and Green, 1995; Frantsman, 1997; Izzard and Tout, 2004). Faint carbon stars are thus often termed “extrinsic", in contrast to their “intrinsic" TP-AGB counterparts.

Carbon stars make very unique tracers of particular stellar populations. Carbon-rich TP-AGB stars are easily identified photometrically or spectroscopically, and are more difficult to confuse with other tracer populations (e.g., as is the case between blue stragglers and blue horizontal branch stars). As a result, they have been used to map morphological structure, kinematical structure, mean age and metallicity of various hosts (e.g., Rowe *et al.*, 2005; Battinelli and Demers, 2005; Demers and Battinelli, 2007; Cioni *et al.*, 2008; Huxor and Grebel, 2015). These stars also trace intermediate-age populations, and so have been used to constrain the star formation histories of various Local Group objects (Grebel, 2007, and references therein). Extrinsic carbon stars provide information about earlier generations of AGB stars as well as the binary systems in which they are found.

Both intrinsic and extrinsic carbon stars have been identified throughout the Local Group. There have been dedicated carbon star surveys, or AGB surveys for which carbon stars share priority with oxygen-rich M-stars, using photometry in the optical (e.g., Albert *et al.*, 2000; Nowotny *et al.*, 2001, and subsequent papers in these series), near-infrared (e.g., Cioni and Habing, 2005; Whitelock *et al.*, 2006; Battinelli *et al.*, 2007) and mid-infrared (e.g., Blum *et al.*, 2006; Boyer *et al.*, 2011; Woods *et al.*, 2011). In addition, non-dedicated surveys have been mined for carbon stars, AGB or otherwise (e.g., Margon *et al.*, 2002; Green, 2013; Hamren *et al.*, 2015). In many nearby dwarf galaxies, and various fields in the Milky Way (MW) halo,

these surveys have enabled detailed abundance studies (e.g., Abia *et al.*, 1993, 2002). However, the more distant satellite galaxies associated with M31 are fainter, and often difficult to distinguish from the MW foreground and the M31 halo. As a result, studies in these objects have largely been limited to C-star identification and the ratio (C/M) of carbon- to oxygen-rich TP-AGB stars.

Recent advances have made these previously under-studied regions ripe for further attention. Large-scale surveys like the Spectroscopic Landscape of Andromeda's Stellar Halo (SPLASH; Guhathakurta *et al.*, 2005, 2006; Tollerud *et al.*, 2012; Gilbert *et al.*, 2012; Dorman *et al.*, 2012; Gilbert *et al.*, 2014; Dorman *et al.*, 2015) and the Pan-Andromeda Archaeological Survey (PAndAS; McConnachie *et al.*, 2009) have produced a wealth of spectroscopic and photometric data that can be used to study carbon stars in a uniform way. In addition, the M31 satellites have been shown via thorough characterization of their kinematical properties to be low-dispersion systems (Tollerud *et al.*, 2012; Ho *et al.*, 2012; Collins *et al.*, 2013; Tollerud *et al.*, 2013). This improves the veracity of kinematical determination of satellite membership. Finally, several M31 satellites now have star formation histories (SFHs) derived from deep *Hubble Space Telescope* (HST) images (Weisz *et al.*, 2014; Geha *et al.*, 2015) and identification of carbon stars can be put into a far broader context.

In this work we use photometric and spectroscopic data from SPLASH to study carbon stars in the satellites and halo of M31. Section 3.2 describes our dataset, including a summary of the observations, the photometric transformations and synthetic photometry used to homogenize the sample, and criteria for determining membership. Section 3.3 discusses the carbon stars themselves; identification, location, and the impact of the SPLASH selection func-

tion on the final sample. Section 3.4 looks at the photometric properties of the carbon stars, while Section 3.5 looks at their spectroscopic properties. We discuss the implications of our findings in Section 3.6.

3.2 Data

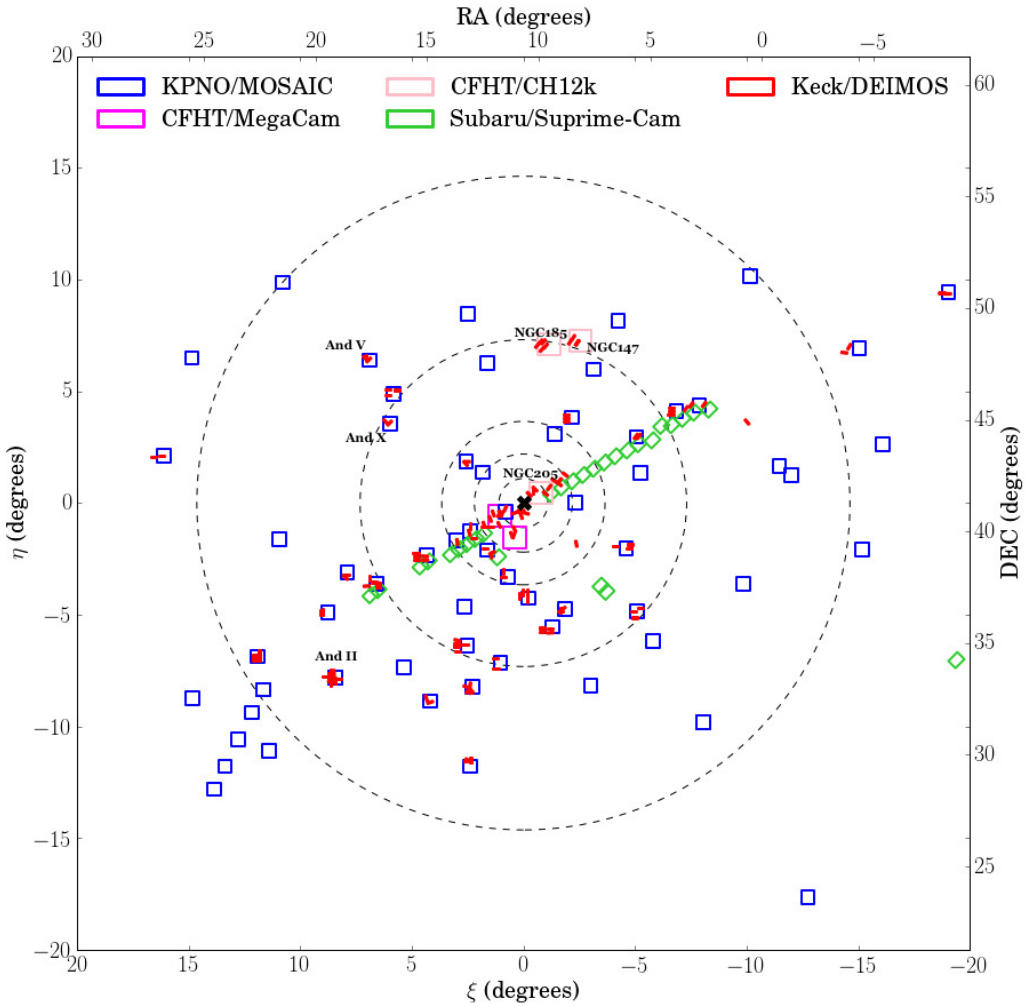

Figure 3.1: SPLASH survey map (including M32 but excluding the bright disk of M31). Footprints of the images used for spectroscopic target selection are shown to scale as blue (KPNO/MOSAIC), magenta (CFHT/MegaCam), pink (CFHT/CFH12k) or green (Subaru/Suprime-Cam) rectangles. The footprints of the DEIMOS masks are shown to scale as red rectangles. The center of M31 itself is marked as a bold black $\times$, and several of the more prominent satellite galaxies are labeled. The dashed circles represent projected radii of 15, 30, 50, 100 and 200kpc.

Table 3.1: Properties of M31 Satellites Observed by SPLASH

Satellite	RA[a]	DEC[a]	[Fe/H][a]	M_V[a]	$(m-M)_0$[a]	v_{sys} (km s^{-1})[b]	σ (km s^{-1})[b]	[α/Fe][h]	I_{TRGB}[i]
And I	00:45:39.8	+38:02:28	-1.45 ± 0.04	-11.7 ± 0.1	24.36 ± 0.07	-376 ± 2.2	10.2 ± 1.9	0.278 ± 0.164	20.36
And II	01:16:29.8	+33:25:09	-1.64 ± 0.04	-12.4 ± 0.2	24.07 ± 0.06	-192.4 ± 0.5[c]	7.8 ± 1.1[c]	0.033 ± 0.09	20.10
And III	00:35:33.8	+36:29:52	-1.78 ± 0.04	-10.0 ± 0.3	24.37 ± 0.07	-344.3 ± 1.7	0.3 ± 1.4	0.205 ± 0.16	20.40
And V	01:10:17.1	+47:37:41	-1.6 ± 0.3	-9.1 ± 0.2	24.44 ± 0.08	-397.3 ± 1.5	10.5 ± 1.1	0.119 ± 0.09	20.54
And VII	23:26:31.7	+50:40:33	-1.40 ± 0.30	-12.6 ± 0.3	24.41 ± 0.10	-307.2 ± 1.3	13.0 ± 1.0	0.296 ± 0.09	20.59
And IX	00:52:53.0	+43:11:45	-2.2 ± 0.2	-8.1 ± 1.1	24.42 ± 0.07	-209.4 ± 2.5	10.9 ± 2.0	...	20.59
And X	01:06:33.7	+44:48:16	-1.93 ± 0.11	-7.6 ± 1.0	24.23 ± 0.21	-164.1 ± 1.7	6.3 ± 1.4	0.505 ± 0.24	20.33
And XI	00:46:20.0	+33:48:05	-2.00 ± 0.20	-6.9 ± 1.3	$24.40^{+0.20}_{-0.50}$	-427.5 ± 3.5[d]	$7.6^{+4.0d}_{-2.8}$	...	20.51
And XII	00:47:27.0	+34:22:29	-2.10 ± 0.20	-6.4 ± 1.2	24.70 ± 0.30	-557.1 ± 1.7[d]	$0.0^{+4.0d}$	...	20.88
And XIII	00:51:51.0	+33:00:16	-1.90 ± 0.20	-6.7 ± 1.3	$24.80^{+0.10}_{-0.40}$	-185.4 ± 2.4	5.8 ± 2.0	...	20.89

Table 3.1 (cont'd): Properties of M31 Satellites Observed by SPLASH

Satellite	RA[a]	DEC[a]	[Fe/H][a]	M_V[a]	$(m-M)_0$[a]	v_{sys} (km s^{-1})[b]	σ (km s^{-1})[b]	[α/Fe][h]	I_{TRGB}[i]
And XIV	00:51:35.0	+29:41:49	-2.26 ± 0.05	-8.4 ± 0.6	24.33 ± 0.33	-480.6 ± 1.2	5.3 ± 1.0	...	20.51
And XV	01:14:18.7	+38:07:03	-1.80 ± 0.20	-9.4 ± 0.4	24.00 ± 0.20	-323.0 ± 1.4	4.0 ± 1.4	...	20.02
And XVI	00:59:29.8	+32:22:36	-2.10 ± 0.20	-9.2 ± 0.4	23.60 ± 0.20	-367.3 ± 2.8	3.8 ± 2.9	...	19.72
And XVIII	00:02:14.5	+45:05:20	-1.8 ± 0.1	-9.7	25.66 ± 0.13	-332.1 ± 2.7	9.7 ± 2.3	...	21.76
And XXI	23:54:47.7	+42:28:15	-1.80 ± 0.20	-9.9 ± 0.6	24.67 ± 0.13	-361.4 ± 5.8	7.2 ± 5.5	...	20.75
And XXII	01:27:40.0	+28:05:25	-1.8	-6.5 ± 9.9	24.50	-126.8 ± 3.1	$3.54^{+4.16}_{-2.49}$	...	20.56
NGC 147	00:33:21.1	+48:30:32	-1.1 ± 0.1	-14.6 ± 0.1	24.15 ± 0.09	-193.1 ± 0.8[e]	16 ± 1[e]	0.356 ± 0.10	20.35
NGC 185	00:38:58.0	+48:20:15	-1.3 ± 0.1	-14.8 ± 0.1	23.95 ± 0.09	-208.8 ± 1.1[e]	24 ± 1[e]	0.120 ± 0.09	20.12
NGC 205	00:40:22.1	+41:41:07	-0.8 ± 0.2	-16.5 ± 0.1	24.58 ± 0.07	-246 ± 1[f]	35 ± 5[f]	...	20.73
M32	00:42:41.8	+40:41:55	-0.25	-16.4 ± 0.2	24.53 ± 0.21	$-196.9^{+5}_{-4.9}$[g]	$29.9^{+5.2}_{-4.6}$[g]	0.425 ± 0.32	21.15

Table 3.1 (cont'd): Properties of M31 Satellites Observed by SPLASH

Satellite	RA[a]	DEC[a]	[Fe/H][a]	M_V[a]	$(m-M)_0$[a]	v_{sys} (km s^{-1})[b]	σ (km s^{-1})[b]	[α/Fe][h]	I_{TRGB}[i]

a - McConnachie (2012), b - Tollerud *et al.* (2012), unless otherwise noted, c - Ho *et al.* (2012), d - Collins *et al.* (2013), e - Geha *et al.* (2010), f - Geha *et al.* (2006), g- Howley *et al.* (2013), h - Vargas *et al.* (2014), i- Calculated in this work.

3.2.1 Spectroscopic and Photometric Observations

Our spectroscopic and photometric data were obtained over $\sim$ 10 years as part of the SPLASH survey. In this paper, we focus on the subset of SPLASH data that excludes the bright disk of M31. This includes fields targeting the dSphs, dEs, the smooth virialized halo, halo substructure, and M32. The extent of these observations are shown in Figure 3.1. These data include 14143 stellar spectra taken with the DEIMOS multi-object spectrograph on the Keck II 10m telescope. These spectra are spread across 151 individual DEIMOS masks, targeting $\sim$ 60 separate fields (red rectangles on Figure 3.1).

The SPLASH spectroscopic selection functions vary significantly from field to field, as the observations were conducted with specific science goals in mind that varied from field to field rather than following the strict guidelines of an overarching homogenous survey. As a result, we will not go into details regarding those selection functions in this section. Instead, we will discuss the selection functions to the extent that they affect the identification of carbon stars in Section 3.3.2.

3.2.1.1 dSphs

SPLASH has observed 16 of the dSphs in the M31 system: And I, And II, And III, And V, And VII, And IX, And X, And XI, And XII, And XIII, And XIV, And XV, And XVI, And XVIII, And XXI, and And XXII. The properties of these dSphs relevant to this analysis are shown in Table 3.1.

The majority of these spectra were targeted using Washington photometry (M, T_2, and DDO51) taken with the Mosaic Camera on the Kitt Peak National Observatory (KPNO)

4m Mayall telescope. The DDO51 filter is centered on Mg absorption features (Mgb) that are highly dependent on surface gravity, and so allows for the discrimination of M31 giant stars from MW foreground dwarf stars (Majewski *et al.*, 2000; Gilbert *et al.*, 2006). We selected spectroscopic targets using the $M-\mathrm{DDO51}$ versus $M-T_2$ color-color diagram. The spectra in And X were targeted using Sloan Digital Sky Survey (SDSS) imaging (Adelman-McCarthy *et al.*, 2006). SDSS imaging was also used to supplement the Washington photometry imaging for And II. The spectra in And XV and And XVI were targeted using archival Canada-France-Hawaii Telescope (CFHT) imaging. Finally, the spectra in And XVIII and And XXII were targeted using B- and V-band imaging from the Large Binocular Telescope (LBT).

All spectra were observed with the 1200 line mm^{-1} grating with a central wavelength of 7800 Å. This configuration has a dispersion of 0.33 Å pixel^{-1}, and a wavelength range from Hα to the Calcium II triplet at 8500 Å. The typical integration time was 3600 s per mask.

For further descriptions of the original observations, we refer the reader to Majewski *et al.* (2007, And XIV), Kalirai *et al.* (2009, And X), Kalirai *et al.* (2010, And I and III), Ho *et al.* (2012, And II), and Tollerud *et al.* (2012, the remainder). There are 3778 stellar spectra from dSph fields. All have associated Washington M, T_2 and DDO51 photometry (either used to target or taken after spectroscopic observations).

3.2.1.2 dEs

In addition to the dSphs, our dataset contains SPLASH observations of the three dEs of M31: NGC 147, NGC 185 and NGC 205. The properties of these dEs relevant to this analysis are shown in Table 3.1.

Spectra were targeted using CFHT CFH12K mosaic R and I band imaging (Battinelli and Demers, 2004a,b). Priority was assigned based on apparent I-band magnitude, with highest priority assigned to stars between $20.5 \leq I_0 \leq 21$. To minimize contamination by foreground MW dwarfs, stars were required to have $(R-I) > 0.2$.

For the purposes of this work, we used the 12 masks designed to be observed in a conventional mode, with grating and exposure times matching the observations of other SPLASH fields (see § 3.2.1.1). The final mask (n205-4m) was designed for use with a blocking filter centered on the CaT region at 8500Å. Since it did not cover the wavelength range necessary to identify carbon stars, it was excluded.

For further descriptions of the original observations, we refer the reader to Geha *et al.* (2006, NGC 205) and Geha *et al.* (2010, NGC 147 and 185). In total, there are 1924 stellar spectra from dE fields with corresponding R and I magnitudes. In addition, these stars have CN and TiO narrow-band photometry, which will be discussed in greater detail later.

3.2.1.3 M32

SPLASH has also observed the compact elliptical (cE) galaxy M32. It's relevant properties are also listed in Table 3.1. The photometry for identifying spectroscopic targets was archival CFHT data imaged with MegaCam in the g', r' and i' bands. Heavy crowding means that the g'- and r'-band images were unreliable, so i'-band data drove the target selection. The greatest weight was given to unblended photometric sources with $20.5 \leq I_o < 21$.

All masks were observed with the same configuration described in § 3.2.1.1. For further details on the observations, we refer the reader to Howley *et al.* (2013). In total, there

are 1418 stellar spectra with i'-band magnitudes.

3.2.1.4 M31 Halo

The remaining SPLASH fields target the halo of M31, including areas of known substructure (Guhathakurta *et al.*, 2006; Kalirai *et al.*, 2006a; Gilbert *et al.*, 2007, 2009a) and areas that are relatively smooth. The majority of these fields were targeted using KPNO Washington photometry, allowing for efficient separation of M31 giants and MW dwarfs (Beaton, 2014). Additional photometry includes V- and I-band images taken with the William Herschel Telescope (Zucker *et al.*, 2007), V- and I-band images taken with the Subaru Telescope's Suprime-Cam (Tanaka *et al.*, 2010), and g' and i' images (transformed to Johnson-Cousins V and I) taken with CFHT's MegaCam.

Spectra were observed using the standard SPLASH configuration (see § 3.2.1.1). For further description of these observations, see Gilbert *et al.* (2012), and references therein. There are 7023 stellar spectra in our halo fields; 3451 in fields containing substructure and 3572 in fields probing the smooth, virialized halo.

3.2.2 Synthetic Photometry and Photometric Transformations

The fields outlined above have been observed in a variety of filters: M, T_2, V, I, R, CN and TiO. To homogenize our dataset, we perform a series of photometric transformations to ensure that whenever possible stars have the equivalent of V, I and R-band photometry. The Washington photometry filters M and T_2 are nearly identical to Johnson Cousins V and I. To convert from one to the other, we apply the transformation established by Majewski *et al.* (2000). To

transform V to R, we use the transformation between $R-I$ and $V-I$ established for red and "very red" stars by Battinelli and Demers (2005). This relationship is color dependent, with the break point at $V-I=1.7$. After transforming $V-I$ to $R-I$, we add the I-band magnitude to extract R on its own. To transform R to V, we apply the same equations in the opposite direction. We do not further transform V and I into M and T_2, simply because the Washington photometry filters are less commonly used in the literature and we do not require them for comparison. Typical uncertainties of the transformed photometry are 0.09 mag in V and 0.02 mag in R. In contrast, the typical uncertainties of the raw photometry are 0.04 mag in V and 0.05 mag in R.

We also calculate synthetic CN and TiO magnitudes. CN and TiO are narrow-band filters centered at 8120.5Åand 7778.4Å, respectively. The CN filter is centered on the CN band in carbon-stars and a continuum region of M-stars, while the TiO filter is centered on the TiO band in M-stars and a continuum region of C-stars. CN–TiO color can thus distinguish between C- and O-rich TP-AGB stars. Indeed many of the photometric surveys of AGB stars in the Local Group have used a broad band color and CN–TiO color to identify carbon stars (the four-band photometry system, FBPS; Wing, 1971). Broad-band photometry has too low spectral resolution to contain the detailed spectral information provided by narrow-band filters, so we instead compute synthetic CN and TiO magnitudes by weighting the spectra with CFHT/CH12k CN and TiO throughput curves (see a full discussion of this method in Hamren *et al.*, 2015).

3.2.3 Membership

We would like to confirm whether the carbon stars identified in this paper are members of an M31 satellite, the M31 halo/extended disk, or the halo of the MW. To do this, we take

advantage of the membership criteria established by the SPLASH team.

Membership in the halo and substructure fields is determined via the likelihood estimates from Gilbert *et al.* (2006), which uses radial velocity, the equivalent width of the Na I line at 8190.5Å (EW_{NaI}), position in M-DDO51 versus $M-T_2$ color-color space, position in I versus $V-I$ color-magnitude space, and estimated [Fe/H] to determine the probably that a given star belongs to the M31 RGB or the MW foreground. Likelihood classes go from -3 (secure MW classification) through -1 (marginal MW classification) and 1 (marginal M31 classification) to 3 (secure M31 classification). In this work we will take those stars with likelihood greater than or equal to zero (i.e. those stars more likely to be associated with the M31 than the MW) to be M31 members. Likelihoods have also been calculated for many stars in the dSphs.

Membership in the M31 dSphs has been calculated by Ho *et al.* (2012, And II) and Tollerud *et al.* (2012, the remainder). In And II, the authors use a kinematical restriction, requiring member stars to be within 3σ of the systemic velocity of the dSph (-228 km s$^{-1} < v < -157$ km s^{-1}). They then apply a photometric and spectroscopic cut, $V-I < 2.5$ and $EW_{NaI} < 4$, to further eliminate foreground MW contamination. In the remaining dSphs, the authors calculate membership probability using the distance of the star from the center of the dSph, the distance from the fiducial isochrones in T_2 versus $M-T_2$ space, the equivalent width of Na I, and the half-light radius of the dSph.

In NGC 147 and NGC 185, membership criteria have been established by Geha *et al.* (2010), using a modification of the method set forth in Gilbert *et al.* (2006). The authors' metric uses line of sight velocity, EW_{NaI}, position with respect to isochrones in I versus $V-I$ space, and Ca II triplet-based spectroscopic metallicity.

Membership to NGC 205 is more difficult to determine: it's proximity to M31 leads to contamination from the M31 disk as well as the M31 and MW halos. As a rule of thumb, stars with velocities more negative than the systemic velocity of the dE ($v_{sys} = -246 \pm 35$ km s^{-1}) are likely M31 halo stars. Stars with velocities much less negative than the systemic velocity of the dE are likely to be foreground contamination (Geha *et al.*, 2006). While it is not used in Geha *et al.* (2006), EW_{NaI} can also be used to distinguish member stars from foreground dwarfs (e.g., Gilbert *et al.*, 2006). Here we will apply the condition that $EW_{NaI} < 3$.

It is even more difficult to conclusively determine membership in M32, which is superimposed on the M31 disk. Howley *et al.* (2013) define M32 candidate members to be stars with $-275 \leq v \leq -125$ km s^{-1}. Stars with velocities more negative than this range likely belong to either M31's disk or inner spheroid. Stars with velocities less negative than this range are likely MW foreground.

3.3 The Carbon Star Sample

3.3.1 Identification

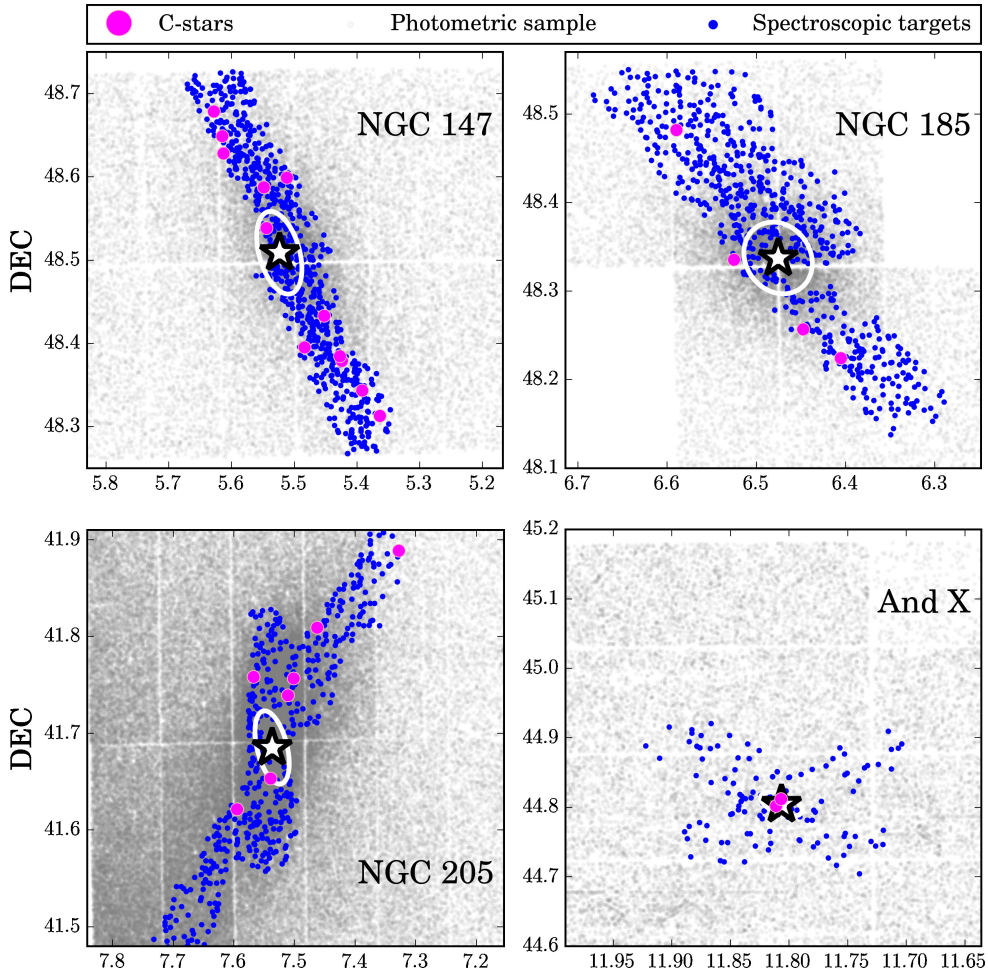

Figure 3.2: Maps of carbon stars within their host satellite. Each panel shows the RA and DEC (in degrees) of the full photometric sample (plotted in grey) and the spectroscopic sample (overlaid in blue). Carbon stars (§ 3.3) are plotted in pink. The fields have been stretched slightly to ensure that the full galaxy is visible in all panels. Each panel is annotated with the galaxy name, the galaxy center (white star), and an ellipse marking the half-light radius (obtained from McConnachie, 2012). In several fields the half-light radius is so small as to be hidden behind the star marking the galaxy center.

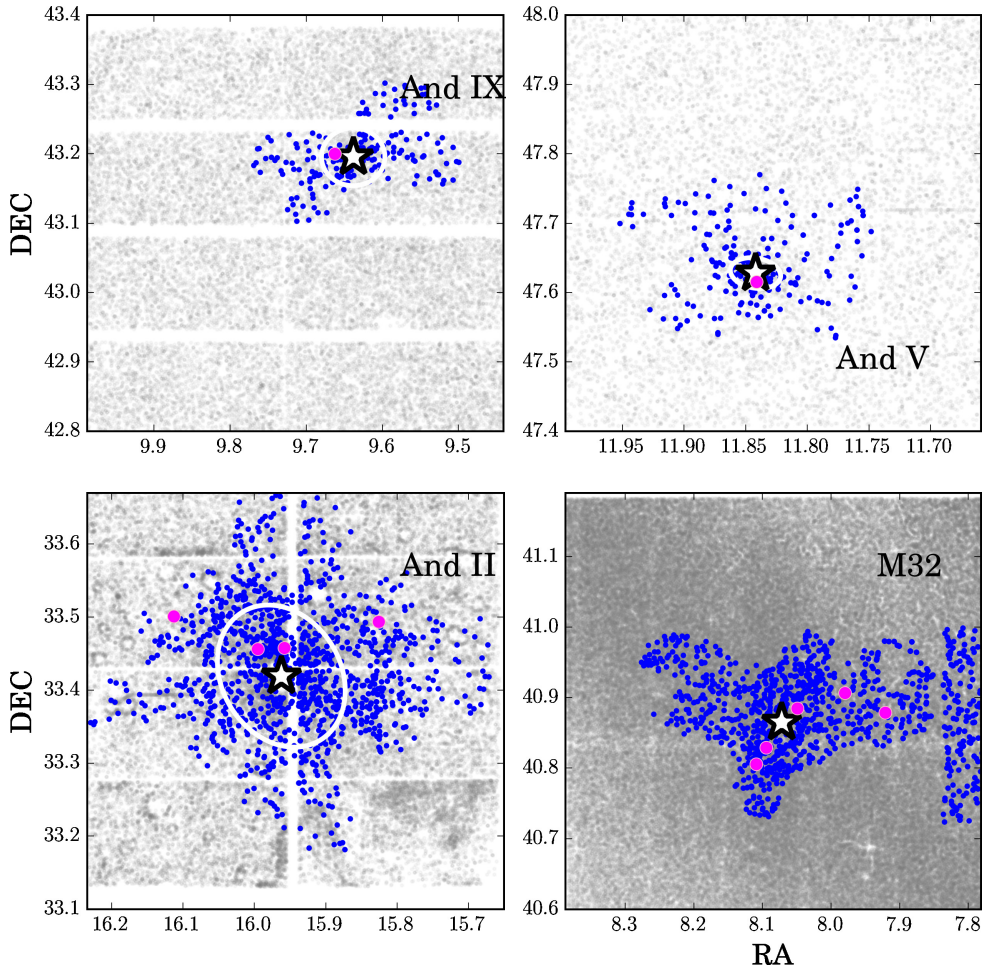

Figure 3.3: Figure 3.2, continued

Table 3.2: Carbon stars in the satellites and halo of M31

ID	Field	Field Type	RA	DEC	V	I	R	CN−TiO[‡]	$v_{\rm helio}$	Membership
1000019	And X	dSph	01:06:35.21	+44:48:06.3	22.31	21.84[†]	22.07[‡]	0.51	−184.4	And X
1000009	And X	dSph	01:06:33.77	+44:48:43.8	21.59	20.87[†]	21.22[‡]	0.59	−175.1	And X
2002324	And II	dSph	01:17:13.14	+33:30:04.6	21.52	19.72	20.63[‡]	0.37	−188.4	And II
6004761	And II	dSph	01:15:50.50	+33:29:37.9	22.49	21.19[†]	21.83[‡]	0.54	−215.8	And II
131	And II	dSph	01:16:28.58	+33:27:28.6	...	...	...	0.61	−192.9	And II
2103321	And II	dSph	01:16:39.27	+33:27:22.8	21.97	20.84[†]	21.39[‡]	0.47	−191.9	And II
6004761	And II	dSph	01:15:50.50	+33:29:37.9	22.49	21.19[†]	21.83[‡]	0.43	−215.8	And II
3005915	And V	dSph	01:10:16.79	+47:36:56.5	21.91	20.52	21.20[‡]	0.55	−412.5	And V
60001744	And IX	dSph	00:53:00.95	+43:12:00.1	22.75	21.49[†]	22.11[‡]	0.45	−221.0	And IX
240022	M32	cE	00:42:34.43	+40:53:04.7	...	20.09	...	0.39	−226.0	M32
160934	M32	cE	00:42:53.46	+40:48:20.2	...	20.46[*]	...	0.95	−2.6	MW/M31
183365	M32	cE	00:42:48.86	+40:49:45.2	...	20.02[*]	...	0.90	−15.5	MW/M31

Table 3.2 (cont'd): Carbon stars in the satellites and halo of M31

ID	Field	Field Type	RA	DEC	V	I	R	CN–TiO[‡]	$v_{\rm helio}$	Membership
263107	M32	cE	00:42:12.49	+40:54:23.2	...	20.48*	...	0.27	−448.8	M31
233791	M32	cE	00:41:53.86	+40:52:42.7	...	20.55*	...	0.61	−527.4	M31
7003	NGC 147	dE	00:32:45.10	+48:22:44.4	23.65[‡]	20.90[†]	22.42	0.71	−228.5	NGC 147
12726	NGC 147	dE	00:33:06.60	+48:23:43.7	22.66[‡]	20.55[†]	21.69	0.68	−235.2	NGC 147
4380	NGC 147	dE	00:32:23.20	+48:18:46.5	22.26[‡]	20.03	21.24	1.05	−255.4	NGC 147
5306	NGC 147	dE	00:32:33.40	+48:20:36.7	22.84[‡]	20.61[†]	21.83	0.74	−259.7	NGC 147
7187	NGC 147	dE	00:32:46.10	+48:23:04.6	22.40[‡]	20.51[†]	21.49	0.57	−269.4	NGC 147
9245	NGC 147	dE	00:32:55.30	+48:25:59.5	22.82[‡]	21.32[†]	22.05	0.43	−228.9	NGC 147
20866	NGC 147	dE	00:33:30.20	+48:35:15.5	22.31[‡]	20.13	21.31	0.73	−218.7	NGC 147
25366	NGC 147	dE	00:33:53.40	+48:37:41.7	23.05[‡]	21.50[†]	22.26	0.51	−222.9	NGC 147
25456	NGC 147	dE	00:33:54.10	+48:38:57.9	22.56[‡]	20.10	21.46	0.47	−219.2	NGC 147
25862	NGC 147	dE	00:33:59.00	+48:40:43.7	24.09[‡]	21.04[†]	22.71	0.59	−198.1	NGC 147

Table 3.2 (cont'd): Carbon stars in the satellites and halo of M31

ID	Field	Field Type	RA	DEC	V	I	R	CN–TiO[‡]	$v_{\rm helio}$	Membership
16315	NGC 147	dE	00:33:16.80	+48:35:57.9	22.57[‡]	20.65[†]	21.66	0.53	−185.8	NGC 147
os2	NGC 147	dE	00:33:28.60	+48:32:19.8	21.86[‡]	20.68[†]	21.26	0.81	−177.5	NGC 147
21924	NGC 185	dE	00:39:39.26	+48:28:55.2	23.10[‡]	21.49[†]	22.28	0.40	−245.2	NGC 185
3523	NGC 185	dE	00:38:32.78	+48:13:28.4	22.72[‡]	21.24[†]	21.97	0.57	−233.6	NGC 185
7625	NGC 185	dE	00:38:47.89	+48:15:25.7	21.82[‡]	20.04	20.93	0.52	−254.7	NGC 185
17901	NGC 185	dE	00:39:15.88	+48:20:08.2	21.86[‡]	20.03	20.97	0.40	−220.5	NGC 185
22282	NGC 205	dE	00:40:32.10	+41:45:29.4	22.69[‡]	20.51	21.69	0.63	−243.3	NGC 205
23520	NGC 205	dE	00:40:10.67	+41:45:24.7	22.91[‡]	20.59	21.86	0.71	−228.3	NGC 205
2186	NGC 205	dE	00:39:15.05	+41:53:19.8	22.62[‡]	20.66	21.69	0.74	−195.9	NGC 205
5100	NGC 205	dE	00:39:58.28	+41:48:33.2	22.99[‡]	20.55	21.89	0.63	−162.9	NGC 205
26251	NGC 205	dE	00:40:13.88	+41:44:21.4	22.72[‡]	20.86[†]	21.82	0.74	−183.9	NGC 205
80542	NGC 205	dE	00:40:23.04	+41:39:12.8	22.17[‡]	20.04	21.19	0.44	−276.3	NGC 205

Table 3.2 (cont'd): Carbon stars in the satellites and halo of M31

ID	Field	Field Type	RA	DEC	V	I	R	CN–TiO[‡]	$v_{\rm helio}$	Membership
83287	NGC 205	dE	00:40:40.70	+41:37:17.3	22.45[‡]	20.54	21.53	0.73	−423.8	M31
507513	Northeast shelf	substruct	00:50:15.66	+41:42:07.7	23.08	21.44	...	0.68	−218.0	M31
137459	Northeast shelf	substruct	00:52:14.21	+42:08:55.5	23.03	21.29	...	0.60	−315.2	M31
170544	Northeast shelf	substruct	00:52:45.74	+42:15:24.8	22.91	21.01	...	0.89	−376.1	M31
17901	Northwest shelf	substruct	00:34:42.85	+42:25:21.3	22.35	20.81	21.56	0.50	−365.4	M31

[*] i' photometry calibrated to match Johnson-Cousins I

[†] Fainter than $I_{\rm TRGB}$

[‡] Synthetic or transformed photometry, as per § 3.2.2

The optical spectra of carbon stars are distinguished by prominent CN features at $\sim 7000-8200$Å, and C_2 bands at $\sim 6100-6600$Å. Previous authors have used the CN band to identify carbon stars, either by using narrow-band filters centered on CN and its oxygen-rich counterpart TiO (e.g., Nowotny *et al.*, 2003; Battinelli and Demers, 2004b,a; Wing, 2007), or by cross-correlating spectra against templates with and without CN (Hamren *et al.*, 2015).

In this work, we identify carbon stars using the spectroscopic classification statistic demonstrated by Hamren *et al.* (2015) in the disk of M31. This method identifies carbon stars by cross correlating the spectrum in question with a suite of Milky Way templates. Spectra that are best fit by a carbon star template are flagged as likely carbon stars, and visually examined for final confirmation. We refer the reader to Hamren *et al.* (2015) for further details about the template observations and testing of the classification metric.

To make use of the high S/N carbon templates, which were observed with DEIMOS's 600 line grating, we first rebin our spectra to match the template spectra's 0.65Å pixel^{-1} dispersion. We then apply the classification statistic to the full SPLASH satellite/halo sample of 14143 stars and identify 41 carbon stars. The full list of carbon stars, including their SPLASH ID number, their position, magnitude, and velocity, is presented in Table 3.2. For the carbon stars found in the satellites, their position within the galaxy (whose center is denoted by a white X) is shown in Figure 3.2. These maps are omitted for stars in the halo fields, as there is no discernible structure or center to use as a useful reference point.

Using the membership criteria outlined in § 3.2.3, we find that all carbon stars in the dSph fields are unambiguous members of their respective satellite. The same is true for the carbon stars in NGC 185. Only two of the 12 carbon stars identified in NGC 147 fields

satisfy the full set of membership criteria outlined in § 3.2.3. However, if we take into account the rotational velocity of the dE and radial-dependent velocity dispersion (Geha *et al.*, 2006), then all the stars are within 3σ of the systemic velocity. We will thus mark all carbon stars in NGC 147 as members.

Four of the five carbon stars identified in NGC 205 have kinematics consistent with the dE. Star 83287 has a velocity of –423.8 km s^{-1}, making it more likely to be a member of the M31 halo. In M32, only star 240022 has a velocity consistent with the cE. Stars 160934 and 183365 have velocities that may indicate either foreground carbon dwarfs or stars in the tail of the M31 spheroid's kinematic distribution. Given that these masks are located on a relatively high surface brightness part of M31, picking up a foreground star (let alone a rare dC star) is unlikely. These two stars are thus more likely to belong to the M31 spheroid. Stars 263107 and 233791 have velocities consistent with either the M31 spheroid or disk.

We also identify four carbon stars in fields with known substructure, associated with M31's Northeast or Western Shelves. These shelves are debris from the Giant Southern Stream, are are known to contain AGB stars (e.g., Tanaka *et al.*, 2010).

3.3.2 Selection Functions

The presence, or lack thereof, of carbon stars in a particular field is highly dependent on the spectroscopic selection function. The identification of carbon stars was never one of the science goals of the SPLASH survey, and so the regions in color-magnitude space in which they are typically found were not always prioritized.

To estimate the number of carbon stars we might expect to observe in each field, we

begin with the assumption that our carbon stars are all TP-AGB stars brighter than the tip of the red giant branch (TRGB). To estimate the total number of TP-AGB stars in each field (N_{AGB}) we count the number of spectral targets brighter than the TRGB that have $V-I > 1.5$ (equivalently, $R-I > 0.73$). These limits are based on the region in color-magnitude space where carbon-rich TP-AGB stars are typically found, with a slightly bluer color limit designed to encompass the majority of our sample.

In the satellites, we can calculate the I-band magnitude of the TRGB using the calibration from Bellazzini *et al.* (2004) adjusted by the distance moduli listed in Table 3.1. This calibration requires [M/H] measurements, so we convert the [Fe/H] measurements in Table 3.1 using Equation 1 from Ferraro *et al.* (1999). We use the [α/Fe] measurements from Vargas *et al.* (2014) where available, and assume [α/Fe]= 0.28 (the same value used by Ferraro *et al.*, 1999) for the remainder. Finally, we correct the calculated $I_{\rm TRGB}$ for foreground extinction using the dust maps from Schlafly and Finkbeiner (2011). Our calculated $I_{\rm TRGB}$ are listed in Table 3.1. Because the i' photometry of M32 was specifically calibrated such that $i'_{\rm TRGB}$ and $I_{\rm TRGB}$ are equivalent, our calculated $I_{\rm TRGB}$ for M32 is still comparable to the i' photometry. For the halo fields, we assume that $I_{\rm TRGB}$ is located at $M_{\rm bol} = -4$, and adopt the distance modulus of M31 (24.47; Stanek and Garnavich, 1998), giving us $I_{\rm TRGB} = 20.47$.

In the fields with potential TP-AGB stars, we can estimate how many carbon stars we would expect to observe using a theoretical C/M ratio — the number ratio of carbon- to oxygen-rich TP-AGB stars. We calculate the C/M ratio in each field using the well-calibrated relationship between log(C/M) and [Fe/H] from Cioni (2009). In satellite fields, we adopt the [Fe/H] values listed in Table 3.1. In halo fields, we compute the projected line-of-sight distance

from M31, and then derive [Fe/H] value using the metallicity gradient from Gilbert *et al.* (2014).

The probability of detecting a C-star in a TP-AGB population (assuming that the region in color and magnitude space described above is populated entirely by C- and M-type AGB) is

$$P_c = \frac{1}{(C/M)^{-1} + 1} \tag{3.1}$$

Multiplying this probability by the number of likely TP-AGB stars gives us the number of carbon stars expected in each field.

Table 3.3 outlines this analysis. For each field, it lists the theoretical C/M ratio, the number of TP-AGB stars (N_{AGB}), the number of predicted carbon stars (N_{CP}), and the number of observed carbon stars (N_{CO}). We also include the projected radial distance for all fields, although it was only used in the analysis of halo fields.

There are 25 fields in which there are zero predicted C-stars and zero observed C-stars. Of these 25, five are dSphs (And XI, And XIII, And XV, And XVI and And XXII). These five dSphs are some of the least massive of our sample, where the majority of bright stars would have been put on a mask. There are four fields in which we do identify some carbon stars despite there being none predicted; And X, NE2, NE4, and NE1. These carbon stars are either fainter than the TRGB or bluer than $V-I = 1.8$, and will be discussed in detail later in this paper.

In most of the remaining fields, we observe roughly the number of carbon stars that we expect (to within a factor of two). However, in And II, NGC 147, NGC 185 and NGC 205 we observe far more carbon stars than are predicted, despite the fact that our calculated C/M

Table 3.3: Selection Function Data

Field	$N_{\rm masks}$	$D^{a}_{\rm M31,proj}$ (kpc)	Theoretical C/M	$N^{b}_{\rm AGB}$	$N^{c}_{\rm C,\ pred}$	$N^{d}_{\rm C,\ obs}$
SE8	1	3.8	0.001	0	0.00	0
SE9	1	6.0	0.001	0	0.00	0
f109	1	8.9	0.002	1	0.00	0
f1	2	12.2	0.002	1	0.00	0
NW1V	1	13.1	0.002	1	0.00	0
f116	1	13.2	0.002	1	0.00	0
f115	1	14.5	0.002	3	0.01	0
f207	1	16.3	0.002	0	0.00	0
NW1dV	1	18.0	0.003	2	0.01	0
25kpc	1	20.0	0.003	0	0.00	0
NE3	1	20.6	0.003	0	0.00	0
f123	1	21.0	0.003	0	0.00	0
f2	2	21.3	0.003	2	0.01	0
NW2V	2	21.5	0.003	1	0.00	0
NE1	1	22.8	0.003	0	0.00	1

ratios match those in the literature. As in And X and the Northeast Shelf fields, many of these stars are fainter than the TRGB and/or bluer than $V-I = 1.8$. In And I and And III, we predict several carbon stars (~ 4.5 in both fields), but do not observe any.

Table 3.3 (cont'd): Selection Function Data

Field	$N_{\rm masks}$	$D^{a}_{\rm M31,proj}$ (kpc)	Theoretical C/M	$N^{b}_{\rm AGB}$	$N^{c}_{\rm C,\ pred}$	$N^{d}_{\rm C,\ obs}$
NW2dV	1	24.2	0.004	2	0.01	0
M32	6	5.7	0.004	0	0.00	5
NE6	1	24.8	0.004	0	0.00	0
f130	2	25.3	0.004	3	0.01	0
NW3V	1	26.8	0.004	1	0.00	1
a0	3	29.8	0.005	4	0.02	0
NE4	1	32.9	0.006	0	0.00	1
g1	1	34.5	0.006	0	0.00	0
a3	3	35.4	0.006	4	0.03	0
mask4	1	36.8	0.007	0	0.00	0
f135	1	37.9	0.007	0	0.00	0
NE2	1	39.1	0.008	0	0.00	1
A240	3	55.2	0.017	0	0.00	0
A338	3	56.1	0.018	1	0.02	0
m4	5	56.6	0.018	4	0.07	0

Table 3.3 (cont'd): Selection Function Data

Field	$N_{\rm masks}$	$D^{a}_{\rm M31,proj}$ (kpc)	Theoretical C/M	$N^{b}_{\rm AGB}$	$N^{c}_{\rm C,\ pred}$	$N^{d}_{\rm C,\ obs}$
a13	4	58.0	0.019	5	0.10	0
NW9V	2	65.4	0.028	1	0.03	0
n205	3	32.6	0.056	34	1.79	7
a19	4	79.5	0.056	1	0.05	0
A220	3	85.2	0.075	2	0.14	0
m6	5	85.3	0.075	0	0.00	0
A310	3	87.1	0.082	1	0.08	0
A040	3	90.3	0.096	0	0.00	0
b15	5	91.9	0.104	1	0.09	0
NW13dV	1	92.3	0.106	0	0.00	0
NW14V	1	95.5	0.125	0	0.00	0
NW15V	1	100.3	0.158	0	0.00	0
N147	4	101.4	0.242	7	1.36	12
m8	2	116.8	0.356	1	0.26	0
N185	5	97.4	0.643	4	1.57	4

Table 3.3 (cont'd): Selection Function Data

Field	$N_{\rm masks}$	$D^{a}_{\rm M31,proj}$ (kpc)	Theoretical C/M	$N^{b}_{\rm AGB}$	$N^{c}_{\rm C,\ pred}$	$N^{d}_{\rm C,\ obs}$
d7	2	220.1	1.050	3	1.54	0
d1	2	44.8	1.342	8	4.58	0
d5	4	109.8	2.798	2	1.47	1
m11	4	158.6	2.827	2	1.48	0
A170	2	159.9	3.014	0	0.00	0
d2	12	140.5	3.403	11	8.50	5
A080	2	164.8	3.838	1	0.79	0
A305	2	169.5	4.842	0	0.00	0
d3	3	68.4	6.758	5	4.36	0
d18	1	113.0	7.453	1	0.88	0
d22	3	245.1	7.453	0	0.00	0
d15	2	93.7	7.453	0	0.00	0
d13	5	126.8	12.165	0	0.00	0
d10	2	76.7	14.091	0	0.00	2
d11	1	102.2	19.855	0	0.00	0

Table 3.3 (cont'd): Selection Function Data

Field	$N_{\rm masks}$	$D^a_{\rm M31,proj}$ (kpc)	Theoretical C/M	$N^b_{\rm AGB}$	$N^c_{\rm C,\ pred}$	$N^d_{\rm C,\ obs}$
d16	2	138.7	32.407	0	0.00	0
d12	1	114.0	32.407	1	0.97	0
d9	2	36.8	52.894	5	4.91	1
d14	1	159.8	70.968	1	0.99	0

[a] The projected distance (in kpc) of each field from the center of M31
[b] The number of likely AGB stars observed in each field (see text for details)
[c] The *predicted* number of carbon stars in each field given the total number of observed AGB stars and the theoretical C/M ratio
[d] The *observed* number of carbon stars in each field

3.4 Photometric properties

In this section we will examine the photometric properties of our sample of 41 carbon stars. Several of these stars were identified in the previous section as being fainter than the TRGB. They are located in And II, And IX, And X, and all three dEs, and are noted in Table 3.2. As these faint (sub-TRGB) carbon stars may be extrinsic in origin, we will distinguish between them and the bright (super-TRGB) sample.

The distribution of C-star magnitudes with respect to their host satellite's TRGB is shown in Figure 3.4. We restrict this figure to those C-stars within dSphs and dEs, because their distance moduli and thus TRGB estimates are far more certain than in the halo fields. Only 13 (42%) of the carbon stars in the M31 satellites are brighter than the TRGB. The uncertainty in this fraction is dominated by the uncertainties on the distance moduli, which can be as high as 0.2 magnitudes. Typical uncertainties on the I-band magnitudes of the carbon stars, on the other

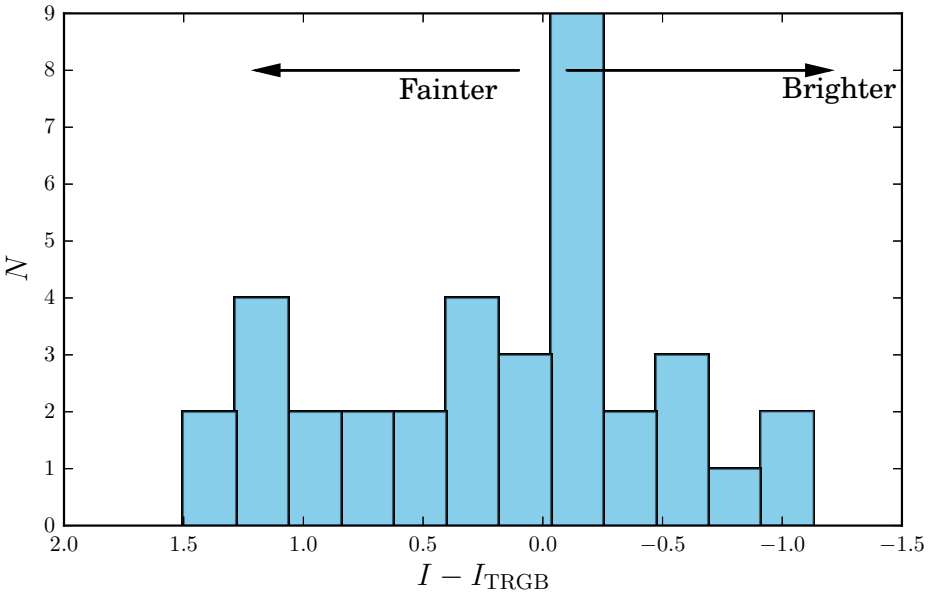

Figure 3.4: Distribution of carbon star I-band magnitude in the dEs and dSphs of our sample with respect to the TRGB of their host galaxy; 42% are brighter than the TRGB and 58% are fainter.

hand, is 0.02 ± 0.01 mag.

The bright carbon stars are concentrated close to the TRGB, with the brightest observed C-star less than one magnitude away. This may be a selection effect, as very bright stars were occasionally given low targeting priority to avoid possible foreground contamination. The remaining 18 carbon stars are fainter than the TRGB by between 0.13 and 1.5 magnitudes. Given the small number of carbon stars in each satellite, it is difficult to compare the observed carbon star luminosity function with the observed SPLASH luminosity function, and we cannot tell if carbon stars are represented down to the detection limit.

Figure 3.5 shows the distribution of colors, rather than magnitudes: $V-I$ color, representing the slope of the continuum, and CN–TiO color, representing the strength of the CN features at ~ 7900Å. We compare stars with no carbon features, carbon stars brighter than the TRGB and carbon stars fainter than the TRGB. The bulk of the faint C-stars are bluer in $V-I$ than the bright C-stars, with a distribution more like that of the non-carbon stars. However the faint carbon stars have comparable CN–TiO colors to the bright C-stars, both of which are considerably higher than the non-carbon stars. This indicates comparable strength of carbon features. The distribution of CN–TiO color for non-carbon stars overlaps slightly with the distributions of CN–TiO for both groups of carbons tars. However visual examination of the spectra shows that this to due to artifacts introduced by the sky subtraction process, and not the presence of carbon stars we failed to identify.

In addition to the one-dimensional distributions of color in Figure 3.5, it is also constructive to look at these distributions in two dimensions. Figure 3.6 shows two color-color diagrams. The left panel plots CN–TiO versus $V-I$, with the full SPLASH sample (black

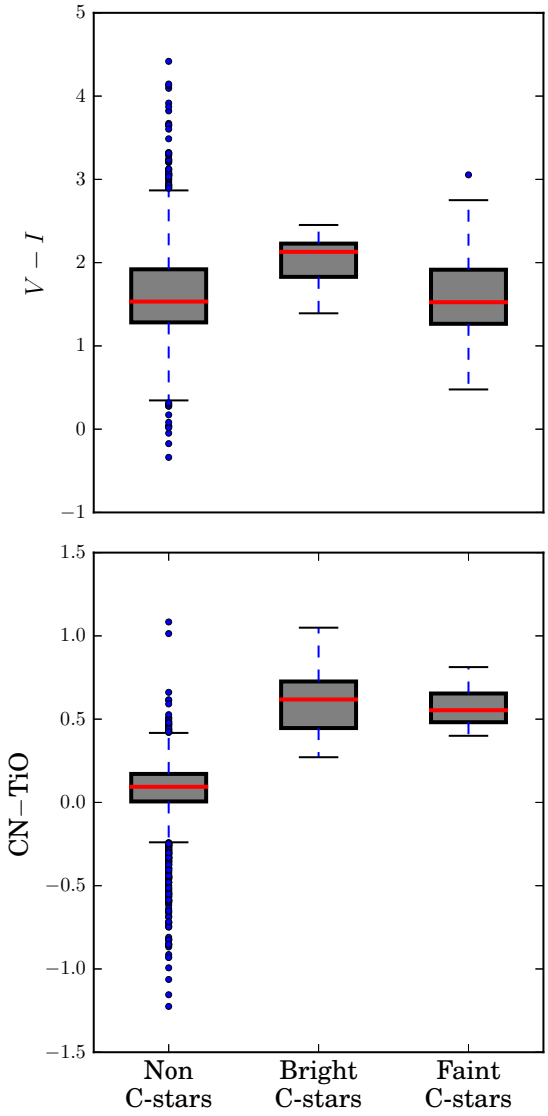

Figure 3.5: Distributions of non-carbon stars (left), C-stars brighter than the TRGB (center), and C-stars fainter than the TRGB (right) in $V-I$ (top) and CN–TiO (bottom). Solid red lines indicate the median of the distribution, grey boxes encompass the quartiles, and the whiskers extend 1.5 times the interquartile range past the quartiles. Outliers are displayed as circles. The bright C-stars are redder in $V-I$ than the faint C-stars, despite having comparable CN–TiO colors (i.e. CN band strength).

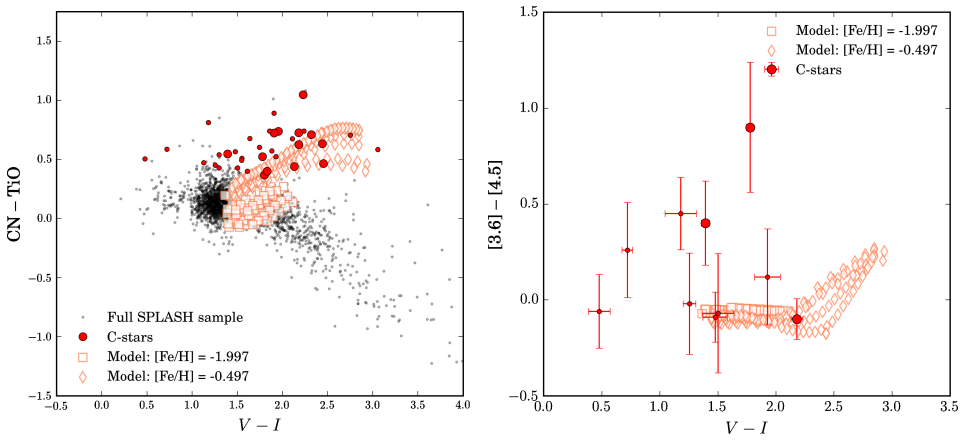

Figure 3.6: Color-color diagrams of observed and synthetic carbon stars. The left panel shows synthetic CN–TiO versus SPLASH $V-I$ color, and the right panel shows DUSTiNGS [3.6]–[4.5] versus SPLASH $V-I$. In both panels SPLASH carbon stars are shown as blue points sized by whether the star is fainter (small points) or brighter (large points) than $I_{\rm TRGB}$. Diamonds and squares represent the dust-free hydrostatic models from Aringer *et al.* (2016). On the left panel we also the full SPLASH sample as small grey points.

points) overlaid with the dust-free, hydrostatic synthetic photometry from Aringer *et al.* (2016). The carbon stars are plotted as blue points, with faint and bright stars differentiated by point size. The carbon stars are fairly consistent with the models, which indicates that they are not particularly dusty. In general, the bright C-stars (larger points) are a better fit, as many of the fainter carbon stars (smaller points) are bluer than the models. However there is not a clear dichotomy; some of the faint C-stars fit the models better than some of the bright C-stars, and visa versa. There are no stars substantially redder than the models in $V-I$. This is likely a selection effect, as the photometry with which SPLASH spectroscopic targets were selected is less complete at these colors. Indeed the sample of non-carbon stars falls off dramatically at $V-I>3$ as well.

The right panel of Figure 3.6 takes advantage of the fact that many of our dSph and

Table 3.4: Carbon stars in the DUSTiNGS sample

ID	Mask	3.6μm	4.5μm
1000019	d10_1	18.87	18.93
1000009	d10_2	19.64	19.38
131	d2_12	20.48	20.15
3005915	d5_1	19.18	18.78
60001744	d9_1	19.97	19.99
9245	N147_2	19.86	19.93
20866	N147_3	18.40	18.50
16315	N147_4	19.69	19.57
os2	N147_4	17.58	17.13
3523	N185_3	18.75	18.84
7625	N185_3	20.31	19.41

dE fields have also been imaged by the Survey of Dust in Nearby Galaxies with *Spitzer* (DUSTiNGS Boyer *et al.*, 2015). DUSTiNGS imaged 50 nearby dwarf galaxies at 3.6 and 4.5 μm using the InfraRed Array Camera (IRAC Fazio *et al.*, 2004) on the *Spitzer Space Telescope*. In total there are 1749 stars with SPLASH spectra that fall within the DUSTiNGS footprints, 11 of which are carbon stars. The 3.6 and 4.5 μm photometry of these 11 stars is shown in Table 3.4.

The right panel of Figure 3.6 displays [3.6]–[4.5] versus $V-I$. Included are the dust-free hydrostatic models from Aringer *et al.* (2016) and the photometry of the ten carbon stars with optical and MIR photometry. We have omitted the matched DUSTiNGS-SPLASH photometry for the full SPLASH sample, because it is highly biased. The SPLASH sample extends far below the DUSTiNGS detection limit, meaning that many of the matched stars are some of the faintest in the DUSTiNGS sample. Stars so close to the detection limit are more often observed when random noise makes them brighter and as the detection limit in 4.5μm is higher than in 3.6μm this translates to artificial reddening. Most TP-AGB C-stars should not be

affected by this bias.

The fit between the observed C-star photometry and the synthetic photometry is worse in [3.6]–[4.5] versus $V-I$ color-color space than it is in CN–TiO versus $V-I$. As before, while the faint carbon stars (small points) are often a poor fit to the models, there are some faint C-stars that fit the models better than the bright C-stars, and visa versa. Some of the mismatch may be due to internal stellar dynamics, as the optical and MIR photometry was taken at very different times. A one dex shift in $V-I$, at least for the bright C-stars, would lead to a far better fit to the models. This shift is well within the variation amplitude of a carbon-rich variable star, and models predict larger color amplitudes in the optical than at longer wavelengths (Nowotny *et al.*, 2011, 2013). That said, none of these stars (faint C-stars included) appear in the DUSTiNGS variable star/extreme-AGB star catalog (Boyer *et al.*, 2015) (though with only two DUSTiNGS epochs this does not definitively rule out variability). Pulsation is unlikely to be enough to explain the position of the three bluest faint-carbon stars. That these are such a poor fit to the models suggests that they are not AGB stars at all.

3.5 Spectroscopic Properties

The optical spectra of carbon stars are characterized by strong bands of CN, C_2, and CH. Of these three molecules, only CN and C_2 are visible within the wavelength range covered by the SPLASH spectra (Hα to the Ca II triplet). These features do not vary as strongly with temperature as their counterparts in oxygen-rich stars (namely TiO), and, as a result, optical carbon star spectra are remarkably uniform (e.g., van Loon *et al.*, 2005).

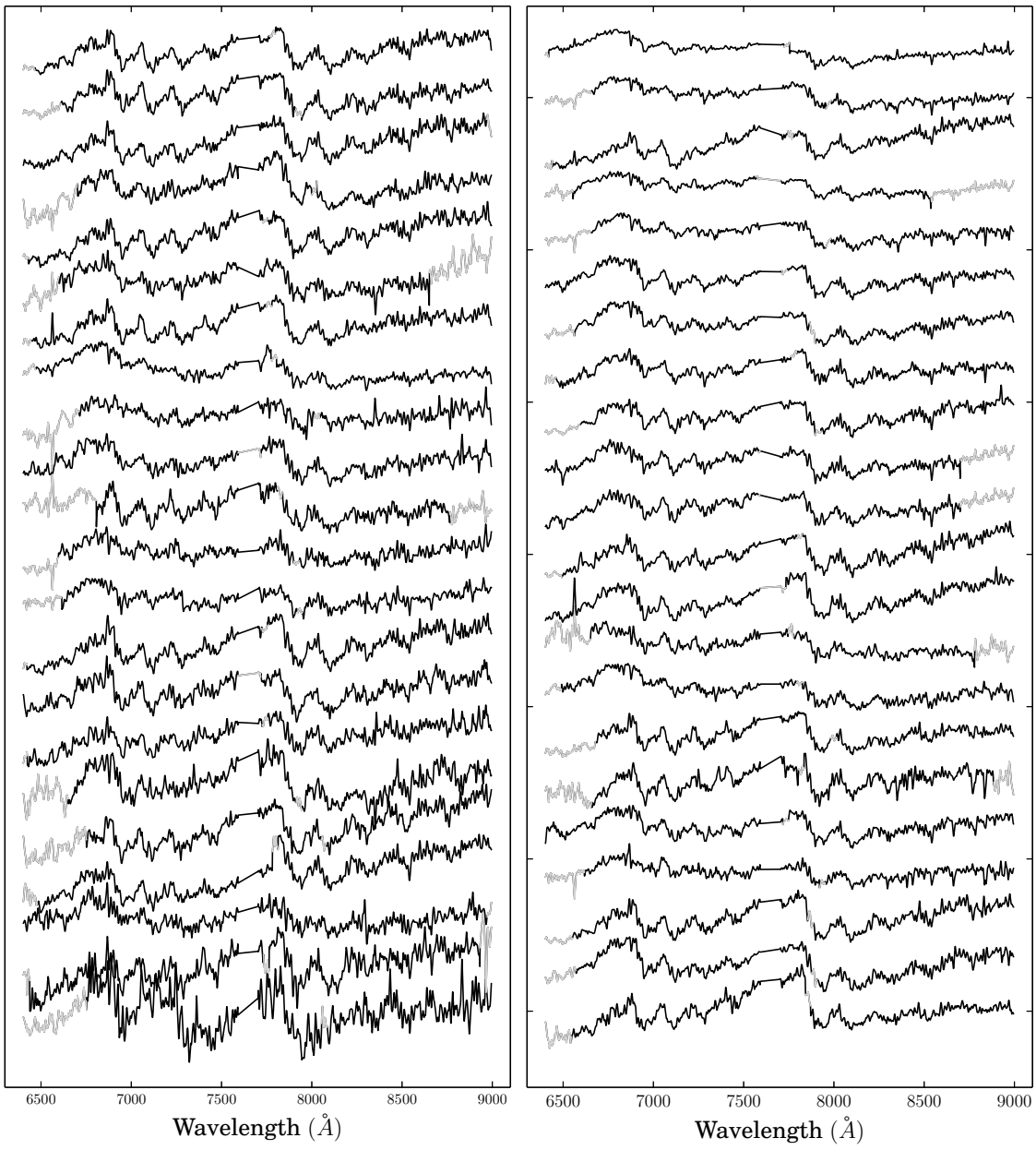

Figure 3.7: Spectra of all carbon stars in our sample, with regions of missing data reconstructed with PCA. Spectra have been smoothed by a Gaussian with σ = 1.95Å, and the telluric A-band has been replaced with a linear interpolation. Sections of the spectra that are reconstructed using eigenvectors are highlighted in grey, while the “raw" spectra are plotted in black.

To identify the fundamental components of our spectra, we apply Principal Component Analysis (PCA) to derive “eigenspectra." Broadly, PCA is a technique for dimensionality reduction, which converts a set of observations of potentially correlated properties to an orthogonal, uncorrelated, basis set. It has been used to classify the spectra of galaxies (Connolly *et al.*, 1995), quasars (Yip *et al.*, 2004), and stars (McGurk *et al.*, 2010), in addition to being widely used by other disciplines.

Briefly, eigenspectra are computed in much the same way as standard eigenvectors. We begin with a symmetric correlation matrix C, such that C_{ij} is the normalized scalar product of spectra i and j. We then find the matrix U, such that

$$U^T C U = \Lambda \tag{3.2}$$

where C is the correlation matrix, and Λ is a diagonal matrix of eigenvalues. The i-th column of U contains the i-th eigenspectrum. The “weight" of each eigenspectrum in the observed spectra is called the eigencoefficient, and is obtained by projecting the observed spectra onto the eigenspectra.

In the end, each observed spectrum can be described by the following expression

$$x_i = \mu + \sum_{j=1}^{N} a_{ij} e_j \tag{3.3}$$

where x_i is the spectrum in question, μ is the mean spectrum, e_j are the eigenspectra, and a_{ij} are the eigencoefficients.

To compute the eigenspectra, eigenvalues, and coefficients of our set of carbon stars, we use the *iterative* PCA formalism set forth by Yip *et al.* (2004, hereafter Y04) in the `astroML` Python library (Vanderplas *et al.*, 2012). Iterative PCA allows us to use successively regenerated eigenvectors to fill holes of missing data, essential for our spectra, which have variable wavelength coverage. However, iterative PCA cannot reconstruct regions in which no spectra have data. This is an issue for the telluric A-band, which was improperly corrected during data processing. Because the telluric A-band contains no stellar information, we remove it (7591 – 7703Å) and linearly interpolate across the gap. We then smooth the spectra with a Gaussian of σ = 1.95Å and perform iterative PCA with l2 normalization.

The reconstructed spectra are shown in Figure 3.7. We can see that the spectra are all very similar, but do have small differences in the strength of the CN bands and the overall slope. Very few of the spectra have measurable C_2 at 7700Å, just to the right edge of the telluric A-band masking. It is possible that this indicates that these spectra all have a fairly low C/O ratio, but it is more likely that the proximity of C_2 to the strong telluric feature has led to its being engulfed by the noise. Two of the spectra show prominent Hα emission at 6562.8Å, and an additional two show weak emission. This fraction is far lower than the $\sim$ 40% of carbon stars observed with Hα emission in the halo and satellites of the MW (Mauron *et al.*, 2007).

Figure 3.8 shows the first five carbon star eigenspectra, which account for 42% of the variance in the sample. The fifth eigenspectrum, as well as the subsequent eigenspectra not shown, is dominated by noise. Not only does it not correlate strongly with any of the physical properties shown in Figure 3.9, its eigencoefficients are all very small. With this noise, it takes 30 eigenspectra to account for 90% of the variance in the carbon star sample. Higher S/N

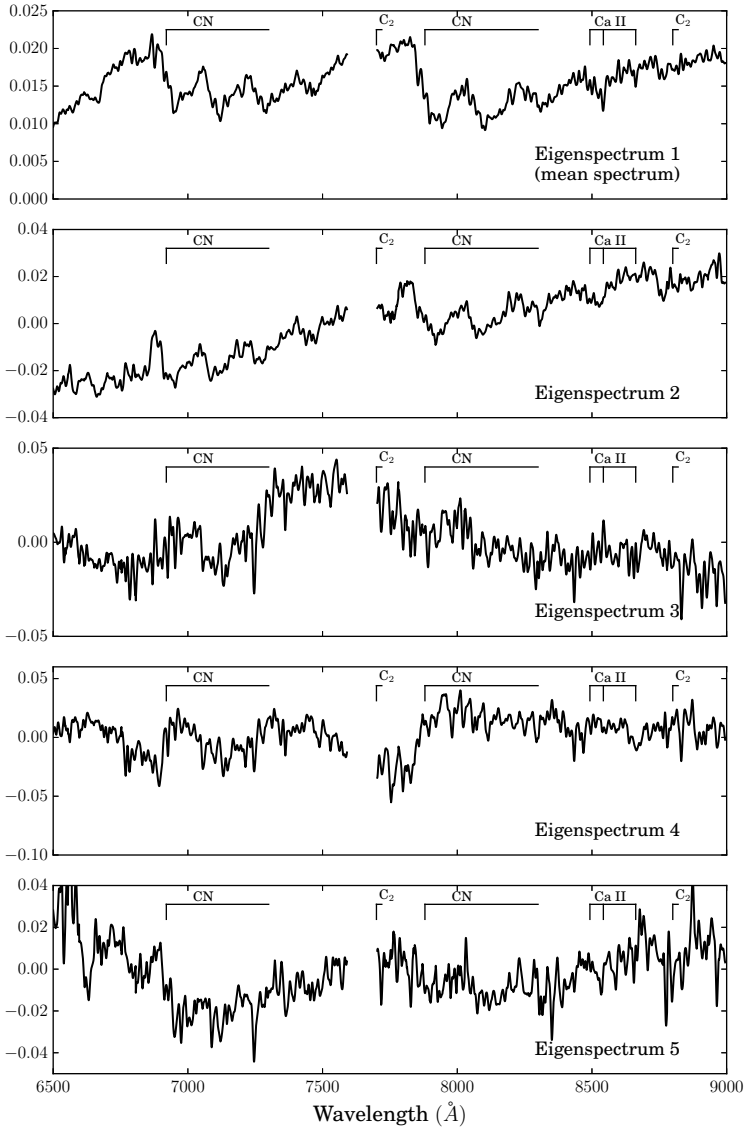

Figure 3.8: First five C-star eigenspectra. The eigenspectra are annotated with major absorption features (CN, C_2 and Ca II)

.

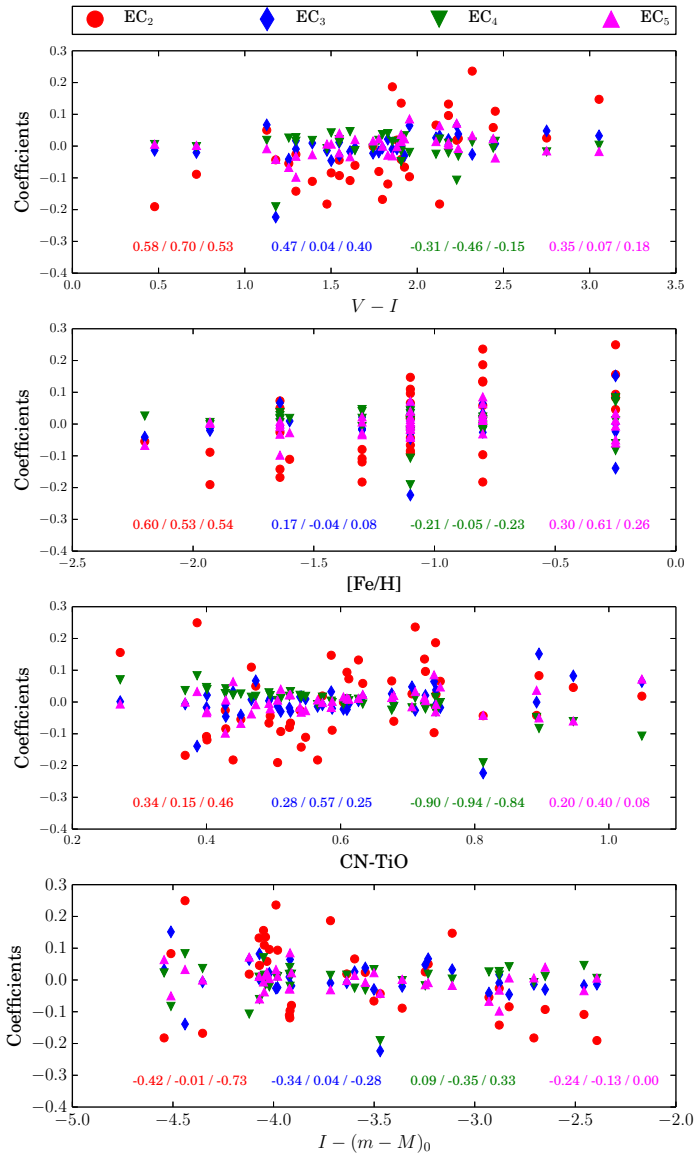

Figure 3.9: C-star eigencoefficients versus physical properties ($V-I$ color, [Fe/H] of the host satellite, CN−TiO color, and absolute I-band magnitude) of the star. Coefficients of the second eigenspectrum are plotted as red circles, coefficients of the third are plotted as blue diamonds, coefficients of the fourth are plotted as inverted green triangles, and coefficients of the fifth are plotted as magenta triangles. The Spearman's rank correlation coefficient for each eigenspectrum is printed in the corresponding color, in the format "all carbon stars / bright carbon stars only / faint carbon stars only."

spectra will be necessary to tease out finer features than CN.

The first eigenspectrum is the mean of the full carbon star sample. At a glance it is indistinguishable from many of the spectra in Figure 3.7, with prominent CN features. Visible here but not in each individual spectrum are some of the finer structure in the carbon features, such as the sawtooth shape of the CN band heads at $\sim$ 6900 and $\sim$ 7900Å. There is also a visible Ca II triplet, and what could be the C_2 feature at 7700Å. However, there is no discernible signature of C_2 at 8800Å.

The second eigenspectrum shows similar CN features to the first, as well as a general increase in flux at red wavelengths. Unlike the first eigenspectrum, it has no visible Ca II, and stronger C_2 at 7700 and 8800Å. This eigenspectrum governs, at least in part, the temperature and metallicity dependent aspects of the carbon star spectra. This suggests that the strength of CN varies with temperature and metallicity. The top two panels of Figure 3.9 show the relationship between the eigencoefficients of this eigenspectrum (EC_2) as a function of $V-I$ color and [Fe/H] of the host satellite. The Spearman correlation coefficients (displayed on each panel in Figure 3.9 for the full sample, the bright carbon stars alone, and the faint carbon stars alone, in that order) indicate positive correlations for both. This reflects the degeneracy seen in the models, where the combination of low metallicity and low temperature can result in a spectrum that looks remarkably similar at optical wavelengths to a star with high temperature and high metallicity (Aringer *et al.*, 2009; Aringer *et al.*, 2016). Interestingly, EC_2 also correlates with absolute I-band magnitude, but only for the faint (sub-TRGB) carbon stars.

The fourth eigenspectrum does not have the same CN features as the first two. Its most prominent feature is a break in flux at $\sim$ 7900Å, just blueward of the 7900Å CN bandhead.

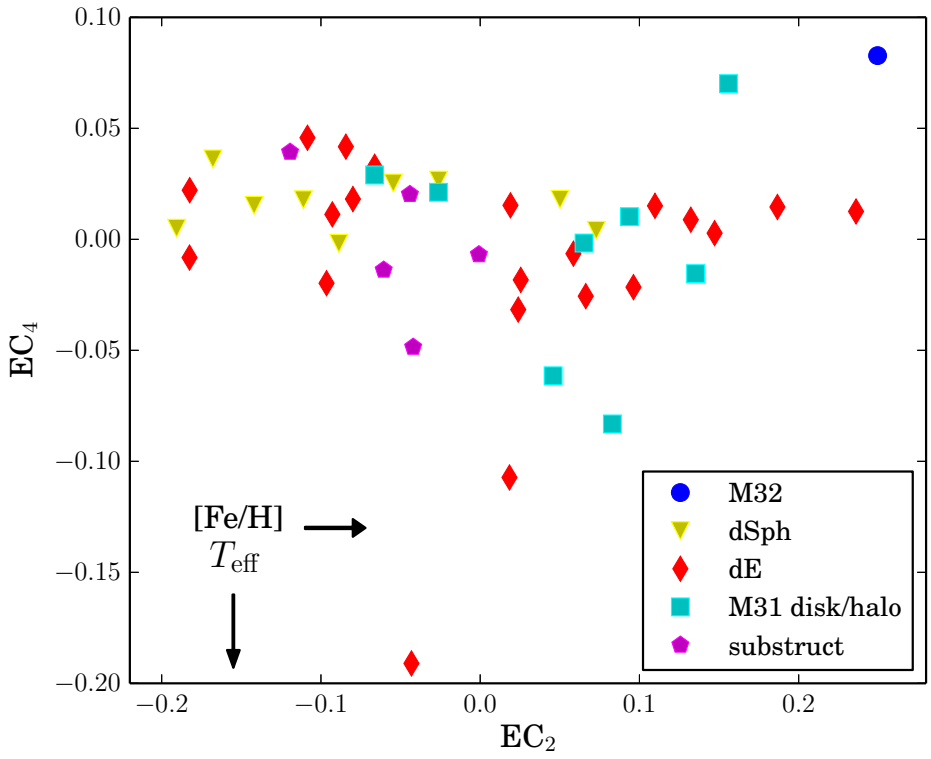

Figure 3.10: EC_2 (a tracer of metallicity) versus EC_4 (a tracer of $T_{\rm eff}$) for all carbon stars in the sample. Colors and shapes denote the type of field/object to which the star is a member, as designated in Table 3.2: stars in the dSphs are plotted as yellow triangles, stars in the dEs are plotted as red diamonds, stars in substructure fields are plotted as magenta pentagons, and the stars in M32 are plotted as blue circles. Finally, stars in the M31 disk or halo (which are kinematically difficult to separate) are plotted as cyan squares.

There is a similar break just blueward of the 6900Å CN bandhead. Figure 3.9 illustrates that it correlates strongly with CN−TiO color for the full carbon star sample as well as the two subsamples (with a Spearman correlation coefficient less than -0.8 for all three), but weakly with the other properties. Carbon star models indicate that at fixed metallicity CN−TiO color increases smoothly as $T_{\rm eff}$, whereas at fixed temperature the change in CN−TiO with metallicity is far less predictable (Aringer *et al.*, 2009). The coefficients of this eigenspectrum (EC_4) are

thus likely a more direct indicator of $T_{\rm eff}$ than EC_2, with EC_2 correlating inversely with $T_{\rm eff}$.

The third and fifth eigenspectra are more difficult to interpret. The only significant correlation seen in either comes out when looking only at the bright (super-TRGB) subset of carbon stars. The third eigenspectrum correlates with CN–TiO color, and the fifth eigenspectrum correlates with [Fe/H].

The eigencoefficients of the 2nd and 4th eigenspectra thus contain most of the information regarding the temperature and metallicity of the carbon stars. Figure 3.10 shows EC_4 versus EC_2 for all carbon stars in the sample, coded by their environment (dE, dSph, M32, halo, or substructure). Following our interpretation of these eigencoefficients, this plot can be thought of as $T_{\rm eff}$ versus [Fe/H]. This figure suggests several trends. First, the single carbon star belonging to M32 has the highest values of both EC_2 and EC_4, indicating that it is both metal-rich and particularly cool. This is consistent with the metallicity of M32 being higher than the other satellites. Next, the carbon stars in the substructure and most dSphs fields have lower values of EC_2 than the other fields, but comparable values of EC_4. This suggests that they are more metal poor than the other fields. The dEs span the full range of EC_2.

The range of EC_2 values is far larger than the range of EC_4 values. While the eigencoefficient ranges do not correspond directly to the range in $T_{\rm eff}$ or metallicity, this may indicate that the carbon stars have comparable temperatures regardless of their metallicity. This would be consistent with models indicating that the formation of AGB carbon stars is bound within a relatively narrow range of mass (Suda and Fujimoto, 2010; Karakas, 2014)

None of the first five eigenspectra correlate strongly with absolute *I* magnitude. There is thus no clear spectroscopic difference between the faint carbon stars in our sample and the

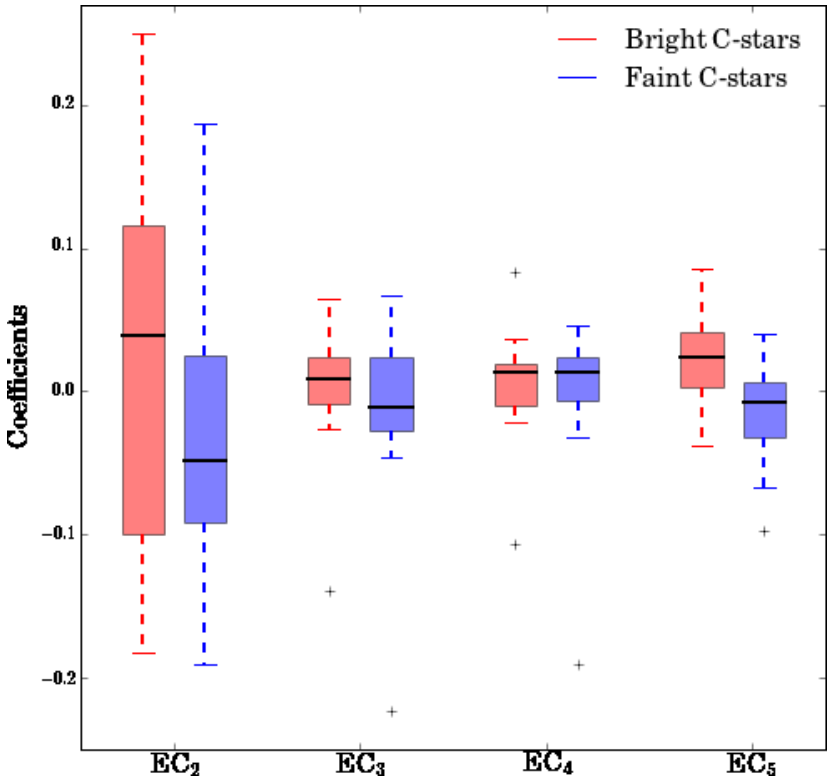

Figure 3.11: Eigencoefficients of bright (red) versus faint (blue) carbon stars. Black lines indicate the median of the distribution, red/blue boxes encompass the quartiles. Outliers are displayed as red/blue crosses.The distributions of eigencoeffients of the second and fifth eigencoefficients (EC_2 and EC_5) differ markedly, with the bright carbon stars typically having larger, more positive coefficients. The eigencoefficients of the third and fourth eigenspectra are nearly indistinguishable.

bright carbon stars. Figure 3.11 illustrates this more clearly, with boxplots representing the distribution of eigencoefficients for all bright and faint carbon stars. There is considerable overlap in the distributions of the faint and bright populations for each eigencoefficient. The two that show a significant difference are EC_2 and EC_5. The median EC_2 value for the bright carbon stars is higher than the majority of the faint carbon stars, which suggests that the bright carbon stars are more metal rich.

3.6 Discussion

In the previous sections we have presented the photometric and spectroscopic properties of the carbon stars found by the SPLASH survey in the satellites and halo of M31. This includes their distribution in various color-color spaces, their luminosities with respect to the I_{TRGB} of their respective regions, and the eigenspectra that make up the fundamental components of their spectra. Here, we will discuss the implications of these properties.

3.6.1 General properties of the SPLASH carbon stars

We identify 41 carbon stars in the satellites and halo of M31. Many are located in fields in which significant numbers of intermediate-age AGB stars have already been identified, including the dEs NGC 147, NGC 185 and NGC 205, and the dSph And II (e.g. Nowotny *et al.*, 2003; Kerschbaum *et al.*, 2004; Battinelli and Demers, 2004a,b). We also identify several carbon stars in the vicinity of M32, which is known to have a substantial intermediate-age population (Davidge, 2014; Jones *et al.*, 2015). However, the majority of our sample have

kinematics suggesting membership to M31 rather than M32 itself. We identify a small number of carbon stars in the dSphs And V, And IX and And X. However this combined sample of four stars, three of which are fainter than the TRGB, indicates no significant intermediate-age population in these galaxies. Finally, we see four carbon stars in regions known to contain substructure from the Giant Southern Stream.

Analysis of the carbon star photometry also reveals that a significant fraction of our sample is fainter than the TRGB. These may be extrinsic in origin, and we will explore their nature fully in the next section.

Our sample of carbon stars appears to be largely dust-free and hydrostatic. Their optical colors are fairly well fit by the dust-free hydrostatic models from Aringer *et al.* (2016), though the models do not extend blue enough to fully match the colors of the faint carbon stars. The introduction of MIR colors complicates this picture, as the dust-free models do not match the observations well in optical versus MIR color-color space. However, none of the carbon stars in our sample appear in the DUSTiNGS variable star/extreme-AGB star catalog, which further supports the idea that they are not heavily effected by dust and dynamics (though again, two epochs is insufficient to rule out variability completely). Finally, very few of our carbon stars exhibit Hα emission, which is associated with presence of shock waves induced by pulsation in the stellar atmosphere. Of the carbon stars in the solar neighborhood, 70% of the Miras, 66% of the SRa type, and 20% of SRb and Lb type stars show Hα in emission (Mauron *et al.*, 2014). The carbon stars in the satellites and halo of M31 are comparatively quite quiet, which would be consistent with a significant population being extrinsic.

Application of PCA to the carbon star spectra illustrates the effects of temperature

Table 3.5: Fraction of faint carbon stars in the Local Group

Field	N_C	N_{FC}/N_C	$I_{\rm limit}-I_{\rm TRGB}$	Reference
IC 1613	195	$0.087^{0.02}_{0.01}$	1.6	Albert *et al.* (2000)
Leo I	27	$0.148^{0.06}_{0.04}$	1	Demers and Battinelli (2002)
Aquarius	3	$0.000^{0.16}_{0.00}$	0.85	Battinelli and Demers (2000)
Pegasus	40	$0.150^{0.05}_{0.04}$	1.1	Battinelli and Demers (2000)
Sagittarius dIrr	33	$0.242^{0.06}_{0.05}$	1.6	Demers and Battinelli (2002)
LMC	7760	$0.017^{0.00}_{0.00}$	...	Kontizas *et al.* (2001)
NGC 6822	907	$0.163^{0.01}_{0.01}$	1.9	Letarte *et al.* (2002)
Phoenix	2	$0.500^{0.23}_{0.23}$	...	Martínez-Delgado *et al.* (1999)
Draco	6	$1.000^{0.00}_{0.09}$	...	Shetrone *et al.* (2001)
Ursa Minor	7	$1.000^{0.00}_{0.07}$	...	Shetrone *et al.* (2001)
And III	1	$1.000^{0.00}_{0.36}$	1.6	Harbeck *et al.* (2004)
And VI	2	$0.500^{0.23}_{0.23}$	1.6	Harbeck *et al.* (2004)
And VII	5	$0.400^{0.17}_{0.15}$	1.4	Harbeck *et al.* (2004)
Cetus	3	$0.667^{0.16}_{0.22}$	1.5	Harbeck *et al.* (2004)
And X	2	$1.000^{0.00}_{0.22}$	1.92	This work
M32	1	$0.000^{0.36}_{0.00}$	0.25	This work

and metallicity. We find that the depth of the broad CN bands (governed by the second eigenspectrum) correlates most strongly with metallicity, while the depth and shape of the break in the spectrum at ~ 7900Å traces T_{eff} (governed by the fourth eigenspectrum). Comparing the coefficients of the eigenspectra governing these features illustrates that the carbon stars in M32 and the M31 disk/halo are typically more metal-rich than the carbon stars in the substructure and dSphs.

Table 3.5 (cont'd): Fraction of faint carbon stars in the Local Group

Field	N_C	N_{FC}/N_C	$I_{\rm limit} - I_{\rm TRGB}$	Reference
And IX	1	$1.000^{0.00}_{0.36}$	2.2	This work
NGC 205	6	$0.167^{0.14}_{0.08}$	0.3	This work
And V	1	$0.000^{0.36}_{0.00}$	1.71	This work
NGC147	158	$0.301^{0.03}_{0.03}$	2.6	This work + Nowotny *et al.* (2003)
NGC185	157	$0.325^{0.03}_{0.03}$	3.0	This work + Nowotny *et al.* (2003)
And II	10	$0.300^{0.12}_{0.10}$	2.5	This work + Kerschbaum *et al.* (2004)

3.6.2 Characterizing the faint carbon stars

In many of our satellites we see a significant number of carbon stars fainter than the TRGB. There are three possible explanations. The first is that these are extrinsic carbon stars, whose carbon was obtained by mass transfer from a carbon-rich AGB star onto a binary companion rather than through dredge-up of He-burning products during the TP-AGB phase (de Kool and Green, 1995; Frantsman, 1997; Izzard and Tout, 2004). The second possible explanation is that they are genuine TP-AGB stars experiencing the post-flash luminosity dip (Boothroyd and Sackmann, 1988) or in a minimum of their dynamic phase (Nowotny *et al.*, 2011). Finally, they may be bright AGB stars extincted by circumstellar dust. Both sections 3.4 and 3.5 treat the bright (super-TRGB) and faint (sub-TRGB) carbon stars as separate populations, to help determine which of the above explanations is most likely.

From the photometry, we can rule out dust as a likely explanation for the faint carbon stars. If the faint carbon stars are heavily extincted then they should appear redder than the brighter population in $V-I$. However, as noted in the previous section, our sample appears to be well fit by the dust-free hydrostatic models. In addition, both the one and two dimensional

color distributions (Figures 3.5 and 3.6, respectively) indicate that the faint carbon stars are typically bluer in $V-I$ than the bright carbon stars.

If the faint carbon stars are extrinsic, we would expect them to be present down to the SPLASH detection limit, while carbon stars on the TP-AGB would be clustered around the TRGB. The observed distribution of I-band magnitudes suggests the former: Figure 3.4 illustrates that the faint carbon stars are present down to 1.5 magnitudes below the TRGB (though this varies from field to field given inhomogeneous detection limits).

We would also expect extrinsic carbon stars to be warmer than their intrinsic counterparts. Both Figures 3.5 and 3.6 illustrate that many of the faint carbon stars are indeed bluer in $(V-I)$ than the bright carbon stars, despite comparable CN–TiO color. They are also typically bluer than the dust-free hydrostatic AGB models from Aringer *et al.* (2016). The effects of dust and dynamics are not likely to make C-stars so optically blue ($V-I<1.5$), so this suggests that these stars do not in fact belong to the AGB.

Spectroscopically, many of the known differences between intrinsic and extrinsic carbon stars fall beyond our wavelength coverage (e.g., G band of CH at ~ 4300Å, $^{12}C/^{13}C$ ratio). The major difference between the bright and faint carbon stars in our sample is the eigencoefficients of the second eigenspectrum (EC_2) (see Figure 3.11). The faint carbon stars typically have negative EC_2 values, while the bright carbon stars have positive EC_2 values. Observationally, this translates to the faint carbon stars having weaker CN bands and appearing more metal-poor than the bright carbon stars. This is fully consistent with observations of extrinsic carbon stars in the Local Group, which are often characterized by their lack of metals (e.g. the CEMP stars). Within the subset of faint carbon stars, we find that EC_2 anticorrelates with

absolute I-band magnitude. Observationally, this means that the brightest/most massive of the faint carbon stars have the strongest CN. Finally, the eigencoefficients of the fifth eigenspectrum (EC_5) also differ between the bright and faint samples, perhaps due to more noise in the fainter stars.

However, all of the figures discussed in this section also illustrate that the colors and magnitudes of the faint carbon stars cover a significant range. Some are fully consistent with the bright carbon stars. It is probable that the faint population consists of a mix of intrinsic and extrinsic carbon stars. Models based on the Magellanic Clouds suggest that $< 10\%$ of TP-AGB stars are fainter than the TRGB (e.g., Marigo and Girardi, 2007; Melbourne and Boyer, 2013) at any given time. This places an upper limit on the number of intrinsic interlopers in the faint population at 1.8 stars.

3.6.3 Carbon star luminosity by environment

At first glance, we appear to observe more faint carbon stars in our less luminous galaxies. To parametrize this, we calculate N_{FC}/N_C, the fraction of faint (sub-TRGB) carbon stars in the full sample of carbon stars, for each galaxy. To place these findings within a broader context, we also calculate N_{FC}/N_C in other Local Group satellites. To compare similar groups of stars, we limit ourselves to optical carbon star surveys, leaving aside surveys in the NIR and MIR and serendipitous carbon (or CH) star discoveries. We assemble C-star counts in IC 1613 (Albert *et al.*, 2000), Leo I, Sagittarius dIrr (Demers and Battinelli, 2002), DDO 210/Aquarius, Pegasus (Battinelli and Demers, 2000), NGC 6822 (Letarte *et al.*, 2002), Phoenix (Martínez-Delgado *et al.*, 1999), Draco, Ursa Minor (Shetrone *et al.*, 2001), the LMC (Kontizas *et al.*,

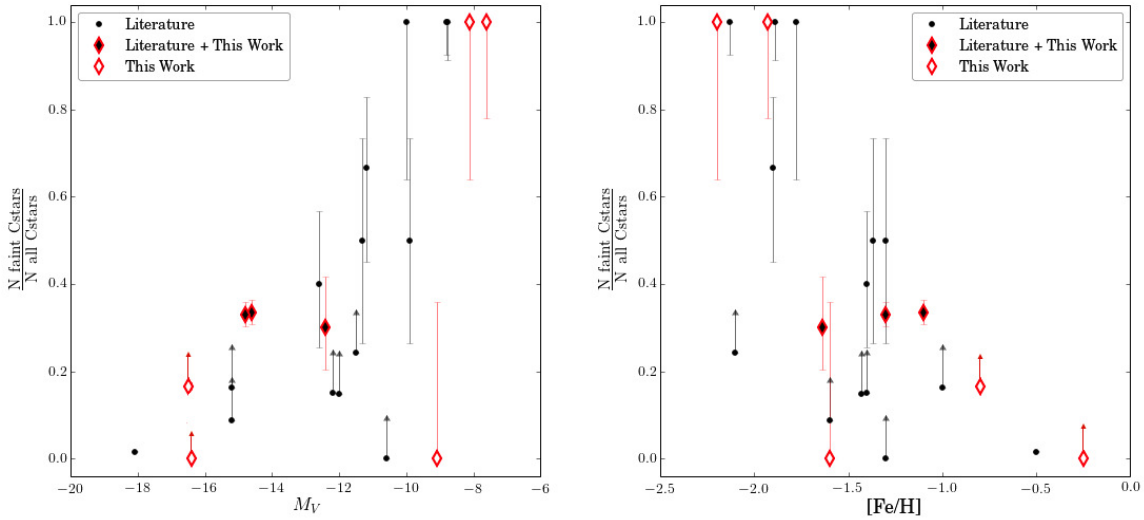

Figure 3.12: Fraction of faint carbon stars as a function of [Fe/H] of the host satellite. Samples from the literature are plotted as black points, samples from the present work are plotted as red diamonds, and samples that combine new and existing data are plotted as red diamonds filled with black. Also shown are the 1σ binomial proportion confidence intervals. Though the uncertainties are large, the fraction of the full carbon star sample fainter than the TRGB appears to increase in smaller, metal-poor galaxies.

2001), And III, And VI, And VII and Cetus (Harbeck *et al.*, 2004). These data are provided in Table 3.5.

The majority of these fields (IC 1613, Pegasus, Aquarius, NGC 6822, Leo I, Sag dIrr) rely on optical FBPS to identify carbon stars. All survey the full galaxy area and extend to 1-2 magnitudes fainter than the TRGB. The approximate extent below the TRGB is listed in Table 3.5. This is roughly equivalent to the SPLASH coverage and detection limit, so we will not worry tremendously about differences in depth for these fields. However, all require C-stars to have $R-I > 0.9$ (though Letarte *et al.* 2002 also look at "bluer" C-stars with $0.8 < R-I < 1.1$). This makes them biased against the faint carbon stars, which we find to be bluer. As a result, the N_{FC}/N_C that we calculate in these fields are likely lower limits. In each field we compute $I_{\rm TRGB}$ following the same prescription outlined in Section 3.3.2 and count the number of C-stars fainter than that limit.

We consider the carbon star samples in Phoenix, Draco, Ursa Minor, the LMC, And III, And VI, And VII and Cetus to be representative of the full carbon star population. The two carbon stars in Phoenix were confirmed spectroscopically by Da Costa (1994), though our data come from Martínez-Delgado *et al.* (1999). Subsequent work by Menzies *et al.* (2007) did not identify any other carbon stars visible in the optical, so we consider this sample of two to be complete. The carbon star census presented in Shetrone *et al.* (2001) for Draco and Ursa Minor relies on the identification of carbon stars via photographic plates (Aaronson *et al.*, 1982; Azzopardi *et al.*, 1986). These stars have been thoroughly vetted (e.g., Dominguez *et al.*, 2004; Abia *et al.*, 2008), and no new carbon stars have been identified. The Kontizas et al. survey of the LMC was conducted with objective-prism plates and visual identification of carbon-stars

using the Swan C_2 bands at 4737Å and 5165Å. Because this is a spectroscopic rather than photometric identification, there is not a strong bias against faint C-stars. This survey is likely incomplete in the most crowded central regions, but we do not expect the extrinsic and intrinsic carbon stars to have different spatial distributions and this incompleteness is not likely to skew our counts. Thus, the N_{FC}/N_C fraction we calculate in the LMC is likely representative. These four fields rely on spectroscopic identification of carbon stars, so their photometric limits are excluded from Table 3.5. Finally, Harbeck *et al.* (2004) use FBPS to identify carbon stars in And III, And VI, And VII and Cetus, but do not apply a limit in $V-I$. They thus sample the bright and faint carbon stars uniformly.

Because Shetrone *et al.* (2001) provide V-band magnitudes of the carbon stars in Draco and Ursa Minor, we compute $V_{\rm TRGB}$ using relationships from Bellazzini *et al.* (2004) and Mager *et al.* (2008). For Phoenix and the LMC, for which provide I-band magnitudes have been provided, we once again calculate the TRGB magnitude using the method described in Section 3.3.2. Harbeck *et al.* (2004) have provided designations of C versus dC (which translate to super- and sub-TRGB), which we use to calculate N_{FC}/N_C in their four fields.

In addition to the new fields discussed above, we also compile carbon star populations in And II, NGC 147 and NGC 185 from the literature. We combine our carbon star samples observed by SPLASH with these samples from the literature. The observations of And II (Kerschbaum *et al.*, 2004), NGC 147 and NGC 185 (Nowotny *et al.*, 2003) also use FBPS, but with V and i_0 as the broad-band colors rather than R and I. Both authors' observations extend ~ 0.5 magnitudes below the TRGB, and they require C-stars to have $(V-i)_0 > 1.16$ and (TiO–CN)$_0 < -0.3$. This limit in $(V-i)_0$ is equivalent to $(R-I) > 0.53$, which encompasses the full

color range over which we observe carbon stars. As a result, we consider this a representative sample. As Bellazzini *et al.* (2004) do not provide a TRGB calibration for i_0, we use the values calculated by Kerschbaum *et al.* (2004), $i_{\rm TRGB} = 20.5$, and Nowotny *et al.* (2003), $i_{\rm TRGB} = 19.96$ for NGC 185 and $i_{\rm TRGB} = 20.36$ for NGC 147, when computing $\rm N_{FC}/N_C$.

Finally, two of the SPLASH fields (M32 and NGC 205) were surveyed so shallowly that they too should be considered lower limits on $\rm N_{FC}/N_C$. We calculate this limit in SPLASH fields using the full SPLASH sample (independent of membership or strength of carbon features).

Figure 3.12 plots N_{FC}/N_C in the galaxies listed in Table 3.5 as a function the absolute magnitude and metallicity of the host satellite (obtained from McConnachie, 2012). Also plotted are the 1σ binomial proportion confidence intervals, save in the cases discussed above where the calculated fraction represents a lower limit. With the exception of the LMC, NGC 147 and NGC 185, the small sample sizes translate to large uncertainties. A trend is still evident; the fraction of faint carbon stars decreases as the galaxy gets brighter and its metallicity increases. The serendipitous detections of CH and dC stars in MW globular clusters adheres to this trend, increasing the number of faint, low-metallicity systems in which $N_{FC}/N_C = 1$.

There are two possible explanations for this trend. The first presumes that the faint carbon stars are extrinsic and owe their composition to a binary companion. If the fraction of stars in binary systems increases in smaller satellites (as it has been shown to increase in smaller globular clusters, Milone *et al.*, 2012), then so will the fraction of faint carbon stars. However this explanation would also require a sizeable population of AGB stars in earlier generations to provide the binary companions. The second explanation presumes that the entire carbon star

sample is made up of intrinsic TP-AGB stars. In this case, the trend could be explained by the effect of metallicity on carbon star formation. At low metallicity, dredge-up efficiency is higher, the range of masses over which carbon stars can form is larger, and TDU begins earlier (Karakas *et al.*, 2002; Marigo *et al.*, 2013; Karakas, 2014). It is possible that at low metallicities these effects combine to produce carbon stars that are fainter than the TRGB. Indeed both explanations may be occur simultaneously. The more massive companion in an earlier binary pair is likely to go through the AGB. In metal-poor galaxies, that AGB star is more likely to be carbon-rich and the low-mass companion is more likely to become carbon enhanced.

3.7 Conclusions

We identify 41 unambiguous carbon stars in the satellites and halo of M31. We present optical, synthetic narrow-band, and MIR photometry of these stars, as well as moderate-resolution optical spectra. Photometric and spectroscopic analysis suggests that they are relatively unaffected by dust and dynamics.

Many of the carbon stars we identify are fainter than the TRGB. In addition to being fainter, these stars are also often bluer and more metal-poor than their super-TRGB counterparts. They are likely to be extrinsic carbon stars. However, this designation is far from unambiguous. Observations at different wavelengths (bluer to capture features known to distinguish intrinsic and extrinsic chemistry, redder to capture any effects of dust), and the extension of carbon-star models to low metallicity ([Fe/H] < -1.5) will be necessary to classify these stars definitively.

Chapter 4

M-giants in the Satellites and Halo of M31

4.1 Introduction

M-giants are late-type stars whose atmospheres are cool enough to support oxygen molecules. On the red giant branch (RGB), M-giants nominally begin with a H-burning shell around a degenerate He-core before eventually commencing He-burning. On the asymptotic giant branch (AGB), they have both He- and H-burning shells around an inert C+O core. Despite these physical differences, M-giants on both branches are observationally very similar. They are luminous, red, and have unmistakable bands of TiO and other oxygen features. This unique spectral signature combined with their high luminosity means that M-giants can be easily identified at large distances, making them useful tracers of kinematical structure (e.g., Majewski *et al.*, 2003; Sharma *et al.*, 2010).

The M-giants on the AGB are particularly interesting due to their relationship with their carbon rich counterparts (carbon stars). AGB stars all begin as oxygen-rich M-giants, with

the ratio of free carbon to free oxygen (C/O) in their atmospheres less than unity. However, the third dredge-up (3DU) that occurs during the thermally pulsating AGB (TP-AGB) phase brings carbon from the stellar interior to the surface. Given sufficiently efficient dredge-up, the free oxygen that characterizes M-giants can be overwhelmed with carbon, leading to a carbon star with C/O greater than unity. The number ratio (C/M) of carbon- to oxygen-rich AGB stars traces the environmental metallicity gradient (e.g., Cioni *et al.*, 2008; Feast *et al.*, 2010; Hamren *et al.*, 2015), and has been used to constrain theories and models of AGB evolution (Boyer *et al.*, 2013; Karakas, 2014). In addition, there are significant differences between dust formation and mass loss in M-giants versus carbon stars that are still not entirely understood (e.g., Boyer *et al.*, 2009; Srinivasan *et al.*, 2009; Boyer *et al.*, 2011; Riebel *et al.*, 2012).

Selecting the M-giants on the AGB can present some observational challenges. First is the ubiquity of M-dwarfs, which can contaminate photometric M-giant surveys (and visa versa). Fortunately, many surface gravity sensitive metrics have been developed to assist with this problem (Bessell and Brett, 1988; Reid *et al.*, 1995; Gilbert *et al.*, 2006; Mann *et al.*, 2012) and spectroscopic surveys can separate dwarfs and giants fairly easily (e.g., Zhong *et al.*, 2015). The second challenge is the fact that M-giants on the AGB have little to distinguish them from M-giants on the RGB (Sneden *et al.*, 2000) or red supergiants (Blum *et al.*, 1996). The clearest delineator is absolute magnitude. Separating the less common M-type AGB stars from the RGB can thus be done using the magnitude of the tip of the red giant branch (TRGB) (Albert *et al.*, 2000; Nowotny *et al.*, 2001, and subsequent papers in these series), while the distinction between AGB stars and red supergiants requires a distance estimate.

In this chapter we will identify and characterize a sample of M-type AGB stars in the

satellites and halo of M31, with this work providing a companion to our work on carbon stars in Chapter 3. To do this we leverage data from the Spectroscopic and Photometric Landscape of Andromeda's Stellar Halo survey (SPLASH; Guhathakurta *et al.*, 2005, 2006). We combine the wealth of photometric and spectroscopic observations from SPLASH with recent advances characterizing the halo and satellites, including satellite distances, systemic velocities and velocity dispersions (e.g., Kalirai *et al.*, 2010; Tollerud *et al.*, 2012; Ho *et al.*, 2012; Collins *et al.*, 2013; Ho *et al.*, 2015); identification of regions of halo substructure (Gilbert *et al.*, 2006; Kalirai *et al.*, 2006a; Gilbert *et al.*, 2007, 2009a); and characterization of the halo's global properties (Tanaka *et al.*, 2010; Gilbert *et al.*, 2012; Gilbert *et al.*, 2014).

This chapter is organized as follows. Section 4.2 summarizes our dataset. In Section 4.3 we describe our identification of M-giants, including the random forest we construct to identify M-giants from their spectra and the distinction between AGB and RGB stars based on luminosity. Section 4.4 discusses the spatial distribution of the final M-giant sample, and in Section 4.5 we evaluate their physical properties ($T_{\rm eff}$ - § 4.5.1, dust and dynamics - § 4.5.2, metallicity - § 4.5.3, and the differences between M-giants on the AGB and the RGB - § 4.5.4). Throughout this chapter we will compare the M-giants on the AGB to both carbon stars from Chapter 3 and M-giants on the RGB.

4.2 Data

4.2.1 Spectroscopic and Photometric Observations

The SPLASH observations on which this work is based are described in detail in Chapter 3, and references therein. Briefly, the observations cover ~ 60 separate fields in the M31 system, targeting M32 (Howley *et al.*, 2013), 16 dSphs (Ho *et al.*, 2012; Tollerud *et al.*, 2012), all three dEs (NGC 147, NGC 185 and NGC 205; Geha *et al.*, 2006, 2010) the smooth virialized halo, and known halo substructure (Gilbert *et al.*, 2006, 2009a, 2012).

Each field has optical photometry in V and I; M, T_2 and DDO51; or R and I, taken from a variety of ground-based telescopes. M32 is the exception, with only i' photometry. This photometry was used to select spectroscopic targets to observe with the DEIMOS multi-object spectrograph (Faber *et al.*, 2003) on the Keck II 10m telescope. In most cases, the spectra were observed with the 1200 line mm^{-1} configuration centered at 7800Å. This enables wavelength coverage from Hα to the near-infrared Ca II triplet (CaT) with a dispersion of 0.33Å pixel^{-1}. With a typical integrration time of 3600s per mask, the average S/N is ~ 5 pixel^{-1}.

The full SPLASH sample (not including the disk fields featured in Chapter 2) contains 14143 stellar spectra. Each spectrum has a measured radial velocity and a quality assessment of that radial velocity measurement ($z_{\rm qual}$). In addition to the photometric observations in the filters listed above, we also perform a series of photometric transformations so that each spectrum (save those in M32) has V, R, and I-band photometry. The full details of these transformations are given in Chapter 3. Finally, we calculate synthetic CN–TiO, where CN and TiO refer in this context to narrow-band filters centered on their namesake absorption features at 8120.5Å and

7778.4Å, respectively. We compute the synthetic magnitudes by weighting each spectrum with CFHT/CH12k throughput curves (see Chapter 2).

In this chapter we restrict the sample of SPLASH stars that we study to those with S/N$>$ 2 pixel^{-1}, and with a $z_{\rm qual}$ value associated with a confident radial velocity measurement.

4.2.2 Membership

This work depends heavily on our ability to distinguish M31 M-giants from MW M-dwarfs. To do this, we draw upon previous work by SPLASH team members (see Chapter 3 for a thorough description).

Membership in the satellites and halo fields has been determined through a combination of photometric and spectroscopic measurements. In various fields, the following stellar properties have been used: radial velocity, 8190Å Na I equivalent width, position in the gravity-sensitive M−DDO51 versus $M-T_2$ color-color space, position in I versus $V-I$ color-color space, photometric and spectroscopic [Fe/H] estimates, and position with respect to the center of the (possible) host satellite (Gilbert *et al.*, 2006; Geha *et al.*, 2006, 2010; Tollerud *et al.*, 2012; Ho *et al.*, 2012; Howley *et al.*, 2013). In the fields targeting the smooth halo, substructure, and most satellites, these properties have been combined to create likelihood classes (Gilbert *et al.*, 2006), which range from -3 (secure MW classification) to 3 (secure M31 classification).

For the purposes of this analysis, we require that stars have a likelihood greater than or equal to zero (which corresponds to the probability of belonging to M31 being greater than the probability of belonging to the MW). In fields where likelihoods are unavailable, we use the membership criteria set forth by the authors of the paper that originally presented the data. Our

one addition is to require that stars have $EW_{NaI} <= 3$Å. This criterium well separates M31 RGB stars from MW dwarfs at redder colors ($V-I > 2$), though it is less effective at distinguishing hotter dwarfs (Gilbert *et al.*, 2006). Due to the level of foreground contamination, the precise limit we set for EW_{NaI} can have a large effect. For example, increasing the EW_{NaI} limit in NGC 205 from 3Å to 4Å adds > 100 stars.

Applying these membership criteria reduces the number of stars in the SPLASH sample to 3272.

4.3 The M-giant sample

M-type stars of all luminosity classes are characterized by cool atmospheres ($T_{\rm eff} <$ 4000K) dominated by broad oxygen features. At optical and NIR wavelengths ($< 1\mu$m), TiO is the most prominent source of absorption, followed by VO, ZrO and YO. At longer wavelengths, H_2O, SiO, OH and CO take over.

At the wavelengths covered by SPLASH (Hα through the Ca II triplet), TiO dominates the spectrum. For late-type M-stars in the SPLASH sample, the TiO bandheads at $\sim$ 7000Å and $\sim$ 7500Å are unmistakable, even at very low S/N. However for early-type M-stars in the SPLASH sample, low S/N obscures these features and makes the stars difficult to distinguish from warmer K-types. In this section, we use a combination of TiO-based features to spectroscopically identify M-stars across the full range of S/N and break them up into AGB and RGB subsamples.

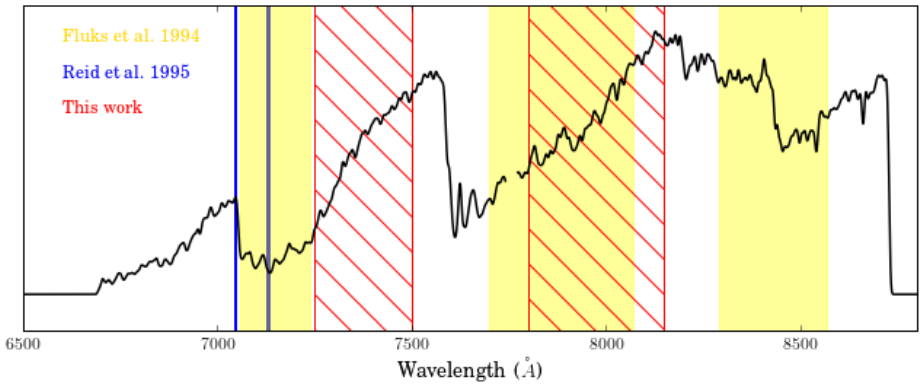

Figure 4.1: Sample SPLASH M-giant with the regions parametrized by our computed features marked. Blue regions refer to the TiO5 index from Reid *et al.* (1995), yellow regions govern the S-indices from F94, and red hatched regions are where we compute slopes m_1 and m_2.

4.3.1 Automated M-star classification

To spectroscopically identify M-stars in the SPLASH sample, we use a random forest (Breiman, 2001). A random forest is well suited to this binary (M versus not-M) classification problem in which features may not be linearly separable. In this section, we describe our training set, the features that we use, the performance of our classifier, and the final sample.

To explain the random forest (sometimes called a random forest of trees) algorithm, we will begin by describing decision trees. A single decision tree is a flowchart-like algorithm based upon a series of nodes through which an observation travels based on criteria with binary outcomes (e.g.,"Is CN–TiO > 0?"). At each node, we choose the split criterium to maximize the decrease in impurity from the parent node to its children (i.e. the information gain). Impurity (also known as entropy) is measured as

$$\text{Entropy} = -\sum_{i} p_i \log p_i \tag{4.1}$$

where p_i is the probability of class i. In the context of M-giant identification, the classes are “M" and “not-M." It thus follows that p_i is the fraction of M or not-M stars in the sample contained within a node.

A random forest is a collection of decision trees. It is less likely to overfit than a single tree, though its interpretation is less straight forward. Each component tree is built from a subset of the training set, created by randomly sampling the full training set with replacement. At each node, a split is selected using a random sample n of the full set of N features, where we have chosen $n = \sqrt{(N)}$. Once the forest is built, it classifies new observations by averaging the probabilistic predictions of each individual tree. We build our random forest using the Python implementation available through `Scikit-learn` (Pedregosa *et al.*, 2011).

We use 44 M-stars and 157 non-M-stars from the X-Shooter Library (XSL, Chen *et al.*, 2014) as the base of our training set. To match the underlying stellar population in the SPLASH sample, we include XSL stars with spectral types from O through M, and disregard those in the “Other" category (namely L-stars and those without classification). We also remove the three M-dwarfs, as the SPLASH sample has already been cleaned of M-dwarfs. To mimic the resolution and S/N of the SPLASH sample (which are considerably lower than the spectra in the XSL), we rebin each XSL spectrum onto the SPLASH wavelength grid and randomly add Gaussian noise to each XSL spectrum to degrade its quality. Each XSL M-star spectrum was degraded 40 times, giving a final sample of 1399 stars with $1 < \mathrm{S/N\ pixel^{-1}} < 20$. The XSL non-M-star spectra were each degraded only 15 times, to achieve a more balanced distribution of M- versus non-M-type. To this set we add 69 known M-stars from the SPLASH sample. We restrict the training set to those spectra with S/N> 2, giving us a final training set of 1415

M-type spectra and 2176 non-M-type spectra.

For each training spectrum we compute ten features designed to parametrize major TiO bands. The regions covered by these indices are shown in Figure 4.1. Six are based on the work by Fluks *et al.* (1994, hereafter F94), who define three indices ($S_{1/2}, S_{1/3}$ and $S_{2/3}$, which we will collectively term S-indices) as follows:

$$S_{1/2} = \frac{\int_{7060}^{7240} F(\lambda) d\lambda}{\int_{7700}^{8070} F(\lambda) d\lambda} \tag{4.2}$$

$$S_{1/3} = \frac{\int_{7060}^{7240} F(\lambda) d\lambda}{\int_{8290}^{8570} F(\lambda) d\lambda} \tag{4.3}$$

$$S_{2/3} = \frac{\int_{7700}^{8070} F(\lambda) d\lambda}{\int_{8290}^{8570} F(\lambda) d\lambda} \tag{4.4}$$

These regions are shown in yellow in Figure 4.1. The three S-indices form a locus in three-dimensional space parametrized by spectral type (illustrated in Figure 4.2). We compute the three indices, their sum (ΣS), the M-type ($m_{\rm min}$) that minimizes the distance between the SPLASH star in S-index space and the locus defined by F94, and the magnitude of that distance. While these features are correlated, we find that including them all improves the performance of the resulting classifier. We also compute the TiO5 index defined by Reid *et al.* (1995), shown in blue in Figure 4.1, synthetic CN–TiO color, and S/N.

Finally, we measure the slopes of the spectrum in the regions $7250 < \lambda < 7500$Å (m_1), and $7800 < \lambda < 8150$Å (m_2) using a least squares fit of a 1st order polynomial over the wavelength range. These regions are shown in red in Figure 4.1. We add these two slopes to the

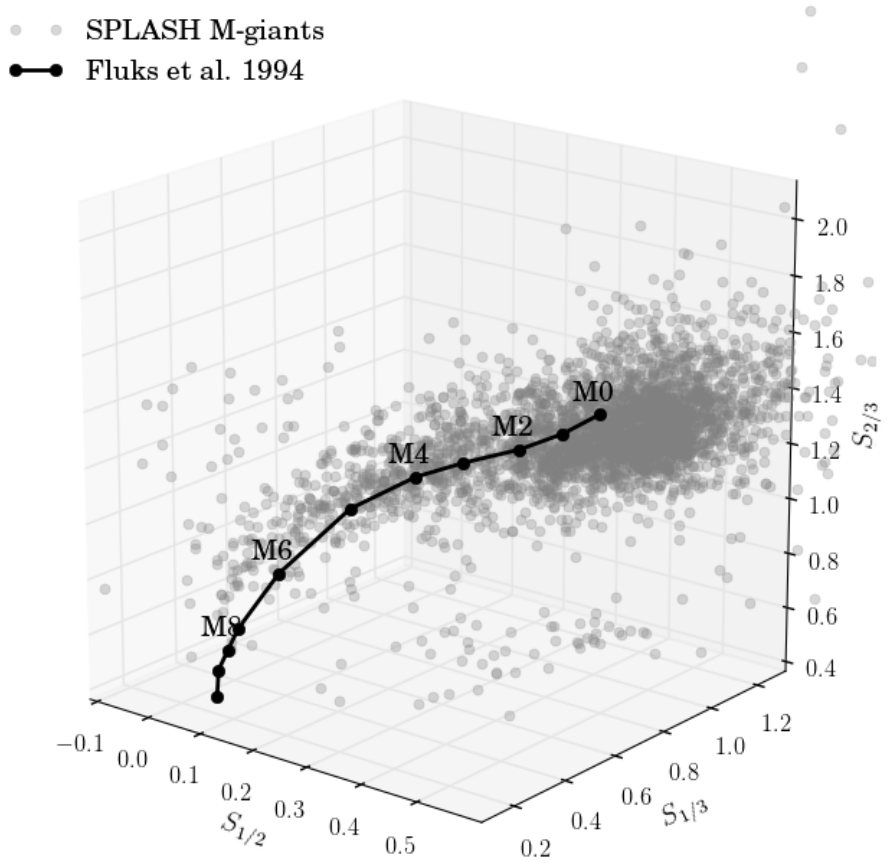

Figure 4.2: The 3272 M31 member stars from SPLASH plotted in grey in S-index space. Axes are $S_{1/2}$, $S_{1/3}$ and $S_{2/3}$ (F94). Plotted in black are the canonical S-indices F94 compute for the 10 M spectral subtypes, connected to show the locus that they form. We refer to this locus as being parametrized by M-type, as each M-type (and fractions thereof) corresponds to a unique point in S-index space.

features from the literature because several SPLASH spectra have wavelength coverage that stops short of the regions necessary for S-indices or TiO5.

To illustrate the classification power of some of these features, Figure 4.3 illustrates the distribution of several properties for the M-type spectra (blue) versus non-M-type spectra (green) in our training set. The top three panels illustrate the distribution of the three S-indices from F94, with the limit the authors find to correspond to M0 marked as a dashed black line. We annotate these panels with the fraction of M-type spectra and non-M-type spectra found in the M0+ region. The bottom left panel shows distance from the F94 locus as a function of S/N, and the bottom right panel shows the distributions of CN–TiO. In each panel, we see that while the M-type spectra are concentrated, there is still a significant amount of overlap between the M-type distributions and non-M-type distributions.

We set aside 30% of our training set to use for testing, and train the random forest (consisting of 10 trees) on the remaining 70%. When optimizing the algorithm parameters (number of trees, split evaluation, etc.) we prioritized a clean sample over a complete sample, and as a result our false positive rates are always lower than the false negative rates. The resulting classifier has a training accuracy of 99.8%, a false positive rate of 0% (i.e., training precision of 100%) and a false negative rate of 0.5% (i.e., training recall of 99.5%). When tested on the withheld data, it has a testing accuracy of 96.8%, a false positive rate of 2.2% (i.e., testing precision of 97.8%) and a false negative rate of 6.7% (i.e., testing recall of 93.3%). The features most important to the classifier, in order of decreasing importance, are TiO5, CN–TiO, minimum distance between the star in S-index space and the F94 locus, $S_{1/3}$, m_2, $S_{1/2}$, $S_{2/3}$, m_1, S/N, and $m_{\rm min}$.

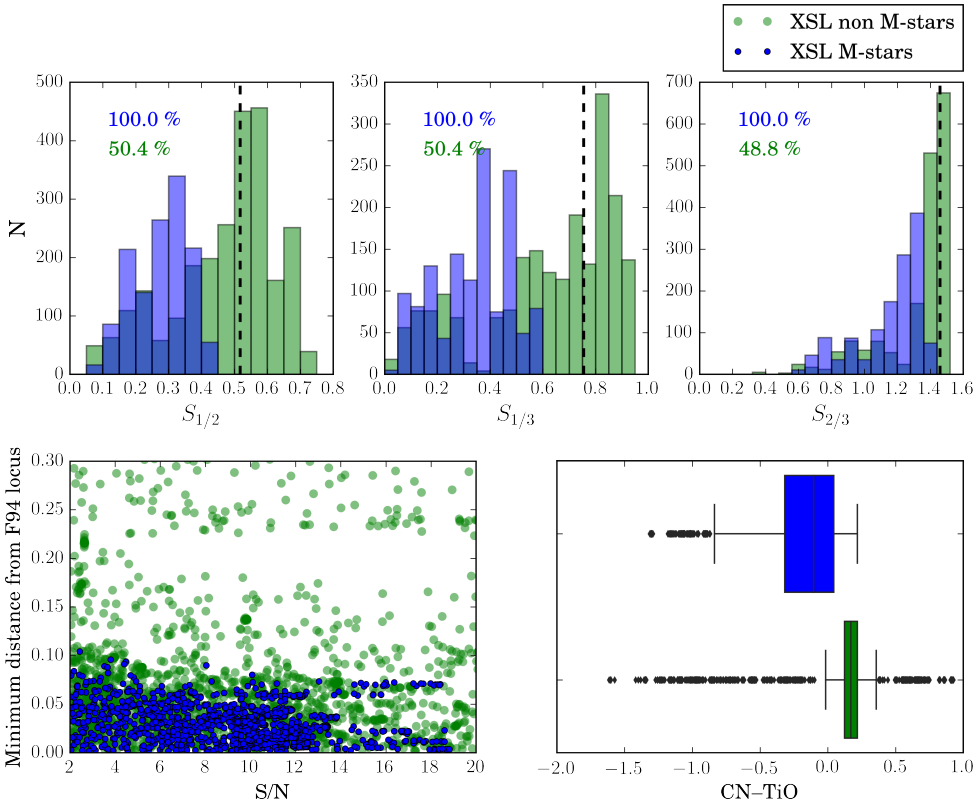

Figure 4.3: Sample features for M and non-M-type stars in the training set. M-type stars are shown in blue, and all others are shown in green. The top row of panels shows distributions of S-indices, with the limit corresponding to values typical of an M0 star (F94) marked as a dashed black line. Each of these three panels is annotated with the fraction of M and non M stars that fall within the M0+ region. The bottom left plot shows distance from the F94 locus as a function of S/N of the training spectrum. The bottom right panel shows distributions of synthetic CN–TiO. In all panels there is a considerable amount of overlap between the fairly concentrated M-star values and the non-M-star values.

A small fraction of the 3272 SPLASH spectra contains artifacts that impede classification. First, 45 stars have wavelength coverage beginning at $\sim$ 7300Å, preventing us from directly calculating the F94-based features. To impute these missing values we interpolate on the relationships between $m_1 + m_2$ and $S_{1/2}$ and $S_{1/3}$ (which have Spearman correlation values of -0.89 and -0.9, respectively). With estimated values for $S_{1/2}$ and $S_{1/3}$ we can calculate the other four F94-based indices. Next, some spectra do not have sufficient wavelength coverage to calculate TiO5. TiO5 correlates strongly with m_1 ($\rho = -0.85$), so we impute these missing values by interpolating on the relationship between TiO5 and m_1. Finally, some spectra suffer from bad sky-subtraction that causes a mismatch in flux levels between the blue and red DEIMOS chips. Unfortunately, this gap mimics the 7500Å TiO bandhead, and so can result in a false positive classification. We visually inspect the spectra whose flux increases by more than 150% across the chip gap, and remove those without true TiO features. This eliminates 39 stars from the sample, leaving us with 3237 members.

Applying the random forest to the cleaned sample of SPLASH members returns 533 M-giants. Figure 4.4 shows a small fraction of this sample (specifically, every eleventh spectrum), ordered by increasing $m_{\rm min}$. Many have regions of missing data, which we have filled in using eigenspectra obtained through iterative PCA (to be discussed in § 4.5.4). These regions are shown in grey, while the raw data are shown in black. The TiO bandheads are clearly visible, and increase in strength as $m_{\rm min}$ increases from the minimum (lower left) to the maximum (upper right). Almost all stars exhibit the Ca II triplet, while almost none show prominent VO bands (which appear around M7).

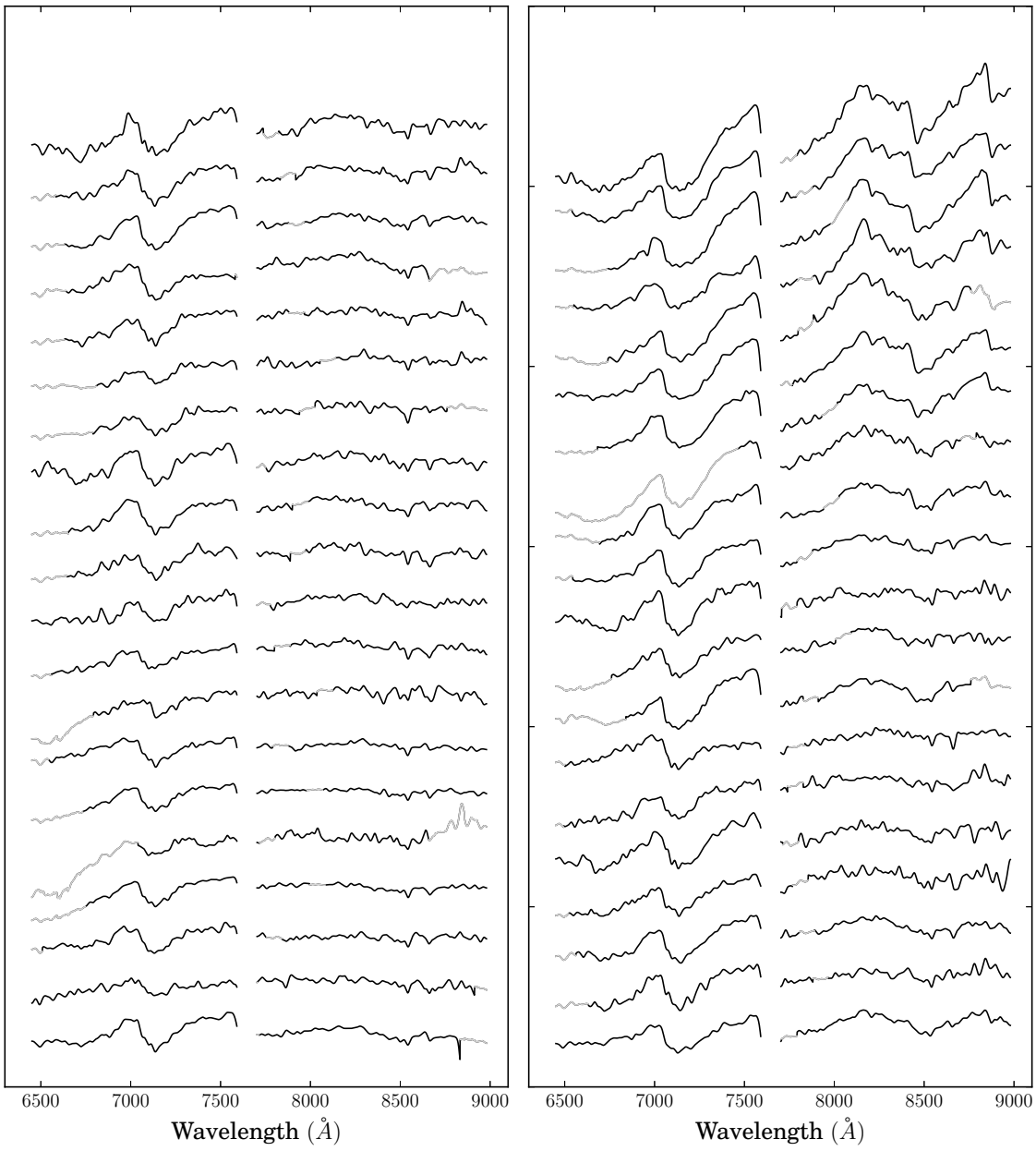

Figure 4.4: Sample M-giant spectra plotted in order of increasing $m_{\rm min}$. Earliest M-types are at the bottom left, and increase such that latest M-types are at the top right. Raw data is shown in black, while grey regions represent missing data that were reconstructed using iterative PCA. To select a representative sample, we sorted by M-type and plotted every eleventh spectrum.

4.3.2 Separating the AGB and RGB

Our sample of 533 M-giants contains both AGB and RGB stars. Spectroscopically, these populations can be differentiated by the presence of s-process elements brought to the surface of AGB stars by the TDU. However such signatures are difficult to observe, particularly at the S/N typical of SPLASH spectra. Photometrically (at least at optical wavelengths), the simplest distinction between AGB and RGB stars is where they lie with respect to the TRGB, as AGB stars increase in luminosity after the onset of the TP-AGB phase. Current models indicate that the fraction of TP-AGB stars fainter than the TRGB does not exceed 5% (Girardi *et al.*, 2010; Rosenfield and Marigo, 2014). As a result, the TRGB has been assumed the lower limit of the TP-AGB "region" in many observational surveys (e.g. Albert *et al.*, 2000; Battinelli and Demers, 2000; Melbourne *et al.*, 2012; Boyer *et al.*, 2013).

To differentiate between AGB and RGB stars, we will thus compare their magnitudes to the TRGB. In the satellites of M31 we calculate $I_{\rm TRGB}$ using the relationship between [M/H] and the TRGB magnitude from Bellazzini *et al.* (2004). We use the metallicity measurements presented in McConnachie (2012), converted from [Fe/H] to [M/H] using the relationship from Ferraro *et al.* (1999). Like Ferraro *et al.* (1999) we assume [α/Fe]= 0.28, except in the nine satellites in which [α/Fe] has been measured by Vargas *et al.* (2014). Finally, we convert the calculated absolute magnitudes to apparent magnitudes using the distance moduli listed in McConnachie (2012) (and Chapter 3). The uncertainties on these distance moduli are the most significant contributor to the uncertainties on $I_{\rm TRGB}$, and are on order 0.05-0.2 mag. In the M31 halo an accurate $I_{\rm TRGB}$ is much more difficult to compute. We will adopt the distance modulus of

M31 (24.47; Stanek and Garnavich, 1998) for all halo fields, which translates to $I_{\rm TRGB} = 20.47$.

We define likely AGB stars to be those M-giants at least 0.1 magnitudes brighter than the TRGB, and likely RGB stars to be those M-giants at least 0.1 magnitudes fainter than the TRGB. The stars brighter/fainter than the TRGB but within the 0.2 mag buffer region we classify as tentative AGB/RGB stars. We also classify stars as tentative AGB/RGB if they are located in a halo field, as we cannot be sure that our assumption of $I_{\rm TRGB}$ is accurate. This splits our sample of 533 M-giants into 58 likely AGB stars, 20 uncertain AGB stars, 89 likely RGB stars, 348 tentative RGB stars, and 18 that could not be classified.

4.4 Spatial distribution of M31 M-giants

We identify M-giants in 41 of the ~ 60 SPLASH fields, including seven of the dSphs, all three dEs, M32, and 19 fields with known substructure. RGB stars (including the uncertain RGB stars) are ubiquitous, and are present in 38 of these fields. AGB stars (including the uncertain AGB stars) are slightly less common, and we observe them in 16 fields. For the satellite fields, Figure 4.5 shows the M-giants' positions within their host galaxy. These maps do not cover the halo and substructure fields, where there is no central reference point. In this section we will discuss the significance of the regions in which we do/do not see AGB stars. Because each field was observed using a different spectroscopic selection function, we cannot easily compare the M-giant populations in different fields. However, the probability of observing oxygen-rich versus carbon-rich AGB stars is independent of the spectroscopic selection, and so the fraction of C- versus M-stars will be discussed.

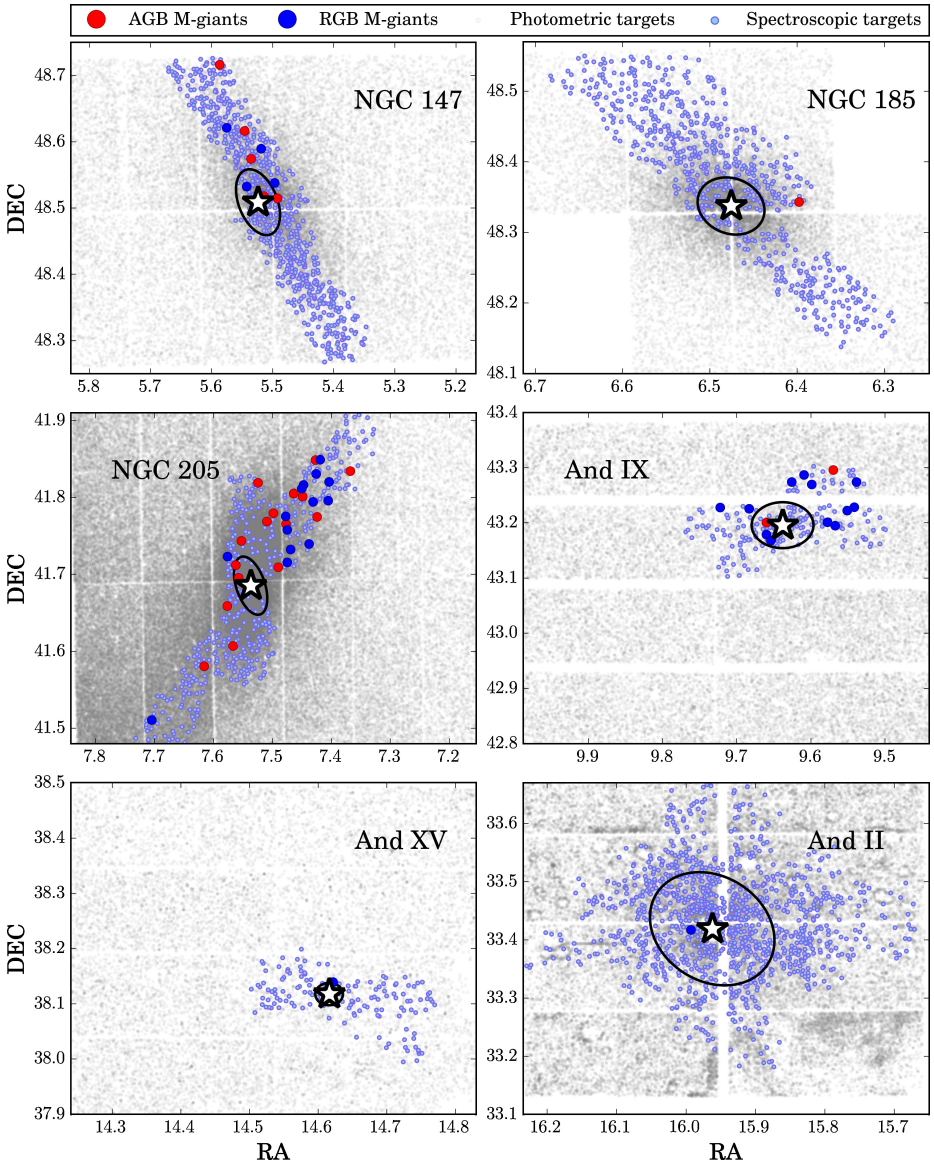

Figure 4.5: Map of M-giants in their host satellites. The full photometric sample is plotted grey, with the SPLASH spectroscopic targets overlayed in light blue. M-giants on the RGB are noted as blue circles, while M-giants on the AGB are in red. Each panel shows RA and DEC (in degrees), and is slightly stretched such that the full spectroscopic survey area fills the panel. We have annotated the galaxy center with a star, and included the half-light radius (McConnachie, 2012) as an ellipse.

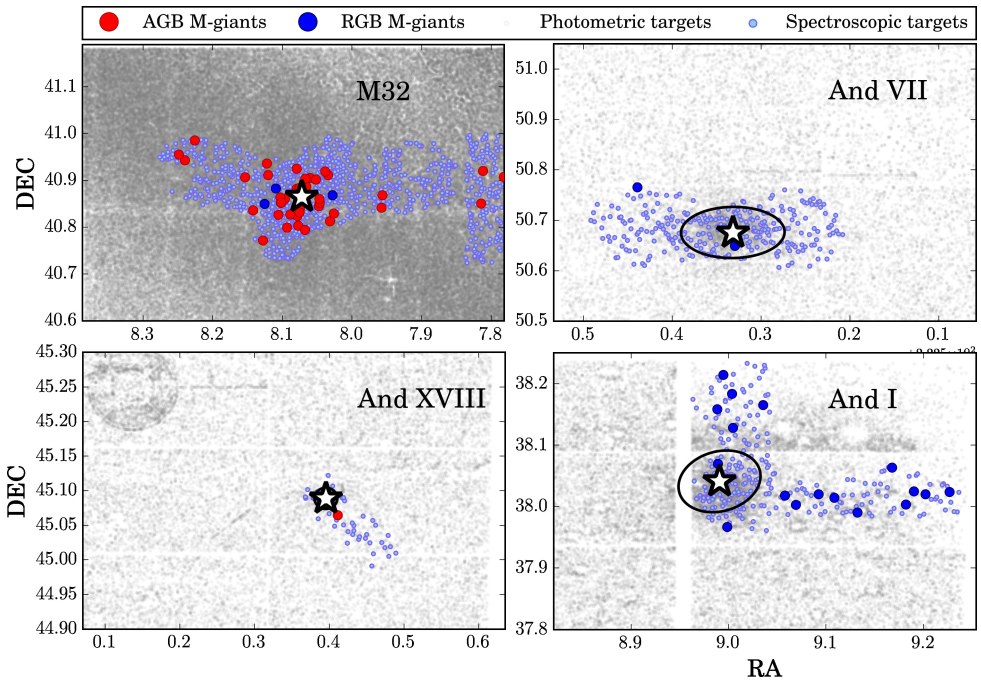

Figure 4.6: Figure 4.5, continued

The presence of a significant number of M-type AGB stars in a field points to a presence of an intermediate-age population. The only galaxies in which we observe many M-giants on the AGB are NGC 147, NGC 205 and M32, which have been previously identified as having intermediate-age stars (e.g., Nowotny *et al.*, 2003; Battinelli and Demers, 2004b,a; Davidge, 2005, 2014; Jones *et al.*, 2015). In each of these fields more than 50% of our M-giant sample is on the AGB, and AGB M-giants represent between 15% (NGC 147) and 74% (M32) of the full spectroscopic sample. We do not see many AGB stars (or indeed M-giants of any type) in NGC 185, which is surprising given the number of M-giants found by photometric surveys (Nowotny *et al.*, 2003; Battinelli and Demers, 2004b; Davidge, 2005). This is an effect of our Na I criterium, as only 22 of the 627 stars observed by SPLASH in the vicinity of NGC 185 have $EW_{NaI} <= 3$. We also observe two M-type AGB stars in And IX (14% of the M-giant sample), and one M-type AGB star in And XVIII (100% of the M-giant sample). However, these stars represent 3% and 5% of the spectroscopic samples in their respective satellites, and thus do not constitute an intermediate age population.

In several of the satellites in which we see M-type AGB stars, we have also identified carbon stars (Chapter 3 of this work). There is no difference in how carbon stars and M-giants were selected for observation by SPLASH, so we can use these carbon star counts to calculate rudimentary C/M ratios. We restrict the carbon star count to those brighter than the TRGB, to ensure that we are counting only the intrinsic carbon stars on the AGB. Table 4.1 shows the calculated C/M ratios for these six fields.

In the three dEs, our computed C/M ratio is much higher than was calculated by previous authors (Demers *et al.*, 2003; Battinelli and Demers, 2004a,b) because we include a

Na I criterium to limit contamination from foreground dwarfs while previous (photometric) surveys relied on statistical arguments to address foreground contamination. The true C/M ratios are likely somewhere between our spectroscopic results and previous photometric results.

In M32 we detect a significant number of M-type AGB stars, and one (member) carbon star. We thus compute a C/M ratio of 0.03 ± 0.03. Using the relationship between [Fe/H] and log(C/M0+) from Cioni (2009), this corresponds to [Fe/H]= -0.64 ± 0.27. The stellar populations within M32 are known to vary with radius (Coelho *et al.*, 2009), so it also instructive to look at the C/M ratio in a more defined region. If we restrict our counts to within five effective radii of the galaxy center, our measured C/M ratio increases to C/M= 0.05 ± 0.05, and the associated [Fe/H] decreases to [Fe/H]= -0.79 ± 0.25. Both of these estimates are more metal-poor than recent isochrone-based metallicity measurements (Monachesi *et al.*, 2012); mass-weighted mean metallicity of [M/H]= -0.01 ± 0.08 dex or the peak of the mean metallicity distribution [M/H]$\simeq -0.2$. They are, however, consistent with the mean metallicity computed using integrated light spectroscopy, [M/H]$\simeq -0.6$ (Coelho *et al.*, 2009).

We have also identified carbon stars in And II, And V, and And X though we see no M-type AGB stars. In And V and And X this is unsurprising, as no significant intermediate age population has ever been observed. And II, however, has been shown to have an intermediate age population (Kerschbaum *et al.*, 2004; Weisz *et al.*, 2014). We do not observe M-type AGB stars because only $\sim 8\%$ of the stars given high priority for spectroscopic selection are brighter than the TRGB, many of which are then removed by the membership criteria. This is thus an observational effect.

Of the eight halo fields that contain AGB stars (with the caveat that our distance

Table 4.1: C/M ratios in SPLASH satellite/halo fields

Field	$N_{\rm M}$[a]	$N_{\rm C}$[b]	C/M ratio
NGC 147	5	3	0.6 ± 0.44
NGC 185	1	2	$2.0^{2.4}_{2.0}$
NGC 205	16	6	0.38 ± 0.18
M32 (average)	39	1	0.03 ± 0.03
M32 ($r \leq 5r_{\rm eff}$)	19	1	0.05 ± 0.05
And IX	2	0	0
And XVIII	1	0	0
Northwest shelf	4	1	$0.25^{0.28}_{0.25}$
Northeast shelf[†]	9	3	0.33 ± 0.22

[a] Number of M-type AGB stars
[b] Number of carbon stars *brighter* than the TRGB
[†] Using the $I_{\rm TRGB}$ described in the text

modulus assumption may not be accurate), four contain substructure known to be associated with the M31's giant southern stream (GSS). Several of these fields target the Northwest Shelf, in which we have also found carbon stars. We find C/M= $0.25^{0.28}_{0.25}$, which corresponds to [Fe/H]= -1.11 ± -0.24. In the other halo fields, the total number of identified AGB stars is too small to be significant.

The final fields we will pay particular attention to are those associated with the Northeast shelf. We identify eight M-giants with magnitudes slightly fainter than our assumed $I_{\rm TRGB}$ of 20.47. However we also observed three carbon stars, also all fainter than $I_{\rm TRGB}$. It is possible that this represents an intermediate age population that has been affected by some systematic offset in the calibration of the original photometry. If we instead adopt $I_{\rm TRGB}$ = 21.41, chosen to encompass the faintest carbon star, then all eight M-giants would be classified as AGB stars. This would return C/M= 0.38 ± 0.25, which corresponds to [Fe/H]= -1.19 ± 0.15. This

is consistent with observations that the metallicities of the NE and NW shelves are very similar (Ferguson *et al.*, 2005). Note that a one magnitude change in the distance modulus represents a tremendous change in physical distance, so it is highly unlikely that these stars are AGB stars that are truly as distant as their magnitudes suggest. It is however possible that they are RGB stars and extrinsic carbon stars in the M31 halo. However, given that intermediate age populations are known to exist in debris associated with the GSS, we believe that a calibration error is the most likely explanation for these luminosities.

4.5 Physical Properties of M31 M-giants

Our sample of M-giants covers a wide range of environments. In this section we explore the range of properties they possess, and the nuances involved in calculating these properties. We focus on effective temperature ($T_{\rm eff}$), dust and dynamics, and metallicity. Finally, we discuss difference between the AGB and RGB populations.

4.5.1 Effective Temperature

M-giants are characterized by atmospheres cool enough to harbor TiO, typically $T_{\rm eff} <$ 4000K. As TiO is highly temperature-dependent, its strength is a good way to measure an M-giant's $T_{\rm eff}$. Indeed it is one of the only ways to measure $T_{\rm eff}$, as the broad TiO bandheads obscure many features that can be used as temperature proxies in warmer stars. In this section we will attempt to measure $T_{\rm eff}$ in our sample using empirical relationships from the literature and direct comparison to models.

In Section 4.3.1 we parametrized the TiO band strength and calculated a spectral subtype for each star. As a reminder, we defined a star's M-type to be that which minimizes the distance between each SPLASH star in S-index space and the locus defined by F94 (see Figure 4.2). The top panel of Figure 4.7 illustrates the distribution of M-types for AGB and RGB stars. In general, the type varies from M2 to M9. The AGB population is skewed to slightly higher M-types (i.e., cooler temperatures), regardless of whether or not the uncertain designations are included. This is not unexpected, as AGB stars are are known to be particularly red and particularly dusty.

The relationship between spectral type and $T_{\rm eff}$ is well documented (e.g., Dyck *et al.*, 1996, 1998; van Belle *et al.*, 1999). Panels a and b of Figure 4.7 demonstrate $T_{\rm eff}$ derived with two of these relationships, one from the table provided by F94 and the second from the empirical equation in van Belle *et al.* (1999). The two methods return very different temperature distributions, with the mean F94 distribution $\sim$ 585K cooler than the van Belle *et al.* (1999) distribution. In both, the AGB stars are cooler than their RGB counterparts (which follows directly from their different M-types).

We can also estimate $T_{\rm eff}$ by comparing our M-giant spectra directly to synthetic spectra. To do this, we perform a χ^2 fit against a grid of model spectra from Aringer *et al.* (2016, hereafter A16). These models cover a range of surface gravities, effective temperatures, metallicities, stellar masses, and C/O ratios. For the purposes of $T_{\rm eff}$ estimation we include all stellar masses and C/O ratios in our grid, but do not include those models with unusual O/N/Zr/Y abundances. The basic grid we use span the following properties; $-1.5 < \log g < 1.5$, $-2 <$ [Fe/H] < 1.0, $2600 < T_{\rm eff} <$ 5000K. Because temperature and metallicity are highly de-

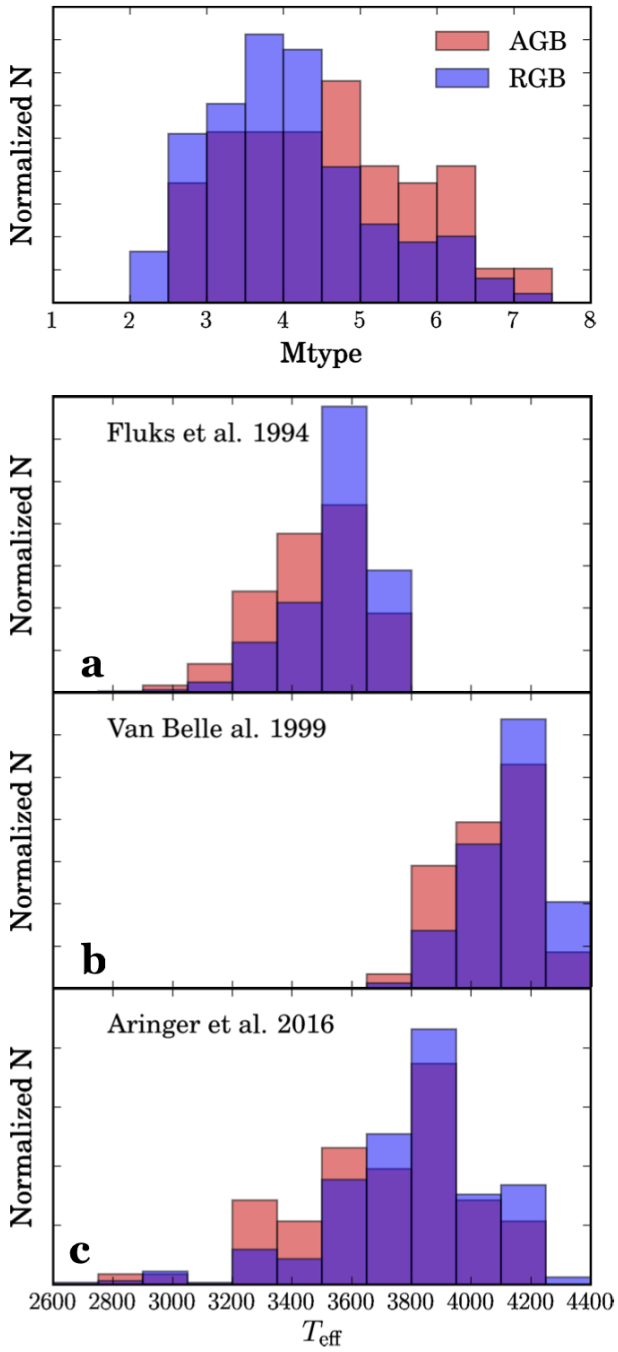

Figure 4.7: The top panel shows the distribution of M-types for both AGB (red) and RGB (blue) stars, in which AGB stars are skewed to slightly later types. The next two panels show the distribution of $T_{\rm eff}$s given two empirical relationships between M-type and temperature. Panel (a) uses an interpolation on the relationship from F94, and panel (b) uses the equation from van Belle *et al.* (1999). The final panel (c) shows the distribution of $T_{\rm eff}$ derived by comparison to A16 models. The temperature distributions derived using each of these methods are quite different.

generate, we also compute the best fitting $T_{\rm eff}$ for different metallicity-based subsets of this grid.

The distributions of computed $T_{\rm eff}$ is shown in Figure 4.8 for three subsets of our grid of A16 models. The first (shown in blue) uses all available parameters. The next two show the best fitting temperatures for those models with $-0.5 < [{\rm Fe/H}] < 0$ (green) and [Fe/H]< -1 (red). The temperature of a single star changes by an average of 90K from the full grid to the more metal rich subset (while the minimum χ^2 value increases by an average of 8%), and by an average of 300K from the full or metal rich subset to the metal poor subset (where the average best χ^2 increases by 50%). The temperature difference does not depend on $V-I$, CN–TiO, or either of the temperature estimates themselves.

The bottom-most panel of Figure 4.7 shows the distributions of χ^2 calculated $T_{\rm eff}$ for AGB and RGB stars using the full A16 grid. Both distributions peak at $\sim$ 3900K, essentially centered between the F94 and van Belle *et al.* (1999) based temperatures. The range of temperatures estimated by this method is much wider than either of the two spectral typed based methods.

Overall, AGB stars have higher M-types than RGB stars. When spectral type drives the temperature estimate, this results in AGB stars appearing cooler than the RGB stars. However, when temperature is calculated independent of spectral type, this difference disappears. Statistically, this can be represented by the results of K-S tests; when comparing the distributions of AGB and RGB M-type we get $p = 0.002$, while when comparing the distributions of $T_{\rm eff}$ we find $p = 0.4$. This suggests that metallicity the driver of the difference in M-types, and AGB stars have higher metallicities than RGB stars. This could be an effect of location, where AGB

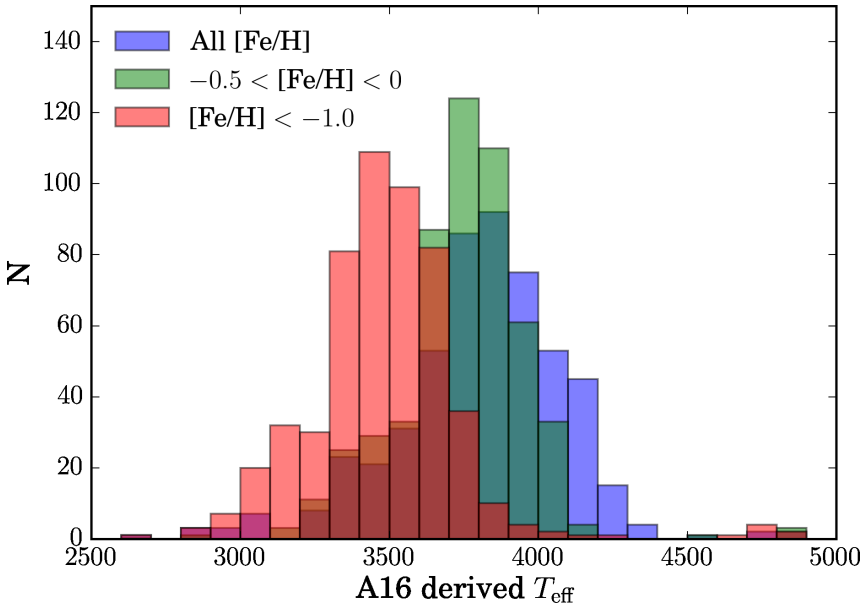

Figure 4.8: M-giant $T_{\rm eff}$ derived by χ^2 comparison with A16 models. We include the results from three subsets of the A16 model grid, including all available [Fe/H] (blue), $-0.5 <$ [Fe/H] $<$ 0.0 (green) and [Fe/H]< -1.0 (red). Due to the degeneracy between [Fe/H] and $T_{\rm eff}$, the temperature of a star's best fitting model changes significantly at different metallicities.

stars are preferentially located in the higher metallicity fields (e.g., M32 and the dEs). However, we do not have a large enough sample of AGB stars in any single field type (dE, dSph, halo, cE) to do a statistically meaningful comparison of homogenous populations.

4.5.2 Stellar Dust and Variability

TP-AGB stars are known for their variability and dust production. M-giants (and their carbon-rich counterparts) on the AGB have been observed with photometric variations on time scales from a few tens to several hundred days with amplitudes of up to several magnitudes. In addition, they return significant amounts of mass (in the form of gas and dust) to the interstellar medium via stellar winds (e.g., Gehrz, 1989). Many are so extincted as to become invisible at optical wavelengths (e.g., Nowotny *et al.*, 2013). While RGB stars may also be variable, they do not lose their mass to a a comparable extent.

These particular properties are best studied using multiple epochs of mid-infrared (MIR) observations. Several large-scale surveys have used the *Spitzer Space Telescope* to this end (e.g., Blum *et al.*, 2006; Boyer *et al.*, 2011). Fortunately, there is overlap between the fields observed by *Spitzer* and the SPLASH fields. In addition, our broad-band photometry was observed at a different epoch than the spectroscopy, and can thus provide a modicum of multi-epoch information.

We begin by looking at the M-giants in CN–TiO versus $V-I$ color-color space (Figure 4.9). Combined, these two colors make up the four-band photometry system that has been used to study AGB stars throughout the Local Group (e.g., Nowotny *et al.*, 2003; Battinelli and Demers, 2004a,b, 2009; Wing, 2007). As we synthesized CN–TiO directly from the spectra,

it represents the properties of the star at a different point in time than the $V-I$ color. In Figure 4.9 the full SPLASH sample is shown in grey, while the AGB and RGB stars are plotted in red and blue (respectively). We distinguish between certain and uncertain designations by shape (circles and crosses, respectively). We also plot synthetic photometry from the dust-free hydrostatic models from A16.

Overall there is a good fit between the models and the observations. Approximately 5% of the M-giants are redder in $V-I$ than predicted for their CN–TiO color (we include a dashed black line on Figure 4.9 marking this sample). The majority of those that deviate from the models are AGB stars, and by fraction more AGB stars lie outside the model sequence than RGB stars. This is consistent with conventional wisdom that AGB stars are more dusty and more dynamic than RGB stars. Very few M-giants are scattered in the opposite direction, blueward of the $V-I$ color predicted for the CN–TiO color. There is a small clump of stars at $V-I \simeq 1.3$ with stronger TiO features (i.e., more negative CN–TiO color) than predicted by the models. Four these are early M-type stars with a slight gap between the blue and red DEIMOS chips. However, three have very deep TiO bands.

Next we compare the SPLASH sample with *Spitzer* observations. The Survey of Dust in Nearby Galaxies with *Spitzer* (DUSTiNGS, Boyer *et al.*, 2015) imaged 50 nearby dwarf galaxies at 3.6 and 4.5 μm using the InfraRed Array Camera (IRAC; Fazio *et al.*, 2004). Of the 1749 stars with SPLASH spectra that fall within the DUSTiNGS footprints, 23 are M-giants. These 23 stars are comprised of 13 RGB stars, 5 AGB stars, 3 uncertain RGB stars, and 2 uncertain AGB stars. These stars are shown in their corresponding DUSTiNGS [3.6] versus [3.6]–[4.5] CMDs in Figure 4.10. Interestingly, many of the AGB stars are fainter than

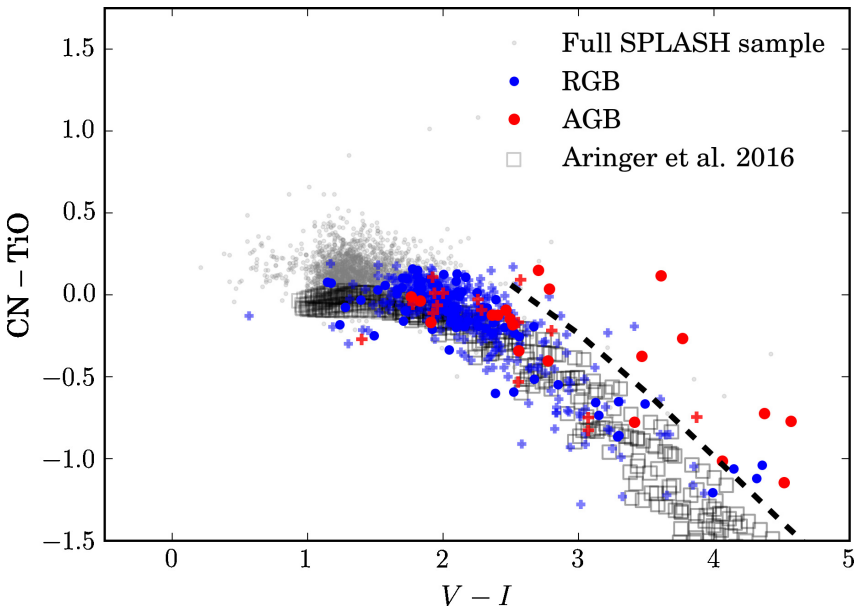

Figure 4.9: CN–TiO versus $V-I$ color-color diagram. AGB stars are shown in red while RGB stars are shown in blue, with certain and uncertain designations plotted as circles and plus signs respectively. For comparison, the non M-giant portion of the SPLASH sample is plotted in grey, and the cool star models from Aringer *et al.* (2016) are overlaid as black squares. The black dashed line indicates the edge of what may be considered the region of stars effected by dust and/or dynamics.

the TRGB in 3.6μm despite being brighter than $I_{\rm TRGB}$. This is unlikely to be due solely to uncertainties on the (optical or MIR) TRGB, as typical uncertainties are far less than the ~ 2 magnitude differences we see here.

Figure 4.11 shows our sample of M-giants in [3.6]–[4.5] versus $V-I$ color-color space. To avoid Eddington bias, we restrict the M-giants plotted to AGB stars, and RGB/uncertain stars at least one magnitude brighter than the DUSTiNGS detection limit ($M_{3.6} \leq -6$mag). This removes 13 stars, as well as the match in M32 that has no $V-I$ color. There is a significant amount of scatter towards large [3.6]–[4.5] colors. This is particularly true at bluer $V-I$ colors, though this may be a selection effect given the paucity of M-giants observed with $V-I > 3$. The scatter pushes many of the stars into the regime that might classify them as "extreme" (x-) AGB stars were it not for their very blue $V-I$ color (e.g., Blum *et al.*, 2006; Boyer *et al.*, 2015). X-AGB stars are known to be highly variable, and are typically losing dusty mass at such a rate as to be invisible in the optical and extremely red in the MIR. However, x-AGB stars are brighter than the 3.6μm TRGB, and none of the stars in the SPLASH-DUSTiNGS overlap are both bright in 3.6μm and particularly red in [3.6]–[4.5].

The nature of this scatter is unclear, as it has not been observed in other fields (Aringer, private communication). Overall, the AGB stars do not seem to exhibit any more deviation from the models than their RGB counterparts, despite being typically more impacted by dust and dynamics (for which these hydrostatic models do not account). It is likely a purely observational effect, a result of photometric uncertainties at these magnitudes, as Figure 4.10 illustrates that there is more scatter redward of [3.6]–[4.6]= 0 than blueward.

We find that only the three reddest (two AGB stars and one RGB star) stars in Fig-

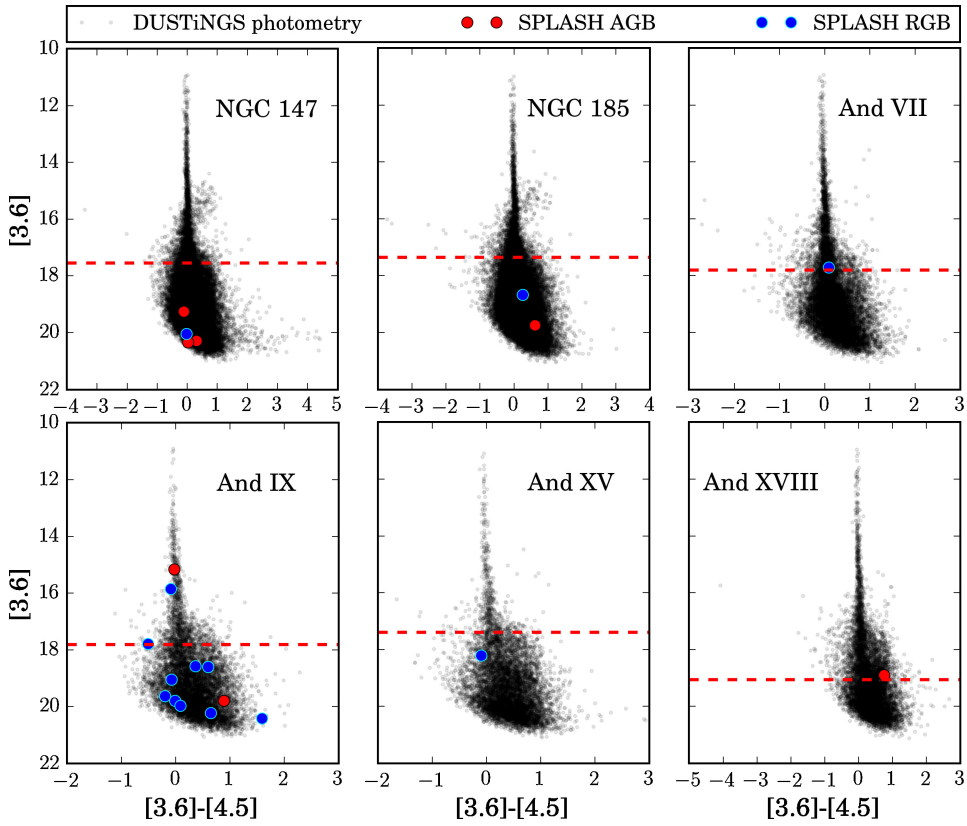

Figure 4.10: DUSTiNGS [3.6] versus [3.6]-[4.5] color magnitude diagrams for the six fields in which there are M-giants spectroscopically identified by SPLASH. DUSTiNGS photometry is shown in grey, and SPLASH points are highlighted as red (likely AGB stars) and blue (likely RGB stars). The TRGB (at roughtly $M_{[3.6]} = -6.6$ is noted by a dashed red line. Despite being selected to be brighter than the optical TRGB, many of the SPLASH AGB stars are fainter than the TRGB in 3.6μm.

ure 4.11 lie in the “dynamic" region of Figure 4.9 (i.e., to the right/above the black dashed line). Two of these stars are perfectly coincident with the models in [3.6]–[4.5] versus $V-I$ color-color space, while the third is red enough to be an x-AGB candidate ([3.6]–[4.5]$>$ 0.5). It is possible that this star is an “extreme" AGB (X-AGB) candidate that resides below the 3.6μm TRGB temporarily due to its variability. However, none of these three stars (or the other 20 M-giants in the SPLASH-DUSTiNGS overlap) appear in the DUSTiNGS variable/X-AGB star catalog. While this does not rule out variability completely, as the catalog is based on only two epochs, it makes it less likely. In particular, those AGB stars fainter than the 3.6μm TRGB but brighter than $I_{\rm TRGB}$ are likely variable.

M32 has also been imaged with *Spitzer* (Jones *et al.*, 2015). Of the nine total matches between SPLASH footprint and the catalog from Jones *et al.* (2015), one is a confirmed M-giant. This single match is harder to interpret. It is detected in 3.6 and 5.8μm. Howver, X-AGB criteria rely on either [3.6]–[4.5] or [3.6]–[8] color, so it is not immediately apparent whether this star (with [3.6]–[5.8] = 0.368 ± 0.13) is an X-AGB candidate. However, we do have the distribution of [3.6]–[5.8] colors for X-AGB candidates and non X-AGB candidates in M32. Applying Bayes theorem, we determine that our M-giant is twice as likely *not* to be an X-AGB star than it is to be an X-AGB star.

Our takeaway from this analysis is that our sample of M-giants is at most mildly pulsating, and minimally effected by dust.

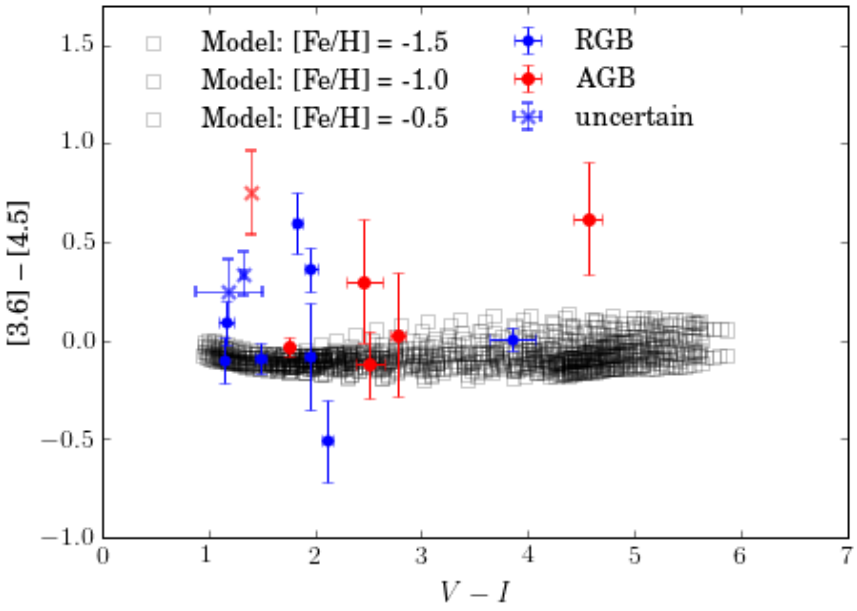

Figure 4.11: [3.6]–[4.5] versus $V-I$ color-color diagram. Colors and shapes are the same as Figure 4.9. There is a plume of stars that are quite red in [3.6]–[4.5] while quite blue in $V-I$, which we cannot explain.

4.5.3 Metallicity

A common method of measuring the metallicity of low resolution or low S/N spectra is using the Ca II triplet (CaT) at $\sim$ 8500Å. The relationship between the CaT equivalent width (EW) and [Fe/H] has been well calibrated for RGB stars at a range of ages and metallicities(Rutledge *et al.*, 1997; Carrera *et al.*, 2007; Starkenburg *et al.*, 2010; Carrera *et al.*, 2013), and has been used throughout the Local Group (e.g., Gilbert *et al.*, 2006, 2012; Ho *et al.*, 2015). While age has not found to significantly impact this calibration (Cole *et al.*, 2004), the CaT is sensitive to surface gravity in temperature and metallicity dependent ways (Jorgensen *et al.*, 1992; S.V., 1997). As a result, it manifests differently in AGB stars versus RGB stars, and may well be different in M-giants versus warmer stars. Observations have found that there is a discrepancy between spectroscopic and photometric metallicities when intermediate-age stars are present (Lianou *et al.*, 2011), but the precise differences between the CaT on the AGB and the RGB have not been thoroughly mapped out. While a complete calibration of the relationship between the CaT and [Fe/H] requires higher resolution spectra than we have available, we can still explore the differences in how the CaT appears in our sample.

We restrict our CaT EW calculations to those spectra with S/N$>$ 3 pixel^{-1} at the CaT ($8560 < \lambda < 8640$Å). This is the limit at which Ho *et al.* (2015) find that the true EW of model spectra could be recovered within an error of 30%. This removes 33 spectra, all RGB stars. For the remaining 445 M-giants, we compute the total equivalent width to be the unweighted sum of the two stronger lines.

$$\Sigma\mathrm{Ca} = \mathrm{EW}_{8542} + \mathrm{EW}_{8662} \tag{4.5}$$

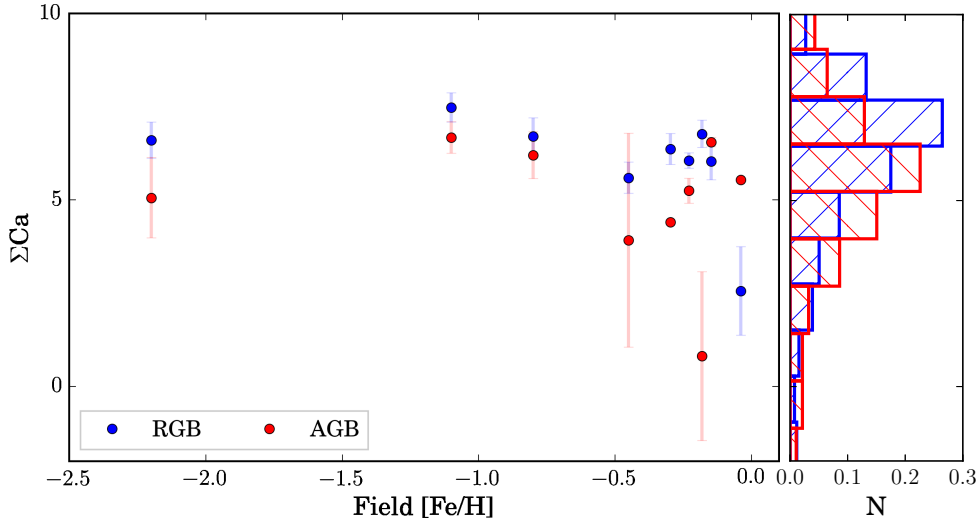

Figure 4.12: Distributions of ΣCa for AGB (red) versus RGB (blue) stars. The left panel shows mean ΣCa as a function of environment, where the x-axis is the estimated [Fe/H] of the field to which the stars belong. In seven of the nine fields the AGB stars have a lower average ΣCa than the RGB stars. The right panel shows these distributions in aggregate, and the AGB stars are skewed to smaller ΣCa values.

We exclude the weakest line, which Ho *et al.* (2015) found add more noise than signal at the S/N of these data.

Figure 4.12 illustrates the distribution of mean ΣCa in fields with measurements for both AGB and RGB stars. In the satellite fields, the metallicity shown is the mean [Fe/H] from the literature (McConnachie, 2012). In the halo fields, we compute the mean projected distance from M31 and compute [Fe/H] given the radial gradient from Gilbert *et al.* (2014). In seven of the nine fields, the mean ΣCa of the AGB stars is smaller than that of the RGB stars. The right panel of Figure 4.12 illustrates this in aggregate, with the distribution of ΣCa for the AGB stars skewing slightly lower than the distribution for the RGB stars (with means of 5.22 ± 0.3 and 6.1 ± 0.17, respectively).

For the fields with known distance modulus, we can convert ΣCa to [Fe/H] using the two-line calibration from Carrera *et al.* (2013), as presented in Ho *et al.* (2015),

$$\begin{aligned}[\mathrm{Fe/H}] &= -3.51 + 0.12 \times M_I + 0.57 \times \Sigma\mathrm{Ca} \\ &\quad -0.17 \times \Sigma\mathrm{Ca}^{-1.5} + 0.02 \times \Sigma\mathrm{Ca} \times \mathrm{M_I} \end{aligned} \tag{4.6}$$

where M_I is the absolute I-band magnitude.

Figure 4.13 illustrates the results of this conversion. Despite the interaction term in this equation, the offsets between the AGB and RGB distributions match those in Figure 4.12. In four of the six fields, the RGB stars have higher average metallicities than the AGB stars (with the mean marked by a star). It is unlikely that AGB stars are systematically more metal-poor than their RGB counterparts, particularly given that § 4.5.1 indicated that their TiO bands are consistent with being more metal-rich. Instead, the offsets that we observe are likely due to differences in the temperature structure of the outer atmospheres of AGB versus RGB stars.

If the CaT appears systematically weaker AGB stars, then using the CaT to calculated [Fe/H] will return a lower metallicity in fields with RGB and AGB stars than in fields with AGB stars alone. The effect of AGB contamination has been modeled using NTLE line-formation data and theoretical stellar evolution models, and was found to be minimal (with an error in [Fe/H] of ~ 0.02 dex per star, Cole *et al.*, 2000). We can use the information in Figure 4.13 to investigate this contamination. We begin with the full sample of RGB stars (whose mean is shown as a dashed red line in Figure 4.14). To this we add increasingly large numbers of AGB stars randomly sampled without replacement from the AGB sample. We then compute the mean

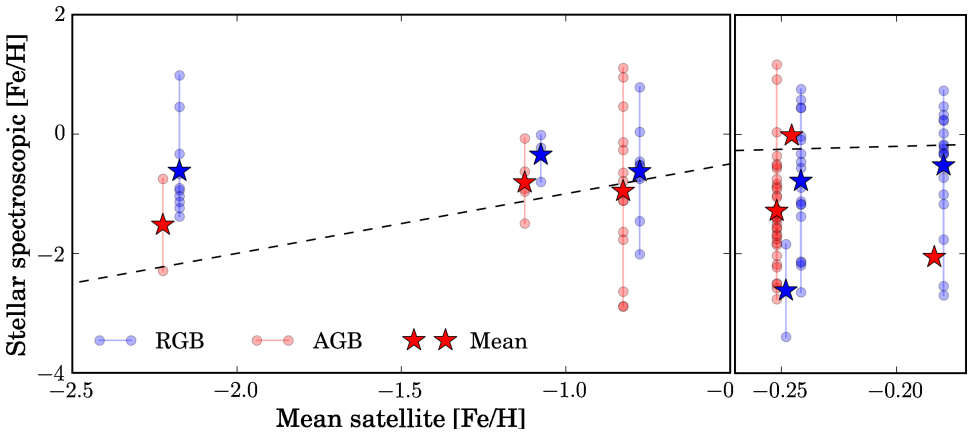

Figure 4.13: CaT-based [Fe/H] of M-giants as a function of mean environmental metallicity. Calculated [Fe/H] values for individual AGB and RGB stars are plotted as red or blue circles, respectively, while the means for each field are plotted as stars. AGB stars are offset slightly to teh left estimated [Fe/H] of their host satellite/field, while RGB stars are offset slightly to the right. The dashed black line indicates the 1-to-1 relationship. Both panels contain the same information, the right is presented on a different x-axis scale to allow easier visualization.

ΣCa of the combined RGB+AGB sample and convert it to [Fe/H]. To estimate the uncertainties, we do this 250 times and combine the results. Figure 4.14 shows the results of this exercise. The change in mean [Fe/H] increases with the fraction of AGB stars, increasing to 0.2dex when AGB contamination is $\sim 50\%$. This is comparable to typical error in abundance measurements, so may be problematic for the best-measured [Fe/H].

Finally, neither ΣCa (Figure 4.12) nor CaT-based [Fe/H] (Figure 4.13) show a tight relationship with the mean metallicity of the field. The mean metallicities were derived using several methods, including CaT EW of coadded spectra (And IX, Collins *et al.*, 2010), CaT EW of un-coadded spectra (NGC 185, NGC 147, Geha *et al.*, 2010), isochrones (M32 Grillmair *et al.*, 1996), and interpolation on the M31 halo metallicity gradient at different radial distances (Gilbert *et al.*, 2014). The closest matches are with NGC 205 and NGC 147, whose mean

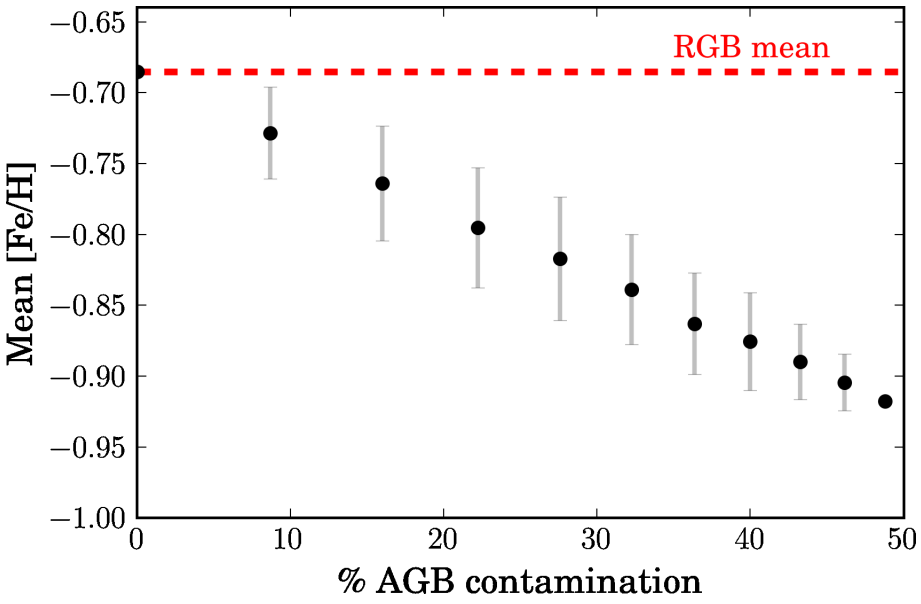

Figure 4.14: Mean ΣCa as a function of fraction of AGB contamination, with 1σ uncertainties computed through repeated trials. The mean of the clean RGB sample is shown as a dashed red line. The population's mean ΣCa decreases steadily as more AGB stars are included.

metallicities were calculated using SPLASH data. The offset is not in a consistent direction; in the metal-poor fields the CaT-based metallicities are higher than the mean metallicities, while in metal-rich fields the CaT-based metallicities are lower than the mean metallicities. This suggests that the CaT is not a well-calibrated absolute metallicity indicator for M-giants.

4.5.4 The AGB versus the RGB

The previous subsections have illustrated minor differences between the AGB and RGB spectra. Our AGB sample have slightly later spectral types than the RGB stars, are more likely to deviate from the relationship between CN–TIO and $V-I$, and have slightly weaker CaT EWs. In this section, we apply Principle Component Analysis (PCA) to tease out any significant differences we have not yet observed.

The PCA algorithm as it relates to spectra has been thoroughly laid out elsewhere (e.g., Yip *et al.*, 2004, and Chapter 3 of this work), but we will briefly summarize it here. PCA in general is a technique for dimensionality reduction, which converts a set of observations of potentially correlated properties to an orthogonal, uncorrelated, basis set. Within the PCA framework, each spectrum can be described as a linear combination of "eigenspectra". Mathematically, this is represented as

$$x_i = \mu + \sum_{j=1}^{N} a_{ij} e_j \tag{4.7}$$

where x_i is the i-th spectrum of the sample, μ is the mean spectrum (which is also the first eigenspectrum), e_j is the j-th eigenspectrum, and a_{ij} is the j-th eigencoefficient of spectrum i.

To compute the eigenspectra, eigenvalues, and eigencoefficients of our sample of M-giants, we use the iterative PCA formalism set forth by Yip *et al.* (2004) in the `astroML` Python library.

A major limitation of PCA in this case is the typical S/N of the SPLASH spectra. PCA endeavors to capture *all* the variance, which in a sample with low S/N is quite substantial. The effect of noise on the eigenspectra is illustrated in Figure 4.15, which presents the predictive power of the first five eigenspectra as a function of various S/N limits and degrees of smoothing. Both S/N limits and smoothing increase the percentage of variance described by the first several eigenspectra, and as a result decrease the number of eigenspectra necessary to represent the full sample. However both also have negative effects; applying a S/N limit reduces the sample size and biases us towards AGB stars and the brightest RGB stars, and large amounts of smoothing removes features that we would like to use PCA to represent. We thus choose modest changes to the sample, with a minimum S/N of 3.5 and Gaussian smoothing with $\sigma \simeq 10$Å. This results in the first five eigenspectra representing 42% of the total variance.

Figure 4.16 show the first five eigenspectra of the full M-giant sample. Each of these eigenspectra features prominent TiO bands (the strongest of which have been labeled), though they do not necessarily show the same TiO bands. All major TiO bands appear in the first (mean) eigenspectrum, though the 8400Å TiO feature is weak. However, the second eigenspectrum does not show TiO absorption at 7000Å while the next three eigenspectrum show very strong 7000Å features. Finally, while the first three eigenspectra show substantial TiO absorption redward of 8000Å, the final two eigenspectra are largely featureless at those wavelengths.

The appearances of TiO in the first five eigenspectra suggest several things. First, that the mean eigenspectrum has TiO absorption at 7000Å while the second eigenspectrum does not

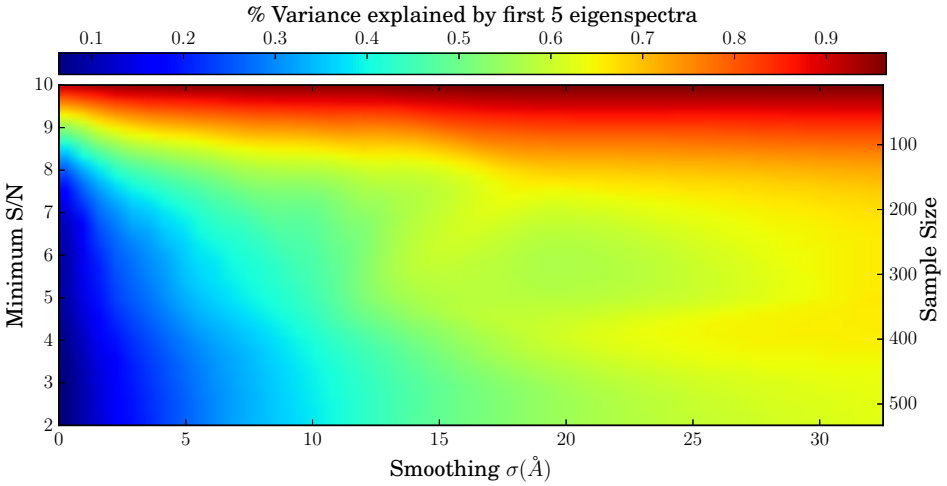

Figure 4.15: Effect of smoothing and S/N cuts on the cumulative percentage of variance explained by the first five eigenspectra. The minimum S/N used to make the sample is indicated on the left y-axis, the number of spectra that meet that S/N criteria is on the right y-axis, and the σ of the smoothing Gaussian applied to that sample is indicated on the x-axis. Color represents the cumulative percentage of variance covered by the first five eigenspectra. Both smoothing and S/N cuts increase the amount of variance explained by the first few eigenspectra, with S/N cuts providing a larger change due to the dual effect of less noise and fewer spectra.

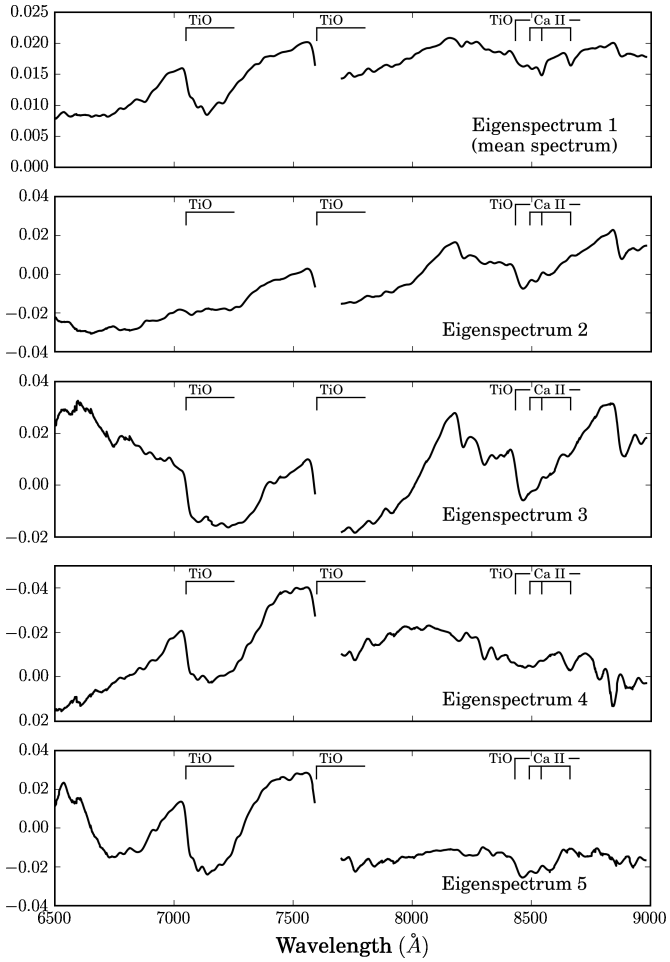

Figure 4.16: First five M-giant eigenspectra, accounting for $\sim 42\%$ of the population's variance. We annotate the major spectral features, including TiO at 7050Å, 7500Å and 8453Å, and the CaT at $\sim$ 8500Å. In the fourth panel we have flipped the eigenspectra over zero such that TiO bands are recognizable as absorption. The y-axis reflects this transformation, and goes from positive to negative.

tells us that many of the M-giants in our sample have very similar 7000Å features. This suggests that this TiO feature saturates before those at redder wavelengths. Very early M-type stars should have weaker features, so the fact that they are not seen suggests that our sample is biased against the earliest M-types. The major difference between the first and second eigenspectra is the strength of the 8400Å and 8900Å TiO bands, illustrating that for our sample these features are the most variable. The very strong TiO features at all locations in the third eigenspectrum likely represents our sample's late-type M-giants. Finally, the relatively featureless red halves of the final two eigenspectra are likely an artifact of our data processing, in which the red and blue DEIMOS chips are not processed identically.

Correlating the eigencoefficients of these eigenspectra (as well as the several hundred eigenspectra not shown) with other observable properties indicates that only two have strong relationships (which we define to be a Spearman's rank correlation coefficient $\rho \geq 0.5$). The second eigenspectrum correlates with $V-I$, CN–TiO, and M-type ($\rho = 0.68, -0.76$ and 0.88, respectively). The third eigenspectrum correlates with CN–TiO ($\rho = -0.72$) and M-type ($\rho = 0.62$), but when compared to $V-I$ is below our correlation threshhold ($\rho = 0.45$). Also just below our threshold is the second eigenspectrum's correlation with ΣCa ($\rho = -0.48$). No eigenspectrum correlates strongly with the mean metallicity of the field.

If we look at the AGB stars alone, some of these correlations strengthen and several other correlations emerge. Both the second and third eigenspectra correlate with ΣCa ($\rho =$ $-0.57, -0.62$, respectively). This is particularly interesting given that the CaT is only clear to the eye in the second eigenspectrum. These two eigenspectra also correlate with $V-I$ ($\rho =$ 0.63 for both), CN–TiO ($\rho = -0.84, -0.85$), and M-type ($rho = 0.85, 0.78$). Finally, the 30th

eigenspectrum emerges as correlating with $V-I$ ($\rho = 0.57$). There is still no eigenspectrum that correlates strongly with the mean metallicity of the field.

If we compare AGB versus RGB eigencoefficients for every eigenspectrum, we find 27 cases for which a K-S test returns $p < 0.05$. We have plotted the first three differing distributions of eigencoefficients in Figure 4.17. As the eigencoefficients of the second (EC_2) and third (EC_3) eigenspectra correlate with various observables, we can interpret these distributions. AGB stars have, on average, slightly lower EC_2 values. This corresponds to redder $V-I$ colors, more positive CN–TiO colors (i.e. weaker TiO bands), and later Mtypes. This is consistent with what we observed in the previous sections. The remaining eigencoefficients are more difficult to interpret.

The primary result of this exercise, and the application of PCA to M-giants as a whole, is that TiO is a complicated molecule. Its depth and shape depends on both the stellar properties that are easily observable (color, temperature, metallicity), but also on a host of properties that we are unable to distinguish. The spectra of AGB and RGB stars do differ, but by small amounts and in ways that are difficult to predict and understand. There are, however, takeaways. First, the 7000 TiO feature appears in most of our spectra at comparable strength, while the 8400 TiO feature changes significantly. Next, the CaT always appears in eigenspectra that also have a significant TiO feature at similar wavelengths, suggesting that the behavior of the CaT in M-giants is very tightly related to the behavior of TiO.

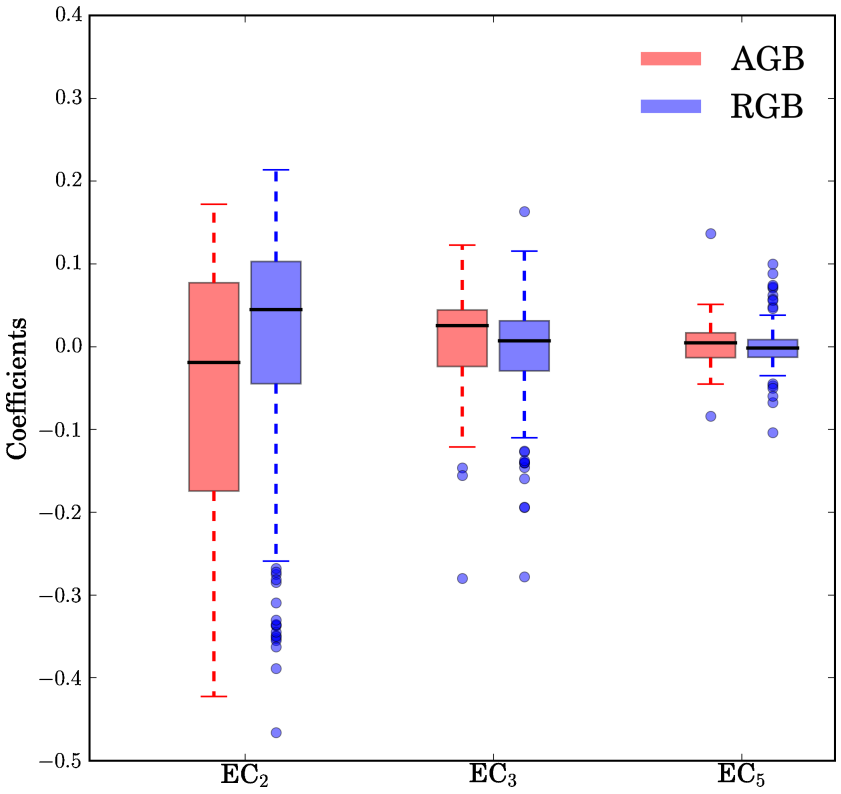

Figure 4.17: Distribution of eigencoefficients of the second M-giant eigenspectrum, which correlates with $V-I$, CN–TIO, and M-type. The distribution for AGB stars is shown in red, while the RGB stars are represented in blue. The median is indicated by a black line, the first and third quartiles indicated by the colored box. The whiskers extend 1.5 times the interquartile range past the quartiles. Outliers beyond that are shown as circles.

4.6 Summary and Conclusions

We have used a random forest to spectroscopically identify 533 M-giants in the satellites and halo of M31. These stars have passed rigorous membership criteria, ensuring that the sample is not significantly contaminated by M-dwarfs in the MW foreground. They have been separated into likely AGB stars, uncertain AGB stars, likely RGB stars, and uncertain RGB stars based on their absolute magnitudes. We have evaluated their spatial distribution, and various physical properties ($T_{\rm eff}$, dust and dynamics, metallicity, and differences between the AGB and RGB stars). Our major results can be summarized as follows

- We identify M-type AGB stars in 16 fields, including all three dEs, M32, two dSphs (And IX and And XVIII), and four fields containing debris from the GSS.

- We have computed C/M ratios seven fields, including three for which this is the first measurement. In M32 we find C/M= 0.14 ± 0.07, in the Northwest shelf we compute C/M= $0.25^{0.28}_{0.25}$, and in the Northeast shelf we find C/M= 0.38 ± 0.25. Using the calibration from Cioni (2009), these valeus correspond to [Fe/H]= -0.99 ± 0.15, [Fe/H]= -1.1 ± 0.24, and [Fe/H]= -1.2 ± 0.15, respectively.

- We find that M-type AGB stars have slightly later spectral types than M-type RGB stars, despite having statistically indistinguishable $T_{\rm eff}$ distributions. This suggests that M-type AGB stars are either intrinsically more metal-rich than their RGB counterparts, or preferentially located in metal-rich regions (e.g., the dEs of M31 rather than the dSphs).

- The M-giants in the satellites and halo of M31 appear to be largely dust-free and hydro-

static, consistent with our previous observations of carbon stars in the same fields.

- Calculations of the CaT in M-giants consistently returns lower ΣCa values and lower metallicities for AGB stars than for RGB stars in the same fields. As a result, AGB contamination can considerably decrease the average metallicity of a sample.

- PCA reveals that the spectra of the AGB and RGB M-giants in our sample are measurably different. In addition to AGB stars having deeper TiO features than their RGB counterparts, there are minute differences in shape and depth that do not correlate with observable properties.

Chapter 5

Conclusions and Future Directions

In this thesis, I have presented a sample of carbon and oxygen-rich AGB stars in the disk, satellites, and halo of M31. These stars were obtained by leveraging the full suite of photometric and spectroscopic observations from the SPLASH and PHAT surveys, including ground-based optical photometry, *HST* six-filter photometry, and over 34,0000 moderate resolution optical spectra. They represent the largest spectroscopically identified sample of AGB stars outside the MW.

In the disk of M31, I used high S/N MW templates and FBPS photometry to identify 103 carbon stars. Using three methods of identifying M-stars on the AGB, I computed the C/M ratio in spatial bins across the disk. I demonstrate that the precise definition of “M" changes the resulting C/M ratio, but does not effect the relationship between the C/M ratio and environmental properties. This confirms the need for homogenous samples when studying the C/M ratio as a function of other parameters. I have also demonstrated statistically significant correlations between the C/M ratio and galactocentric radius, present-day gas-phase [O/H], stellar [M/H], age,

and recent SFR. The relationship that I find between log(C/M) and [Fe/H] within M31 matches the relationship derived across the Local Group, despite significant differences in SFH.

In the satellites and halo of M31, I identify an additional 41 carbon stars which I characterize through a combination of color-color diagrams and the application of PCA. I show that, unlike the carbon stars observed in the MW, these stars are relatively unaffected by dust and dynamics, suggesting that their mass-loss is minimal. I also identify a significant population of carbon stars that are fainter than the TRGB, and bluer than expected. I show that these stars are likely a mix of intrinsic and extrinsic carbon stars. The fraction of faint carbon stars in a given field is highly dependent on the mass/metallicity of their host galaxy, which suggests that they form where low-metallicity enables more efficient carbon star formation via TDU, and higher binary fraction enables mass transfer onto a companion.

I pioneer a random forest approach to spectroscopically identifying M-giants in the satellites and halo of M31. I identify 533 M-giants, of which X are likely to be on the AGB. Using these stars, I compute the C/M ratios in several fields, and present the first C/M ratios in M32, and M31's Northeast and Northwest shelves. Like the carbon stars, I find these M-giants to be minimally affected by dust and dynamics, and thus minimally affected by mass loss. I also show that the CaT - [Fe/H] calibration derived for RGB stars returns systematically lower metallicities when applied to AGB stars, and calculate the change to mean [Fe/H] one can expect given different levels of AGB contamination. Finally, through application of PCA I show that the appearance of the TiO molecule that characterized M-giants is very complicated, and depends in a degenerate way on temperature, metallicity, and a host of properties we have yet to quantify.

5.1 Future directions: M31AGES

There is much work to be done studying AGB stars in M31 and its satellites, particularly in the context of AGB stars as tracers of intermediate age populations. AGB stars can be used to constrain the age distribution function of the M31 halo and provide insight into halo formation mechanisms. The M31 Asymptotic Giant Extended Survey (M31AGES; Beaton et al., in preparation) was created to leverage the power of NIR photometry to break the age-metallicity degeneracy and identify AGB stars in M31 in order to study the formation of the halo.

5.1.1 Motivation

ΛCDM predicts hierarchical galaxy formation: large galaxies are built out of smaller galaxies. In this paradigm, this growth begins with the small star-forming satellite galaxies that are bound to a more massive host. Over time these satellites begin to accrete, a process with several observable states. When a satellite first begins to fall into the halo of its host, it loses its gas through ram-pressure stripping (Grcevich and Putman, 2009). Next its spherical form begins to distort, forming bright, cold substructure (Kalirai *et al.*, 2006b; Gilbert *et al.*, 2009a; Fardal *et al.*, 2012). Over time, this substructure mixes, forming a smooth, virtualized halo.

Satellites have been observationally documented at all phases of accretion. We see star forming satellites that have not yet undergone ram-pressure stripping (Geha *et al.*, 2012), satellites that have been quenched but not yet tidally disrupted (Grcevich and Putman, 2009), satellites disrupted to a range of extents (McConnachie *et al.*, 2009; Martin and Jin, 2010;

Ibata *et al.*, 1994), and substructure on the verge of being well mixed (Gilbert *et al.*, 2006). The accretion process has also been documented by increasingly sophisticated N-body and hydrodynamical simulations.

Much of the observational research into galaxy formation by accretion has been done in the halo of M31. As discussed throughout this thesis, data from the SPLASH and Pan-Andromeda Archaeological (PAndAS, McConnachie *et al.*, 2009) surveys have been used to characterize the kinematics (e.g., Kalirai *et al.*, 2010; Tollerud *et al.*, 2012; Collins *et al.*, 2013) and metallicities (e.g., Ho *et al.*, 2015; Vargas *et al.*, 2014) of intact satellite galaxies, characterize prominent streams (e.g., Ibata *et al.*, 2001; Ferguson *et al.*, 2005; Ibata *et al.*, 2004; Guhathakurta *et al.*, 2005; Gilbert *et al.*, 2009b), detect faint substructure (e.g., Gilbert *et al.*, 2006, 2009a) and map the properties of the smooth halo (Gilbert *et al.*, 2012; Gilbert *et al.*, 2014). We are close to being able to paint a complete panoramic picture of evolution by accretion.

However, there are several open questions. It is difficult to distinguish between the ancient accretion of a massive progenitor and recent accretion of a smaller progenitor using surface brightness or kinematical arguments. As a result, the properties of the progenitors that caused presently observable substructure are largely unknown (with the exception perhaps of the giant southern stream Fardal *et al.*, 2006, 2007, 2012). Existing data is also insufficient to distinguish between halo stars “formed" by accretion, halo stars formed *in situ* and stars that have been kicked out of the disk (Dorman *et al.*, 2015).

These topics can be addressed with stellar ages. However, stellar age is a difficult parameter to estimate. One method is by comparing [α/Fe] and [Fe/H] measurements (Tins-

ley, 1979). While many [Fe/H] measurements have been made in M31 (McConnachie, 2012, and references therein), to date there have been very few measurements of alpha enhancement (Vargas *et al.*, 2014). It is simply difficult to obtain spectra of sufficient S/N at the distance of M31. An alternate method is to use isochrones. NIR (e.g. J and K_s) isochrones in particular break much of the age-metallicity degeneracy present in the optical, and allows for the distinction of intermediate-age (2-10 Gyr) TP-AGB stars and old ($>$ 10Gyr) RGB stars. It also can distinguish between carbon-rich TP-AGB stars and oxygen-rich TP-AGB stars (e.g., Battinelli *et al.*, 2007; Battinelli and Demers, 2009; Cioni, 2009; Held *et al.*, 2010; Jung *et al.*, 2012), whose proportions trace the metallicity and star formation history of their environment (e.g., Cioni *et al.*, 2008; Cioni, 2009; Hamren *et al.*, 2015).

5.1.2 Survey progress and next steps

M31AGES aims to capitalize on the power of NIR photometry to estimate stellar ages. The survey has used the NEWFIRM wide-field imager (Probst *et al.*, 2004) on the Kitt Peak 4m Mayall telescope to observe 61 M31 fields spanning the accreted, accreting, and yet-to-be-accreted populations. The positions of these fields are shown in Figure 5.1, and their general properties are listed in Table 5.1. Typcial fields consists of four blocks of J-band imaging (3840s) and six blocks of K_s imaging (5760s) (for full details of these observations we turn the reader upcoming survey papers).

The next stage of analysis is to identify AGB stars in the M31AGES survey area, an endeavor to which the clean samples of AGB stars presented in this thesis will be of great help. They can be used to verify the NIR-based classification of TP-AGB stars, which may be unre-

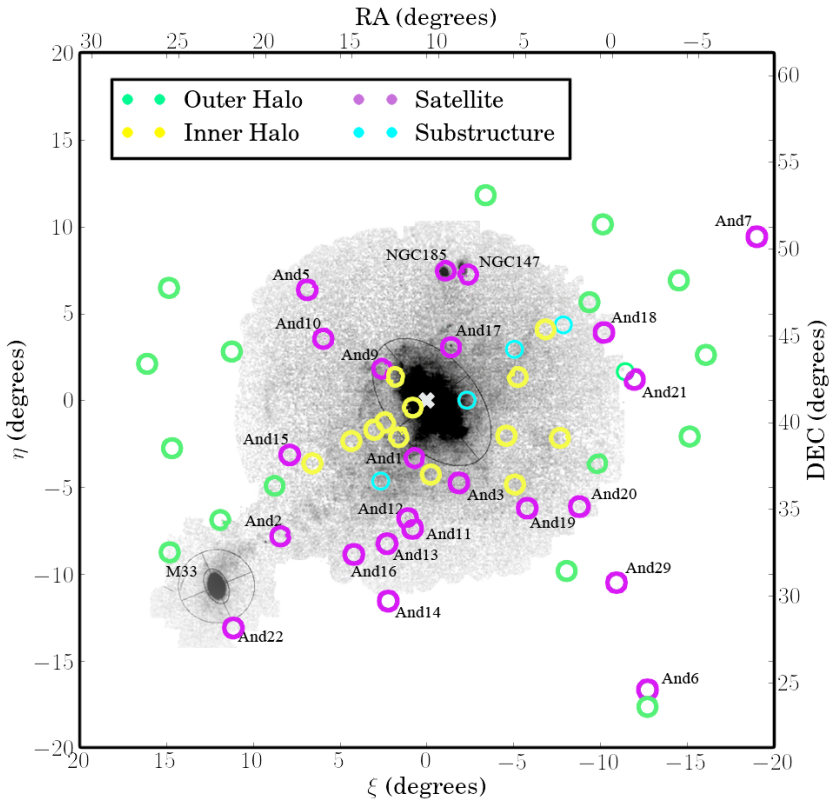

Figure 5.1: M31AGES Survey Map. NEWFIRM fields are overlaid to scale on a surface brightness map of M31 as colored circles, with yellow representing inner halo fields, green representing outer halo fields, turquoise representing known substructure, and purple representing satellite galaxies. M31 itself is marked with a white $\times$.

liable in certain cases (Menzies *et al.*, 2015). Figure 5.2 illustrates an example of this, with the carbon stars identified in Chapter 3 overlaid on preliminary M31AGES photometry. The majority of the carbon stars are consistent with the regions defined by Cioni (2009) and the 2.8 Gyr Padova isochrone (Bressan *et al.*, 2012). The extension of the carbon star sequence beyond the end of the isochrone is due to the treatment (or lack thereof) of dust in this particular isochrone sequence. Next, the properties estimated from the spectra either in this thesis or in future work (e.g., metallicity, [α/Fe]) can be compared to properties derived from the NIR photometry. This will provide an external source of information with which to calibrate photometry-based analysis.

The identification of AGB stars in the M31AGES survey area will enable several science goals. First, they will help determine the epoch of the last major star formation event in each field. This effectively age-dates the ram pressure stripping that marks the accretion of the (visible or progenitor) satellite onto the M31 halo. Next, we may be able to replicate the properties of the AGB populations in halo fields using a combination of AGB populations in satellite fields. This will allow us to roughly characterize the properties of the progenitor satellite. Finally, by comparing the AGB stars identified in the NIR to those identified in the optical and the MIR we will be able to precisely determine the fraction and properties of AGB stars visible/invisible at particular wavelengths. This will provide important information about dust production, and will allow future AGB surveys to correct their observed counts to represent the full AGB sample.

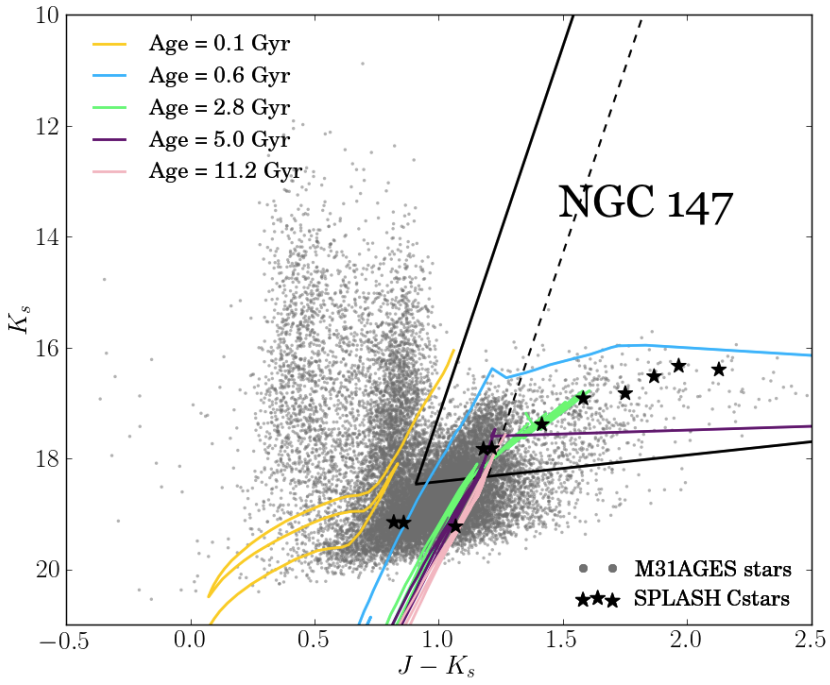

Figure 5.2: M31AGES photometry (grey) overlaid with SPLASH carbon stars (black), and Padova isochrones (colored by age). The regions delineating C- and M-stars from Cioni (2009) are marked as dashed lines.

Table 5.1: Properties of M31 Fields Targeted by M31AGES

Field	RA	DEC	Type	M_* ($10^6 M_\odot$)	$(m-M)_0$	d_{M31} degrees	kpc
a0	0:52:17	39:59:09	Inner Halo	...	...	2.219	30.33
a13	0:41:46	36:59:02	Inner Halo	...	...	4.289	58.6
a3	0:49:11	39:07:44	Inner Halo	...	...	2.468	33.73
And I	00:45:30.00	37:55:54.00	dSph	3.9	24.36	3.379	58.93
And X	01:06:33.70	44:48:15.80	dSph	0.096	24.23	5.605	109.42
And XI	00:45:58.32	33:52:35.00	dSph	0.049	24.4	7.42	102.61
And XII	00:47:05.17	34:26:58.99	dSph	0.031	24.7	6.873	132.46
And XIII	00:51:51.00	33:00:16.00	dSph	0.041	24.8	8.461	179.4
And XIV	00:51:35.00	29:41:49.00	dSph	0.2	24.33	11.71	162.05
And XV	01:14:18.70	38:07:03.00	dSph	0.49	25	6.839	173.59
And XVI	00:59:29.80	32:22:36.00	dSph	0.41	23.6	9.5	279.0
And XVII	00:37:07.00	44:19:20.00	dSph	0.26	24.5	3.223	45.69
And XVIII	00:01:48.97	45:09:50.00	dSph	0.63	25.66	8.403	114.73
And XIX	00:19:32.10	35:02:37.10	dSph	0.43	24.85	7.713	189.0
And II	01:16:28.30	33:25:42.00	dSph	7.6	24.07	10.305	183.39
And XX	00:07:30.70	35:07:56.50	dSph	0.029	24.52	9.24	129.07
And XXI	23:54:47.70	42:28:15.00	dSph	0.76	24.67	8.998	149.44
And XXII	01:27:40.0	28:05:25	dSph	0.034	24.5	16.062	220.59

Table 5.1 (cont'd): Properties of M31 Fields Targeted by M31AGES

Field	RA	DEC	Type	M_* ($10^6 M_\odot$)	$(m-M)_0$	d_{M31} degrees	kpc
And XXVII	0:37:27	45:23:13	dSph	0.12	24.59	4.229	74.53
And XXIX	23:58:55.6	30:45:20.0	dSph	0.18	24.32	13.725	188.12
And III	00:35:17.00	36:30:30.00	dSph	0.83	24.37	4.976	75.1
And V	01:10:17.00	47:37:46.00	dSph	0.39	24.44	8.032	109.43
And VI	23:58:48	24:35:42	dSph	2.8	24.47	19.015	258.67
And VII	23:26:33.50	50:41:30.00	dSph	9.5	24.41	16.169	218.27
And IX	00:53:00.00	43:05:00.00	dSph	0.15	24.42	2.628	39.38
GSS70	00:53:18.74	36:36:23.76	Substructure	...	...	5.095	69.6
GSS89	00:55:01.22	35:28:20.28	Substructure	...	...	6.275	85.71
H13d	00:50:04.55	42:36:36.00	Inner Halo	...	...	1.913	26.14
hst_stream	00:44:18.00	39:47:21.00	Substructure	...	...	1.509	20.62
m1	00:45:57.59	40:50:27.62	Inner Halo	...	...	0.743	10.15
m11	01:30:19.20	34:21:44.61	Outer Halo	...	...	11.644	158.85
m14	01:42:00.00	32:30:00.00	Outer Halo	...	...	14.707	200.43
M33	01:33:51.00	30:39:36.00	dSpiral	2900	24.54	14.784	206.44
m4	01:00:04.68	38:54:58.52	Inner Halo	...	...	4.065	55.54
m6	01:09:04.58	37:37:39.46	Inner Halo	...	...	6.251	85.38
m8	01:17:46.55	36:19:50.69	Outer Halo	...	...	8.418	114.94

Table 5.1 (cont'd): Properties of M31 Fields Targeted by M31AGES

Field	RA	DEC	Type	M_* ($10^6 M_\odot$)	$(m-M)_0$	d_{M31} degrees	kpc
NGC 147	00:33:12.1	48:30:32	dE	62	24.15	7.434	142.64
NGC 185	00:38:58.0	48:20:15	dE	68	23.95	7.1	186.99
Off AndVI	23:58:48	23:35:41	Outer Halo	...	...	19.918	270.83
R06A220	00:22:21.38	36:24:27.80	Inner Halo	...	...	6.273	85.68
R06A250	00:11:57.60	39:05:48.00	Inner Halo	...	...	6.264	85.57
R06A310	00:15:18.70	45:20:52.00	Inner Halo	...	...	6.441	87.97
R08A071	01:27:40.50	44:04:21.89	Outer Halo	...	...	8.714	118.98
R08A311	00:05:09.90	46:54:51.59	Outer Halo	...	...	8.786	119.96
R11A057.5	01:42:09.40	47:44:20.60	Outer Halo	...	...	12.383	168.89
R11A080	01:47:11.69	43:21:46.00	Outer Halo	...	...	12.078	164.75
R11A110	01:41:27.07	38:30:06.99	Outer Halo	...	...	11.582	158.01
R11A215	00:10:25.99	31:25:32.99	Outer Halo	...	...	11.786	160.78
R11A260	23:42:03.15	39:10:25.80	Outer Halo	...	...	11.756	160.38
R11A282.5	23:38:18.60	43:52:43.39	Outer Halo	...	...	12.124	165.38
R11A305	23:44:33.39	48:10:27.42	Outer Halo	...	...	12.398	169.1
R11A327.5	00:02:05.20	51:23:59.10	Outer Halo	...	...	12.299	167.75
R11A350	00:29:06.89	53:04:49.29	Outer Halo	...	...	12.033	164.14
R4A240	00:24:19.76	39:13:04.41	Inner Halo	...	...	4.067	55.57

Table 5.1 (cont'd): Properties of M31 Fields Targeted by M31AGES

Field	RA	DEC	Type	M_* ($10^6 M_\odot$)	$(m-M)_0$	d_{M31} degrees	kpc
R4A289	00:21:44.67	42:36:12.77	Inner Halo	...	...	4.125	56.36
R8A250	00:03:21.03	37:37:43.32	Outer Halo	...	...	8.423	115.01
R8A281	23:56:53.70	42:54:44.20	Outer Halo	...	...	8.655	118.17
SE35	00:54:47.75	39:34:09.40	Inner Halo	...	...	2.855	39.02
StrmE	00:22:27.94	44:11:54.50	Substructure	...	...	4.736	64.7
StrmF	00:11:11.90	45:36:31.70	Substructure	...	...	7.179	98.04
West	00:33:25.50	41:16:09.00	Inner Halo	...	...	1.75	23.92

Bibliography

Aaronson, M.; Gordon, G.; Mould, J.; Olszewski, E. and Suntzeff, N. The Extended Giant Branch of the Andromeda II Dwarf Spheroidal Galaxy. *The Astrophysical Journal* **296**, L7 (1985).

Aaronson, M.; Liebert, J. and Stocke, J. Discovery of carbon stars in the Draco dwarf spheroidal galaxy. *The Astrophysical Journal* **254**, 507 (1982).

Abia, C.; Boffin, H. M. J.; Isern, J. and Rebolo, R. Lithium abundances in a flux-limited sample of galactic carbon stars. *Astronomy & Astrophysics* **272**, 455 (1993).

Abia, C.; De Laverny, P. and Wahlin, R. Chemical analysis of carbon stars in the Local Group II. The Carina dwarf spheroidal galaxy. *Astronomy and Astrophysics* **481**, 161 (2008).

Abia, C.; Dominguez, I.; Gallino, R.; Busso, M.; Masera, S.; Straniero, O.; De Laverny, O.; Plez, B. and Isern, J. S -process nucleosynthesis in carbon stars. *The Astrophysical Journal* **579**, 817 (2002).

Abia, C. and Isern, J. ^{12}C/^{13}C ratios and Li abundances in C stars: evidence for deep mixing? *Monthly Notices of the Royal Astronomical Society* **289**, L11 (1997).

Abia, C. and Isern, J. The chemical composition of carbon stars. ii. the j-type stars■. *The Astrophysical Journal* **536**, 438 (2000).

Adelman-McCarthy, J. K.; Agüeros, M. A.; Allam, S. S.; Anderson, K. S. J.; Anderson, S. F.; Annis, J.; Bahcall, N. A.; Baldry, I. K.; Barentine, J. C.; Berlind, A.; Bernardi, M.; Blanton, M. R.; Boroski, W. N.; Brewington, H. J.; Brinchmann, J.; Brinkmann, J.; Brunner, R. J.; Budavári, T.; Carey, L. N.; Carr, M. A.; Castander, F. J.; Connolly, A. J.; Csabai, I.; Czarapata, P. C.; Dalcanton, J. J.; Doi, M.; Dong, F.; Eisenstein, D. J.; Evans, M. L.; Fan, X.; Finkbeiner, D. P.; Friedman, S. D.; Frieman, J. A.; Fukugita, M.; Gillespie, B.; Glazebrook, K.; Gray, J.; Grebel, E. K.; Gunn, J. E.; Gurbani, V. K.; de Haas, E.; Hall, P. B.; Harris, F. H.; Harvanek, M.; Hawley, S. L.; Hayes, J.; Hendry, J. S.; Hennessy, G. S.; Hindsley, R. B.; Hirata, C. M.; Hogan, C. J.; Hogg, D. W.; Holmgren, D. J.; Holtzman, J. A.; Ichikawa, S.-i.; Ivezić, Ž.; Jester, S.; Johnston, D. E.; Jorgensen, A. M.; Jurić, M.; Kent, S. M.; Kleinman, S. J.; Knapp, G. R.; Kniazev, A. Y.; Kron, R. G.; Krzesinski, J.; Kuropatkin, N.; Lamb, D. Q.; Lampeitl, H.; Lee, B. C.; Leger, R. F.; Lin, H.; Long, D. C.; Loveday, J.; Lupton, R. H.; Margon, B.; Martínez-Delgado, D.; Mandelbaum, R.; Matsubara, T.; McGehee, P. M.; McKay, T. A.; Meiksin, A.; Munn, J. A.; Nakajima, R.; Nash, T.; Neilsen, Jr., E. H.; Newberg, H. J.; Newman, P. R.; Nichol, R. C.; Nicinski, T.; Nieto-Santisteban, M.; Nitta, A.; O'Mullane, W.; Okamura, S.; Owen, R.; Padmanabhan, N.; Pauls, G.; Peoples, Jr., J.; Pier, J. R.; Pope, A. C.; Pourbaix, D.; Quinn, T. R.; Richards, G. T.; Richmond, M. W.; Rockosi, C. M.; Schlegel, D. J.; Schneider, D. P.; Schroeder, J.; Scranton, R.; Seljak, U.; Sheldon, E.; Shimasaku, K.; Smith, J. A.; Smolčić, V.; Snedden, S. A.; Stoughton, C.; Strauss, M. A.; SubbaRao, M.;

Szalay, A. S.; Szapudi, I.; Szkody, P.; Tegmark, M.; Thakar, A. R.; Tucker, D. L.; Uomoto, A.; Vanden Berk, D. E.; Vandenberg, J.; Vogeley, M. S.; Voges, W.; Vogt, N. P.; Walkowicz, L. M.; Weinberg, D. H.; West, A. A.; White, S. D. M.; Xu, Y.; Yanny, B.; Yocum, D. R.; York, D. G.; Zehavi, I.; Zibetti, S. and Zucker, D. B. The Fourth Data Release of the Sloan Digital Sky Survey. *The Astrophysical Journal Supplement Series* **162**, 38 (2006).

Albert, L.; Demers, S. and Kunkel, W. E. A carbon star survey of the local group dwarf galaxies. I. IC 1613. *The Astronomical Journal* **119**, 2780 (2000).

Aringer, B.; Girardi, L.; Nowotny, W.; Marigo, P. and Bressan, A. Synthetic photometry for M and K giants and stellar evolution: hydrostatic dust-free model atmospheres and chemical abundances. MNRAS **457**, 3611 (2016).

Aringer, B.; Girardi, L.; Nowotny, W.; Marigo, P. and Lederer, M. T. Synthetic photometry for carbon rich giants I . Hydrostatic dust-free models. *Astronomy & Astrophysics* **503**, 913 (2009).

Azzopardi, M.; Lequeux, J. and Westerlund, B. E. New carbon stars in spheroidal galaxies. I - Sculptor, Carina, Leo I and Leo II systems. A&A **144**, 388 (1985).

Azzopardi, M.; Lequeux, J. and Westerlund, B. E. New carbon stars in spheroidal galaxies. *Astronom & Astrophysics* **161**, 232 (1986).

Balick, B.; Kwitter, K. B.; Corradi, R. L. M. and Henry, R. B. C. Metal-rich Planetary Nebulae in the Outer Reaches of M31. *The Astrophysical Journal* **774**, 3 (2013).

Barmby, P.; Ashby, M. L. N.; Bianchi, L.; Engelbracht, C. W.; Gehrz, R. D.; Gordon, K. D.;

Hinz, J. L.; Huchra, J. P.; Humphreys, R. M.; Pahre, M. A.; Pérez-González, P. G.; Polomski, E. F.; Rieke, G. H.; Thilker, D. A.; Willner, S. P. and Woodward, C. E. Dusty Waves on a Starry Sea: The Mid-Infrared View of M31. *The Astrophysical Journal Letters* **650**, L45 (2006).

Battinelli, P. and Demers, S. A carbon star survey of the local group dwarf galaxies. ii. Pegasus, DDO 210, and Tucana. *The Astronomical Journal* **120**, 1801 (2000).

Battinelli, P. and Demers, S. Carbon star survey in the Local Group VIII . Probing the stellar halo of NGC 147. *Astronomy & Astrophysics* **418**, 33 (2004a).

Battinelli, P. and Demers, S. Carbon star survey of Local Group galaxies IX . The spheroidal galaxy NGC 185. *Astronomy & Astrophysics* **417**, 479 (2004b).

Battinelli, P. and Demers, S. Exploratory C star search in the disk of M 31 beyond 30 kpc. *Astronomy & Astrophysics* **430**, 905 (2005).

Battinelli, P. and Demers, S. Assessment of the near infrared identification of carbon stars II . The local group galaxies IC 1613 and NGC 3109. *Astronomy & Astrophysics* **493**, 1075 (2009).

Battinelli, P.; Demers, S. and Letarte, B. Carbon star survey in the Local Group. V. The outer disk of M31. *The Astronomical Journal* **125**, 1298 (2003).

Battinelli, P.; Demers, S. and Mannucci, F. The assessment of the near infrared identification of carbon stars. I. The Local Group galaxies WLM, IC 10 and NGC 6822. *Astronomy and Astrophysics* **474**, 35 (2007).

Beaton, R. L. *Life in the Outer Limits – Insight into Hierarchical Assembly from Stellar Halos in the Local Volume*. Ph.D. thesis, University of Virginia, USA (2014).

Bellazzini, M.; Ferraro, F. R.; Sollima, A.; Pancino, E. and Origlia, L. The calibration of the RGB Tip as a Standard Candle Extension to Near Infrared colors and higher metallicity. *Astronomy & Astrophysics* **424**, 199 (2004).

Bessell, M. S. and Brett, J. M. JHKLM photometry - Standard systems, passbands, and intrinsic colors. PASP **100**, 1134 (1988).

Blum, R. D.; Mould, J. R.; Olsen, K. A.; Frogel, J. A.; Werner, M.; Meixner, M.; Indebetouw, R.; Whitney, B.; Meade, M.; Babler, B.; Churchwell, E. B.; Gordon, K.; Engelbracht, C.; For, B.; Misselt, K.; Vijh, U.; Leitherer, C.; Volk, K.; Points, S.; Reach, W. and Hora, J. L. Spitzer SAGE survey of the Large Magellanic Cloud. II. Evolved stars and infrared color-magnitude diagrams. *The Astronomical Journal* **132**, 2034 (2006).

Blum, R. D.; Sellgren, K. and Depoy, D. L. Really Cool Stars at the Galactic Center. AJ **112**, 1988 (1996).

Boothroyd, A. I. and Sackmann, I. J. The production of low-mass stars. IV. Carbon stars. *The Astrophysical Journal* **328**, 671 (1988).

Boyer, M. L.; Girardi, L.; Marigo, P.; Williams, B. F.; Aringer, B.; Nowotny, W.; Rosenfield, P.; Dorman, C. E.; Guhathakurta, P.; Dalcanton, J. J.; Melbourne, J. L.; Olsen, K. a. G. and Weisz, D. R. Is There a Metallicity Ceiling To Form Carbon Stars? Novel Technique Reveals a Scarcity of C Stars in the Inner M31 Disk. *The Astrophysical Journal* **774**, 83 (2013).

Boyer, M. L.; McQuinn, K. B. W.; Barmby, P.; Bonanos, A. Z.; Gehrz, R. D.; Gordon, K. D.; Groenewegen, M. a. T.; Lagadec, E.; Lennon, D.; Marengo, M.; McDonald, I.; Meixner, M.; Skillman, E.; Sloan, G. C.; Sonneborn, G.; van Loon, J. T. and Zijlstra, A. An infrared census of dust in nearby galaxies with Spitzer (DUSTiNGS). II. Discovery of metal-poor dusty AGB stars. *The Astrophysical Journal* **800**, 51 (2015).

Boyer, M. L.; McQuinn, K. B. W.; Barmby, P.; Bonanos, A. Z.; Gehrz, R. D.; Gordon, K. D.; Groenewegen, M. a. T.; Lagadec, E.; Lennon, D.; Marengo, M.; Meixner, M.; Skillman, E.; Sloan, G. C.; Sonneborn, G.; van Loon, J. T. and Zijlstra, A. an Infrared Census of Dust in Nearby Galaxies With Spitzer (Dustings). I. Overview. *The Astrophysical Journal Supplement Series* **216**, 10 (2014).

Boyer, M. L.; Skillman, E. D.; van Loon, J. T.; Gehrz, R. D. and Woodward, C. E. A Spitzer Study of Asymptotic Giant Branch Stars. III. Dust Production and Gas Return in Local Group Dwarf Irregular Galaxies. *The Astrophysical Journal* **697**, 1993 (2009).

Boyer, M. L.; Srinivasan, S.; Riebel, D.; McDonald, I.; van Loon, J. T.; Clayton, G. C.; Gordon, K. D.; Meixner, M.; Sargent, B. A. and Sloan, G. C. The Dust Budget of the Small Magellanic Cloud: Are Asymptotic Giant Branch Stars the Primary Dust Source at Low Metallicity? *The Astrophysical Journal* **748**, 40 (2012).

Boyer, M. L.; Srinivasan, S.; van Loon, J. T.; McDonald, I.; Meixner, M.; Zaritsky, D.; Gordon, K. D.; Kemper, F.; Babler, B.; Block, M.; Bracker, S.; Engelbracht, C. W.; Hora, J.; Indebetouw, R.; Meade, M.; Misselt, K.; Robitaille, T.; SewiÅĆo, M.; Shiao, B.; Whitney, B. and SewiÅĆ, M. Surveying the agents of galaxy evolution in the tidally stripped, low metallicity

Small Magellanic Cloud (SAGE-SMC). II. Cool evolved stars. *The Astronomical Journal* **142**, 103 (2011).

Breiman, L. Random forests. *Machine learning* **45**, 5 (2001).

Bressan, A.; Marigo, P.; Girardi, L.; Salasnich, B.; Dal Cero, C.; Rubele, S. and Nanni, A. PARSEC : stellar tracks and isochrones with the PAdova and TRieste Stellar Evolution Code. *Monthly Notices of the Royal Astronomical Society* **427**, 127 (2012).

Brewer, J. P.; Richer, H. B. and Crabtree, D. R. Late-Type Stars in M31. I. Photometric Study of AGB Stars and Metallicity Gradients. *The Astronomical Journal* **109** (1995).

Brewer, J. P.; Richer, H. B. and Crabtree, D. R. Late-Type Stars In M31. II. C-, S- and M-Star Spectra. *The Astronomical Journal* **112** (1996).

Carrera, R.; Gallart, C.; Pancino, E. and Zinn, R. The infrared Ca II Triplet as metallicity indicator. *The Astrophysical Journal* **134**, 1298 (2007).

Carrera, R.; Pancino, E.; Gallart, C. and del Pino, A. The near-infrared Ca II triplet as a metallicity indicator - II. Extension to extremely metal-poor metallicity regimes. MNRAS **434**, 1681 (2013).

Chen, P. S. and Shan, H. G. Newly Identified Carbon Stars From Sources With Unusual IRAS Low-Resolution Spectra. *The Astronomical Journal* **144**, 10 (2012).

Chen, Y.; Trager, S.; Peletier, R.; Lancon, A.; Vazdekis, A.; Prugniel, P.; Silva, D. R. and Gonneau, A. The X-shooter Spectral Library (XSL): I. DR1. Near-ultraviolet through optical spectra from the first year of the survey. *Astronomy & Astrophysics* **565** (2014).

Cioni, M. L.; Girardi, L.; Marigo, P. and Habing, H. J. Astrophysics AGB stars in the Magellanic Clouds III . The rate of star formation across the Small Magellanic Cloud. *Astronomy & Astrophysics* **452**, 195 (2006).

Cioni, M.-R. L. The metallicity gradient as a tracer of history and structure: the Magellanic Clouds and M33 galaxies. *Astronomy and Astrophysics* **506**, 1137 (2009).

Cioni, M.-R. L. and Habing, H. J. AGB stars in the Magellanic Clouds. I. The C/M ratio. A&A **402**, 133 (2003).

Cioni, M.-R. L. and Habing, H. J. Near-IR observations of NGC 6822: AGB stars, distance, metallicity and structure. *Astronomy and Astrophysics* **429**, 837 (2005).

Cioni, M.-R. L.; Irwin, M.; Ferguson, A. M. N.; Mcconnachie, A.; Conn, B. C.; Huxor, A.; Ibata, R.; Lewis, G. and Tanvir, N. AGB stars as tracers of metallicity and mean age across M33. *Astronomy & Astrophysics* **487**, 131 (2008).

Coelho, P.; Mendes de Oliveira, C. and Cid Fernandes, R. An analysis of the composite stellar population in M32. MNRAS **396**, 624 (2009).

Cole, A.; Smecker-Hane, T. and Gallagher III, J. The Metallicity Distribution Function of Red Giants in the Large Magellanic Cloud. *Aj* **120**, 1808 (2000).

Cole, A. A.; Smecker-Hane, T. A.; Tolstoy, E.; Bosler, T. L. and Gallagher, J. S. The effects of age on red giant metallicities derived from the near-infrared Ca II triplet. *Monthly Notices of the Royal Astronomical Society* **347**, 367 (2004).

Collins, M. L. M.; Chapman, S. C.; Irwin, M. J.; Martin, N. F.; Ibata, R. A.; Zucker, D. B.; Blain, A.; Ferguson, A. M. N.; Lewis, G. F.; McConnachie, A. W. and Peñarrubia, J. A Keck/DEIMOS spectroscopic survey of the faint M31 satellites AndĂČIX, AndĂČXI, AndĂČXII and AndĂČXIII. *Monthly Notices of the Royal Astronomical Society* **407**, 2411 (2010).

Collins, M. L. M.; Chapman, S. C.; Rich, R. M.; Ibata, R. A.; Martin, N. F.; Irwin, M. J.; Bate, N. F.; Lewis, G. F.; Peñarrubia, J.; Arimoto, N.; Casey, C. M.; Ferguson, A. M. N.; Koch, A.; McConnachie, A. W. and Tanvir, N. A Kinematic Study of the Andromeda Dwarf Spheroidal System. *The Astrophysical Journal* **768**, 172 (2013).

Connolly, A. J.; Szalay, A. S.; Bershady, M. A.; Kinney, A. L. and Calzetti, D. Spectral classification of galaxies: an orthogonal approach. *The Astronomical Journal* **110**, 1071 (1995).

Conroy, C. Modeling the Panchromatic Spectral Energy Distributions of Galaxies. *Annual Review of Astronomy and Astrophysics* pp. 1–66 (2013).

Cook, K. H.; Aaronson, M. and Norris, J. Carbon and M stars in nearby galaxies - A preliminary survey using a photometric technique. *The Astrophysical Journal* **305**, 634 (1986).

Cooper, M. C.; Newman, J. A.; Davis, M.; Finkbeiner, D. P. and Gerke, B. F. spec2d: DEEP2 DEIMOS Spectral Pipeline. Astrophysics Source Code Library (2012).

Da Costa, G. S. New Results for Local Group Dwarf Galaxies. In Meylan, G. and Prugniel, P., eds., *European Southern Observatory Conference and Workshop Proceedings* (1994), vol. 49 of *European Southern Observatory Conference and Workshop Proceedings*, p. 221.

Dalcanton, J. J.; Fouesneau, M.; Hogg, D. W.; Lang, D.; Leroy, A. K.; Gordon, K. D.; Sandstrom, K.; Weisz, D. R.; Williams, B. F.; Bell, E. F.; Dong, H.; Gilbert, K. M.; Gouliermis, D. A.; Guhathakurta, P.; Lauer, T. R.; Schruba, A.; Seth, A. C. and Skillman, E. D. The Panchromatic Hubble Andromeda Treasury. VIII. A Wide-area, High-resolution Map of Dust Extinction in M31. *The Astrophysical Journal* **814**, 3 (2015).

Dalcanton, J. J.; Williams, B. F.; Lang, D.; Lauer, T. R.; Kalirai, J. S.; Seth, A. C.; Dolphin, A.; Rosenfield, P.; Weisz, D. R.; Bell, E. F.; Bianchi, L. C.; Boyer, M. L.; Caldwell, N.; Dong, H.; Dorman, C. E.; Gilbert, K. M.; Girardi, L.; Gogarten, S. M.; Gordon, K. D.; Guhathakurta, P.; Hodge, P. W.; Holtzman, J. a.; Johnson, L. C.; Larsen, S. S.; Lewis, A.; Melbourne, J. L.; Olsen, K. a. G.; Rix, H.-W.; Rosema, K.; Saha, A.; Sarajedini, A.; Skillman, E. D. and Stanek, K. Z. The Panchromatic Hubble Andromeda Treasury. *The Astrophysical Journal Supplement Series* **200** (2012).

Davidge, T. J. The brightest asymptotic giant branch stars in the inner bulge of M31. *The Astronomical Journal* **122**, 1386 (2001).

Davidge, T. J. The evolved stellar content of NGC 147 , NGC 185 , AND NGC 205. *The Astronomical Journal* **130**, 2087 (2005).

Davidge, T. J. Seeing Red in M32: Constraints on the Stellar Content From Near- and Mid-Infrared Observations and Applications for Studies of More Distant Galaxies. *The Astrophysical Journal* **791**, 66 (2014).

de Kool, M. and Green, P. J. A Model for the Space Density of Dwarf Carbon Stars. *The Astrophysical Journal* **449**, 236 (1995).

Demers, S. and Battinelli, P. C Star Survey of Local Group Dwarf Galaxies. III. The Sagittarius Dwarf Irregular and the Leo I Dwarf Spheroidal Galaxies. *The Astronomical Journal* **123**, 238 (2002).

Demers, S. and Battinelli, P. C stars as kinematic probes of the Milky Way disk from 9 to 15 kpc. A&A **473**, 143 (2007).

Demers, S.; Battinelli, P. and Letarte, B. Carbon star survey in the Local Group. VI. The dwarf spheroidal galaxy NGC 205. *The Astronomical Journal* **125**, 3037 (2003).

Dolphin, A. E. Numerical methods of star formation history measurement and applications of seven dwarf spheroidals. *Monthly Notices of the Royal Astronomical Society* **332**, 91 (2002).

Dominguez, I.; Abia, C.; Straniero, O.; Cristallo, S. and Pavlenko, Y. V. First detection of a lithium rich carbon star in the Draco dwarf galaxy: evidence for a young stellar population. *Astronomy & Astrophysics* **422**, 10 (2004).

Dorman, C. E.; Guhathakurta, P.; Fardal, M. a.; Lang, D.; Geha, M. C.; Howley, K. M.; Kalirai, J. S.; Bullock, J. S.; Cuillandre, J.-C.; Dalcanton, J. J.; Gilbert, K. M.; Seth, A. C.; Tollerud, E. J.; Williams, B. F. and Yniguez, B. The SPLASH survey: Kinematics of Andromeda's inner spheroid. *The Astrophysical Journal* **752**, 147 (2012).

Dorman, C. E.; Guhathakurta, P.; Seth, A. C.; Weisz, D. R.; Bell, E. F.; Dalcanton, J. J.; Gilbert, K. M.; Hamren, K. M.; Lewis, A. R.; Skillman, E. D.; Toloba, E. and Williams, B. F. A

Clear Age-Velocity Dispersion Correlation in Andromeda's Stellar Disk. *The Astrophysical Journal* **803**, 24 (2015).

Dorman, C. E.; Widrow, L. M.; Guhathakurta, P.; Seth, A. C.; Foreman-Mackey, D.; Bell, E. F.; Dalcanton, J. J.; Gilbert, K. M.; Skillman, E. D. and Williams, B. F. A New Approach To Detailed Structural Decomposition From the Splash and Phat Surveys: Kicked-Up Disk Stars in the Andromeda Galaxy? *The Astrophysical Journal* **779**, 103 (2013).

Dyck, H. M.; Benson, J. A.; van Belle, G. T. and Ridgway, S. T. Radii and Effective Temperatures for K and M Giants and Supergiants. AJ **111**, 1705 (1996).

Dyck, H. M.; van Belle, G. T. and Thompson, R. R. Radii and Effective Temperatures for K and M Giants and Supergiants. II. AJ **116**, 981 (1998).

Faber, S. M.; Phillips, A. C.; Kibrick, R. I.; Alcott, B.; Allen, S. L.; Burrous, J.; Cantrall, T.; Clarke, D.; Coil, A. L.; Cowley, D. J.; Davis, M.; Deich, W. T. S.; Dietsch, K.; Gilmore, D. K.; Harper, C. A.; Hilyard, D. F.; Lewis, J. P.; McVeigh, M.; Newman, J.; Osborne, J.; Schiavon, R.; Stover, R. J.; Tucker, D.; Wallace, V.; Wei, M.; Wirth, G. and Wright, C. A. The DEIMOS spectrograph for the Keck II Telescope: integration and testing. In Iye, M. and Moorwood, A. F. M., eds., *Instrument Design and Performance for Optical/Infrared Ground-based Telescopes* (2003), vol. 4841 of Proc. SPIE, pp. 1657–1669.

Fardal, M. a.; Babul, a.; Geehan, J. J. and Guhathakurta, P. Investigating the Andromeda stream - II. Orbital fits and properties of the progenitor. *Monthly Notices of the Royal Astronomical Society* **1028**, 060120032526019 (2006).

Fardal, M. a.; Guhathakurta, P.; Babul, a. and McConnachie, a. W. Investigating the Andromeda stream - III. A young shell system in M31. *Monthly Notices of the Royal Astronomical Society* **380**, 15 (2007).

Fardal, M. a.; Guhathakurta, P.; Gilbert, K. M.; Tollerud, E. J.; Kalirai, J. S.; Tanaka, M.; Beaton, R.; Chiba, M.; Komiyama, Y. and Iye, M. A spectroscopic survey of Andromeda'ĂŹs Western Shelf. *Monthly Notices of the Royal Astronomical Society* **423**, 3134 (2012).

Fazio, G. G.; Hora, J. L.; Allen, L. E.; Ashby, M. L. N.; Barmby, P.; Deutsch, L. K.; Huang, J.-S.; Kleiner, S.; Marengo, M.; Megeath, S. T.; Melnick, G. J.; Pahre, M. A.; Patten, B. M.; Polizotti, J.; Smith, H. A.; Taylor, R. S.; Wang, Z.; Willner, S. P.; Hoffmann, W. F.; Pipher, J. L.; Forrest, W. J.; McMurty, C. W.; McCreight, C. R.; McKelvey, M. E.; McMurray, R. E.; Koch, D. G.; Moseley, S. H.; Arendt, R. G.; Mentzell, J. E.; Marx, C. T.; Losch, P.; Mayman, P.; Eichhorn, W.; Krebs, D.; Jhabvala, M.; Gezari, D. Y.; Fixsen, D. J.; Flores, J.; Shakoorzadeh, K.; Jungo, R.; Hakun, C.; Workman, L.; Karpati, G.; Kichak, R.; Whitley, R.; Mann, S.; Tollestrup, E. V.; Eisenhardt, P.; Stern, D.; Gorjian, V.; Bhattacharya, B.; Carey, S.; Nelson, B. O.; Glaccum, W. J.; Lacy, M.; Lowrance, P. J.; Laine, S.; Reach, W. T.; Stauffer, J. A.; Surace, J. A.; Wilson, G.; Wright, E. L.; Hoffman, A.; Domingo, G. and Cohen, M. The Infrared Array Camera (IRAC) for the Spitzer Space Telescope. *The Astrophysical Journal Supplement Series* **154**, 10 (2004).

Feast, M. W.; Abedigamba, O. P. and Whitelock, P. a. Is there a metallicity gradient in the Large Magellanic Cloud? *Monthly Notices of the Royal Astronomical Society: Letters* **408**, L76 (2010).

Ferguson, A. M. N.; Johnson, R. A.; Faria, D. C.; Irwin, M. J.; Ibata, R. A.; Johnston, K. V.; Lewis, G. F. and Tanvir, N. R. The Stellar Populations of the M31 Halo Substructure. *The Astrophysical Journal Letters* **622**, L109 (2005).

Ferraro, F. R.; Messineo, M.; Fusi Pecci, F.; De Palo, M. A.; Straniero, O.; Chieffi, A. and Limongi, M. The giant, horizontal, and asymptotic branches of galactic globular clusters. *The Astronomical Journal* **118**, 1738 (1999).

Fluks, M. A.; Plez, B.; The, P. S.; de Winter, D.; Westerlund, B. and Steenman, H. C. On the spectra and photometry of M-giant stars. *Astronomy and Astrophysics Supplement Series* **105**, 311 (1994).

Frantsman, J. Faint carbon stars from the evolution of close binaries. *Astronomy and Astrophysics* **514**, 511 (1997).

Freedman, W. and Madore, B. F. An Empirical Test for the Metallicity Sensitivity of the Cepheid Period-Luminosity Relation. *The Astrophysical Journal* **365**, 186 (1990).

Frogel, J. A.; Mould, J. and Blanco, V. M. The asymptotic giant branch of Magellanic Cloud clusters. *The Astrophysical Journal* **352**, 96 (1990).

Geha, M.; Blanton, M. R.; Yan, R. and Tinker, J. L. A Stellar Mass Threshold for Quenching of Field Galaxies. *The Astrophysical Journal* **757**, 85 (2012).

Geha, M.; Guhathakurta, P.; Rich, R. M. and Cooper, M. C. Local Group Dwarf Elliptical Galaxies. I. Mapping the Dynamics of NGC 205 Beyond the Tidal Radius. *The Astronomical Journal* **131**, 332 (2006).

Geha, M.; van der Marel, R. P.; Guhathakurta, P.; Gilbert, K. M.; Kalirai, J. and Kirby, E. N. Local Group Dwarf Elliptical Galaxies. Ii. Stellar Kinematics To Large Radii in NGC 147 and NGC 185. *The Astrophysical Journal* **711**, 361 (2010).

Geha, M.; Weisz, D.; Grocholski, A.; Dolphin, A.; van der Marel, R. P. and Guhathakurta, P. HST/ACS Direct Ages of the Dwarf Elliptical Galaxies NGC 147 and NGC 185. *The Astrophysical Journal* **811**, 114 (2015).

Gehrz, R. Sources of Stardust in the Galaxy. In Allamandola, L. J. and Tielens, A. G. G. M., eds., *Interstellar Dust* (1989), vol. 135 of *IAU Symposium*, p. 445.

Gilbert, K. M.; Fardal, M.; Kalirai, J. S.; Guhathakurta, P.; Geha, M. C.; Isler, J.; Majewski, S. R.; Ostheimer, J. C.; Patterson, R. J.; Reitzel, D. B.; Kirby, E.; Cooper, M. C. and Al, G. E. T. Stellar kinematics in the complicated inner spheroid of M31 : Discovery of substructure along the southeastern minor axis and its relationship to the giant southern stream. *The Astrophysical Journal* **668**, 245 (2007).

Gilbert, K. M.; Font, A. S.; Johnston, K. V. and Guhathakurta, P. The dominance of metal-rich streams in stellar halos : A comparison between substructure in M31 and Λ CDM models. *The Astrophysical Journal* **701**, 776 (2009a).

Gilbert, K. M.; Guhathakurta, P.; Beaton, R. L.; Bullock, J.; Geha, M. C.; Kalirai, J. S.; Kirby, E. N.; , S. R.; Ostheimer, J. C.; Patterson, R. J.; Tollerud, E. J.; Tanaka, M. and Chiba, M. Global Properties of M31'S Stellar Halo From the Splash Survey. I. Surface Brightness Profile. *The Astrophysical Journal* **760**, 76 (2012).

Gilbert, K. M.; Guhathakurta, P.; Kalirai, J. S.; Rich, R. M.; Majewski, S. R.; Ostheimer, J. C.; Reitzel, D. B.; Cenarro, a. J.; Cooper, M. C.; Luine, C. and Patterson, R. J. A New Method for Isolating M31 Red Giant Stars: The Discovery of Stars out to a Radial Distance of 165 kpc. *The Astrophysical Journal* **652**, 1188 (2006).

Gilbert, K. M.; Guhathakurta, P.; Kollipara, P.; Beaton, R. L.; Geha, M. C.; Kalirai, J. S.; Kirby, E. N.; Majewski, S. R. and Patterson, R. J. The Splash Survey: a Spectroscopic Portrait of Andromeda'Źs Giant Southern Stream. *The Astrophysical Journal* **705**, 1275 (2009b).

Gilbert, K. M.; Kalirai, J. S.; Guhathakurta, P.; Beaton, R. L.; Geha, M. C.; Kirby, E. N.; Majewski, S. R.; Patterson, R. J.; Tollerud, E. J.; Bullock, J. S.; Tanaka, M. and Chiba, M. Global Properties of M31's Stellar Halo from the SPLASH Survey. II. Metallicity Profile. *The Astrophysical Journal* **796**, 76 (2014).

Girardi, L.; Marigo, P.; Bressan, A. and Rosenfield, P. The Insidious Boosting of Thermally Pulsing Asymptotic Giant Branch Stars in Intermediate-Age Magellanic Cloud Clusters. *The Astrophysical Journal* **777**, 142 (2013).

Girardi, L.; Williams, B. F.; Gilbert, K. M.; Rosenfield, P.; Dalcanton, J. J.; Marigo, P.; Boyer, M. L.; Dolphin, A.; Weisz, D. R.; Melbourne, J.; Olsen, K. a. G.; Seth, A. C. and Skillman, E. The ACS Nearby Galaxy Survey Treasury. IX. Constraining Asymptotic Giant Branch Evolution With Old Metal-Poor Galaxies. *The Astrophysical Journal* **724**, 1030 (2010).

Grcevich, J. and Putman, M. E. H I in Local Group Dwarf Galaxies and Stripping By the Galactic Halo. *The Astrophysical Journal* **696**, 385 (2009).

Grebel, E. K. Star Formation Histories as Probed by AGB Stars. In Kerschbaum, F.; Charbonnel, C. and Wing, R. F., eds., *Why Galaxies Care About AGB Stars: Their Importance as Actors and Probes* (2007), vol. 378 of *Astronomical Society of the Pacific Conference Series*, p. 375.

Green, P. Innocent Bystanders: Carbon Stars From the Sloan Digital Sky Survey. *The Astrophysical Journal* **765**, 12 (2013).

Gregersen, D.; Seth, A. C.; Williams, B. F.; Lang, D.; Dalcanton, J. J.; Girardi, L.; Skillman, E. D.; Bell, E.; Dolphin, A. E.; Fouesneau, M.; Guhathakurta, P.; Hamren, K. M.; Johnson, L. C.; Kalirai, J.; Lewis, A. R.; Monachesi, A. and Olsen, K. Panchromatic Hubble Andromeda Treasury. XII. Mapping Stellar Metallicity Distributions in M31. AJ **150**, 189 (2015).

Grillmair, C. J.; Lauer, T. R.; Worthey, G.; Faber, S. M.; Freedman, W. L.; Madore, B. F.; Ajhar, E. A.; Baum, W. A.; Holtzman, J. A.; Lynds, C. R.; O'Neil, Jr., E. J. and Stetson, P. B. Hubble Space Telescope Observations of M32: The Color-Magnitude Diagram. AJ **112**, 1975 (1996).

Groenewegen, M. A. T. The mid- and far-infrared colours of AGB and post-AGB stars. A&A **448**, 181 (2006).

Guhathakurta, P.; Ostheimer, J. C.; Gilbert, K. M.; Rich, R. M.; Majewski, S. R.; Kalirai, J. S.; Reitzel, D. B.; Cooper, M. C. and Patterson, R. J. Discovery of an extended halo of metal-poor stars in the Andromeda spiral galaxy (2005).

Guhathakurta, P.; Rich, R. M.; Reitzel, D. B.; Cooper, M. C.; Gilbert, K. M.; Majewski, S. R.; Ostheimer, J. C.; Geha, M. C.; Johnston, K. V. and Patterson, R. J. Dynamics and stellar content of the Giant Southern Stream in M31. I. Keck spectroscopy of red giant stars. *The Astronomical Journal* **131**, 2497 (2006).

Hamren, K. M.; Rockosi, C. M.; Guhathakurta, P.; Boyer, M. L.; Smith, G. H.; Dalcanton, J. J.; Gregersen, D.; Seth, A. C.; Lewis, A. R.; Williams, B. F.; Toloba, E.; Girardi, L.; Dorman, C. E.; Gilbert, K. M. and Weisz, D. R. a Spectroscopic and Photometric Exploration of the C/M Ratio in the Disk of M31. *The Astrophysical Journal* **810**, 60 (2015).

Harbeck, D.; Gallagher, J. S.; Grebel, E. K.; Koch, A. and Zucker, D. B. Andromeda IX : Properties of the faintest M31 dwarf satellite galaxy. *The Astrophysical Journal* **623**, 159 (2005).

Harbeck, D.; Gallagher III, J. S. and Grebel, E. K. WIYN Survey for Carbon Stars in the M31 and Cetus Dwarf Spheroidal Galaxies: Evolutionary Implications. *The Astronomical Journal* **127**, 2711 (2004).

Held, E. V.; Gullieuszik, M.; Rizzi, L.; Girardi, L.; Marigo, P. and Saviane, I. A near-infrared study of AGB and red giant stars in the Leo I dSph galaxy. *Monthly Notices of the Royal Astronomical Society* **1489**, 1475 (2010).

Ho, N.; Geha, M.; Munoz, R. R.; Guhathakurta, P.; Kalirai, J.; Gilbert, K. M.; Tollerud, E.; Bullock, J.; Beaton, R. L. and Majewski, S. R. Stellar Kinematics of the Andromeda Ii Dwarf Spheroidal Galaxy. *The Astrophysical Journal* **758**, 124 (2012).

Ho, N.; Geha, M.; Tollerud, E. J.; Zinn, R.; Guhathakurta, P. and Vargas, L. C. Metallicity evolution of the six most luminous m31 dwarf satellites. *The Astrophysical Journal* **798** (2015).

Howley, K. M.; Guhathakurta, P.; van der Marel, R.; Geha, M.; Kalirai, J.; Yniguez, B.; Kirby, E.; Cuillandre, J.-C. and Gilbert, K. Internal Stellar Kinematics of M32 From the Splash Survey: Dark Halo Constraints. *The Astrophysical Journal* **765**, 65 (2013).

Huxor, A. P. and Grebel, E. K. Tracing the tidal streams of the Sagittarius dSph, and halo Milky Way features, with carbon-rich long-period variables. MNRAS **453**, 2653 (2015).

Ibata, R.; Chapman, S.; Ferguson, A. M. N.; Irwin, M.; Lewis, G. and McConnachie, A. Taking measure of the Andromeda halo: a kinematic analysis of the giant stream surrounding M31. MNRAS **351**, 117 (2004).

Ibata, R.; Irwin, M.; Lewis, G. F. and Stolte, A. Galactic Halo Substructure in the Sloan Digital Sky Survey: The Ancient Tidal Stream from the Sagittarius Dwarf Galaxy. *The Astrophysical Journal Letters* **547**, L133 (2001).

Ibata, R. A.; Gilmore, G. and Irwin, M. J. A dwarf satellite galaxy in Sagittarius. Nature **370**, 194 (1994).

Izzard, R. G. and Tout, C. a. A binary origin for low-luminosity carbon stars. *Monthly Notices of the Royal Astronomical Society* **350**, L1 (2004).

Jones, O. C.; McDonald, I.; Rich, R. M.; Kemper, F.; Boyer, M. L.; Zijlstra, A. A. and Bendo,

G. J. A Spitzer Space Telescope survey of extreme asymptotic giant branch stars in M32. MNRAS **446**, 1584 (2015).

Jorgensen, U. G.; Carlsson, M. and Johnson, H. R. The calcium infrared triplet lines in stellar spectra. *Astronomy & Astrophysics* **254**, 258 (1992).

Jung, M. Y.; Ko, J.; Kim, J.-w.; Chun, S.-h.; Kim, H.-i. and Sohn, Y. Near-infrared properties of asymptotic giant branch stars in nearby dwarf elliptical Galaxy NGC 205ŃĘ. *Astronomy & Astrophysics* **543** (2012).

Kalirai, J. S.; Beaton, R. L.; Geha, M. C.; Gilbert, K. M.; Guhathakurta, P.; Kirby, E. N.; Majewski, S. R.; Ostheimer, J. C.; Patterson, R. J. and Wolf, J. The Splash Survey: Internal Kinematics, Chemical Abundances, and Masses of the Andromeda I, II, III, VII, X, and XIV Dwarf Spheroidal Galaxies ,. *The Astrophysical Journal* **711**, 671 (2010).

Kalirai, J. S.; Gilbert, K. M.; Guhathakurta, P.; Majewski, S. R.; Ostheimer, J. C.; Rich, R. M.; Cooper, M. C.; Reitzel, D. B. and Patterson, R. J. The Metal-poor Halo of the Andromeda Spiral Galaxy (M31). *The Astrophysical Journal* **648**, 389 (2006a).

Kalirai, J. S.; Guhathakurta, P.; Gilbert, K. M.; Reitzel, D. B.; Majewski, S. R.; Rich, R. M. and Cooper, M. C. Kinematics and Metallicity of M31 Red Giants: The Giant Southern Stream and Discovery of a Second Cold Component at RL'=20 kpc. *The Astrophysical Journal* **641**, 268 (2006b).

Kalirai, J. S.; Marigo, P. and Tremblay, P.-E. The Core Mass Growth and Stellar Lifetime

of Thermally Pulsing Asymptotic Giant Branch Stars. *The Astrophysical Journal* **782**, 17 (2014).

Kalirai, J. S.; Zucker, D. B.; Guhathakurta, P.; Geha, M.; Kniazev, A. Y.; Martínez-Delgado, D.; Bell, E. F.; Grebel, E. K. and Gilbert, K. M. THE SPLASH SURVEY: A SPECTROSCOPIC ANALYSIS OF THE METAL-POOR, LOW-LUMINOSITY M31 dSph SATELLITE ANDROMEDA X,. *The Astrophysical Journal* **705**, 1043 (2009).

Karakas, A. Helium enrichment and Carbon-star Production in Metal-rich Populations. *Monthly Notices of the Royal Astronomical Society* **000** (2014).

Karakas, A. I.; Lattanzio, J. C. and Pols, O. R. Parameterising the Third Dredge-up in Asymptotic Giant Branch Stars. *Publications of the Astronomical Society of Australia* **19**, 515 (2002).

Keenan, P. C. and Morgan, W. W. The Classification of the Red Carbon Stars. *The Astrophysical Journal* **94**, 501 (1941).

Kerschbaum, F.; Nowotny, W.; Olofsson, H. and Schwarz, H. E. A census of AGB stars in Local Group galaxies III . The dwarf spheroidal And II. *Astronomy & Astrophysics* **619**, 613 (2004).

Kewley, L. J. and Dopita, M. A. Using strong lines to estimate abundances in extragalactic HII regions. *The Astrophysical Journal Supplement Series* **142**, 35 (2002).

Koch, A. and Rich, R. M. A Statistical Analysis of the Late-Type Stellar Content in the Andromeda Halo. *The Astronomical Journal* **139**, 2279 (2010).

Kontizas, E.; Dapergolas, A.; Morgan, D. H. and Kontizas, M. A Catalogue of carbon stars in the LMC. *Astronomy & Astrophysics* **369**, 932 (2001).

Kwitter, K. B.; Lehman, E. M. M.; Balick, B. and Henry, R. B. C. Abundances of Planetary Nebulae in the Outer Disk of M31. *The Astrophysical Journal* **753**, 12 (2012).

Lanï£¡on, a. and Wood, P. R. A library of 0.5 to 2.5 micron spectra of luminous cool stars. *Astronomy and Astrophysics Supplement Series* **146**, 217 (2000).

Lebzelter, T.; Lederer, M. T.; Cristallo, S.; Hinkle, K. H.; Straniero, O. and Aringer, B. AGB stars of the intermediate-age LMC cluster NGC 1846 II . Dredge up along the AGB. *Astronomy & Astrophysics* **486**, 511 (2008).

Letarte, B.; Demers, S.; Battinelli, P. and Kunkel, W. E. The Extent of NGC 6822 Revealed by Its C Star Population. *The Astronomical Journal* **123**, 832 (2002).

Lewis, A. R.; Dolphin, A. E.; Dalcanton, J. J.; Weisz, D. R.; Williams, B. F.; Bell, E. F.; Seth, A. C.; Simones, J. E.; Skillman, E. D.; Choi, Y.; Fouesneau, M.; Guhathakurta, P.; Johnson, L. C.; Kalirai, J. S.; Leroy, A. K.; Monachesi, A.; Rix, H.-W. and Schruba, A. The Panchromatic Hubble Andromeda Treasury. XI. The Spatially Resolved Recent Star Formation History of M31. *The Astrophysical Journal* **805**, 183 (2015).

Lianou, S.; Grebel, E. K. and Koch, A. Spectroscopic versus Photometric Metallicities: Milky Way Dwarf Spheroidal Companions as a Test Case. *Astronomy & Astrophysics* **152**, 17 (2011).

Loidl, R. and Lan, A. Spectra of carbon-rich asymptotic giant branch stars between 0.5 and 2.5μm : Theory meets observation. *Astronomy & Astrophysics* **371**, 1065 (2001).

Mager, V. A.; Madore, B. F. and Freedman, W. L. Metallicity-corrected Tip of the Red Giant Branch Distance to NGC 4258. *The Astrophysical Journal* **689**, 721 (2008).

Majewski, S. R.; Beaton, R. L.; Patterson, R. J.; Kalirai, J. S.; Geha, M. C.; Mun, R. R.; Seigar, M. S.; Guhathakurta, P.; Gilbert, K. M.; Rich, R. M.; Bullock, J. S. and Reitzel, D. B. Discovery of Andromeda XIV: A Dwarf Spheroidal Dynamical Rogue in the Local Group. *The Astrophysical Journal* **670**, 9 (2007).

Majewski, S. R.; Ostheimer, J. C.; Kunkel, W. E. and Patterson, R. J. Exploring Halo Substructure with Giant Stars. I. Survey Description and Calibration of the Photometric Search Technique. *The Astronomical Journal* **120**, 2550 (2000).

Majewski, S. R.; Skrutskie, M. F.; Weinberg, M. D. and Ostheimer, J. C. A Two Micron All Sky Survey View of the Sagittarius Dwarf Galaxy. I. Morphology of the Sagittarius Core and Tidal Arms. *The Astrophysical Journal* **599**, 1082 (2003).

Mann, A. W.; Gaidos, E.; Lépine, S. and Hilton, E. J. They Might Be Giants: Luminosity Class, Planet Occurrence, and Planet-Metallicity Relation of the Coolest Kepler Target Stars. *The Astrophysical Journal* **753**, 90 (2012).

Maraston, C. Evolutionary population synthesis: models, analysis of the ingredients and application to high-z galaxies. MNRAS **362**, 799 (2005).

Margon, B.; Anderson, S. F.; Harris, H. C.; Strauss, M. A.; Knapp, G. R.; Fan, X.; Schneider,

D. P.; Vanden Berk, D. E.; Schlegel, D. J.; Deutsch, E. W.; Ivezić, Ž.; Hall, P. B.; Williams, B. F.; Davidsen, A. F.; Brinkmann, J.; Csabai, I.; Hayes, J. J. E.; Hennessy, G.; Kinney, E. K.; Kleinman, S. J.; Lamb, D. Q.; Long, D.; Neilsen, E. H.; Nichol, R.; Nitta, A.; Snedden, S. A. and York, D. G. Faint High-Latitude Carbon Stars Discovered by the Sloan Digital Sky Survey: Methods and Initial Results. AJ **124**, 1651 (2002).

Marigo, P.; Bressan, a.; Nanni, a.; Girardi, L. and Pumo, M. L. Evolution of thermally pulsing asymptotic giant branch stars - I. The COLIBRI code. *Monthly Notices of the Royal Astronomical Society* **434**, 488 (2013).

Marigo, P. and Girardi, L. Coupling emitted light and chemical yields from stars: A basic constraint to population synthesis models of galaxies. A&A **377**, 132 (2001).

Marigo, P. and Girardi, L. Evolution of asymptotic giant branch stars. I. Updated synthetic TP-AGB models and their basic calibration. A&A **469**, 239 (2007).

Martin, N. F. and Jin, S. The Hercules Satellite: A Stellar Stream in the Milky Way Halo? *The Astrophysical Journal* **721**, 1333 (2010).

Martínez-Delgado, D.; Gallart, C. and Aparicio, A. The Stellar Content of the Local Group Dwarf Galaxy PHOENIX. *Aj* **118**, 862 (1999).

Matsuura, M.; Barlow, M. J.; Zijlstra, A. A.; Whitelock, P. A.; Cioni, M.-R. L.; Groenewegen, M. A. T.; Volk, K.; Kemper, F.; Kodama, T.; Lagadec, E.; Meixner, M.; Sloan, G. C. and Srinivasan, S. The global gas and dust budget of the Large Magellanic Cloud: AGB stars and supernovae, and the impact on the ISM evolution. MNRAS **396**, 918 (2009).

Mauron, N. New observations of cool carbon stars in the halo. *Astronomy and Astrophysics* **482**, 151 (2008).

Mauron, N.; Gigoyan, K. S. and Kendall, T. R. Cool carbon stars in the halo: new very red or distant objects. *Astronomy and Astrophysics* **475**, 843 (2007).

Mauron, N.; Gigoyan, K. S. and Klotz, A. Cool carbon stars in the halo and in dwarf galaxies : H α , colours, and variability. *Astronomy & Astrophysics* **562**, 1 (2014).

McConnachie, A. W. Tthe observed properties of dwarf galaxies in and around the local group. *The Astronomical Journal* p. 4 (2012).

McConnachie, A. W.; Irwin, M. J.; Ibata, R. A.; Dubinski, J.; Widrow, L. M.; Martin, N. F.; Côté, P.; Dotter, A. L.; Navarro, J. F.; Ferguson, A. M. N.; Puzia, T. H.; Lewis, G. F.; Babul, A.; Barmby, P.; Bienaymé, O.; Chapman, S. C.; Cockcroft, R.; Collins, M. L. M.; Fardal, M. A.; Harris, W. E.; Huxor, A.; Mackey, A. D.; Peñarrubia, J.; Rich, R. M.; Richer, H. B.; Siebert, A.; Tanvir, N.; Valls-Gabaud, D. and Venn, K. A. The remnants of galaxy formation from a panoramic survey of the region around M31. Nature **461**, 66 (2009).

McGurk, R. C.; Kimball, A. E. and Ivezić, Ž. Principal Component Analysis of Sloan Digital Sky Survey Stellar Spectra. *The Astronomical Journal* **139**, 1261 (2010).

Melbourne, J. and Boyer, M. L. The contribution of thermally-pulsing asymptotic giant branch and red supergiant stars to the luminosities of the Magellanic Clouds at 1-24 μm. *The Astrophysical Journal* **764**, 30 (2013).

Melbourne, J.; Williams, B. F.; Dalcanton, J. J.; Rosenfield, P.; Girardi, L.; Marigo, P.; Weisz,

D.; Dolphin, A.; Boyer, M. L.; Olsen, K.; Skillman, E. and Seth, A. C. The contribution of TP-AGB and RHeB stars to the near-IR luminosity of Local Group galaxies: Implications for stellar mass measurements of high-redshift galaxies. *The Astrophysical Journal* **748**, 47 (2012).

Menzies, J.; Feast, M.; Whitelock, P.; Olivier, E.; Matsunaga, N. and Da Costa, G. Asymptotic Giant Branch Stars in the Phoenix Dwarf Galaxy. MNRAS **000** (2007).

Menzies, J. W.; Whitelock, P. A. and Feast, M. W. The Local Group Galaxy IC 1613 and its asymptotic giant branch variables. MNRAS **452**, 910 (2015).

Milone, A. P.; Piotto, G.; Bedin, L. R.; Aparicio, A.; Anderson, J.; Sarajedini, A.; Marino, A. F. and Moretti, A. The ACS survey of Galactic globular clusters XII . Photometric binaries along the main sequence. *Astronomy & Astrophysics* **540**, 1 (2012).

Monachesi, A.; Trager, S. C.; Lauer, T. R.; Hidalgo, S. L.; Freedman, W.; Dressler, A.; Grillmair, C. and Mighell, K. J. The Star Formation History of M32. *The Astrophysical Journal* **745**, 97 (2012).

Mouhcine, M. and Lancon, A. Carbon star populations in systems with different metallicities: statistics in Local Group galaxies. *Monthly Notices of the Royal Astronomical Society* **338**, 572 (2003).

Nagao, T.; Maiolino, R. and Marconi, A. Gas metallicity diagnostics in star-forming galaxies. *Astronomy & Astrophysics* **459**, 85 (2006).

Newman, J. A.; Cooper, M. C.; Davis, M.; Faber, S. M.; Coil, A. L.; Guhathakurta, P.; Koo,

D. C.; Phillips, A. C.; Conroy, C.; Dutton, A. A.; Finkbeiner, D. P.; Gerke, B. F.; Rosario, D. J.; Weiner, B. J.; Willmer, C. N. A.; Yan, R.; Harker, J. J.; Kassin, S. A.; Konidaris, N. P.; Lai, K.; Madgwick, D. S.; Noeske, K. G.; Wirth, G. D.; Connolly, A. J.; Kaiser, N.; Kirby, E. N.; Lemaux, B. C.; Lin, L.; Lotz, J. M.; Luppino, G. A.; Marinoni, C.; Matthews, D. J.; Metevier, A. and Schiavon, R. P. The DEEP2 Galaxy Redshift Survey: Design, Observations, Data Reduction, and Redshifts. *The Astrophysical Journal Supplement Series* **208**, 5 (2013).

Nowotny, W.; Aringer, B.; Höfner, S. and Eriksson, K. Synthetic photometry for carbon-rich giants III . Tracing the sequence of mass-losing galactic C-type Miras. *Astronomy & Astrophysics* **552**, 1 (2013).

Nowotny, W.; Aringer, B.; Höfner, S. and Lederer, M. T. Synthetic photometry for carbon-rich giants II . The effects of pulsation and circumstellar dust. *Astronomy & Astrophysics* **129**, 1 (2011).

Nowotny, W.; Kerschbaum, F.; Olofsson, H. and Schwarz, H. E. A census of AGB stars in Local Group galaxies II. NGC 185 and NGC 147. *Astronomy & Astrophysics* **403**, 93 (2003).

Nowotny, W.; Kerschbaum, F.; Schwarz, H. E. and Olofsson, H. A census of AGB stars in Local Group galaxies I . Photometry of a field in M 31. *Astronomy & Astrophysics* **367**, 557 (2001).

Pedregosa, F.; Varoquaux, G.; Gramfort, A.; Michel, V.; Thirion, B.; Grisel, O.; Blondel, M.; Prettenhofer, P.; Weiss, R.; Dubourg, V.; Vanderplas, J.; Passos, A.; Cournapeau, D.; Brucher,

M.; Perrot, M. and Duchesnay, E. Scikit-learn: Machine learning in Python. *Journal of Machine Learning Research* **12**, 2825 (2011).

Pilyugin, L. S. and Thuan, T. X. Oxygen abundance determination in HII regions: The strong line intensities abundance calibration revisited. *The Astrophysical Journal* **631**, 231 (2005).

Probst, R. G.; Gaughan, N.; Abraham, M.; Andrew, J.; Daly, P.; Hileman, E.; Hunten, M.; Liang, M.; Merrill, K. M.; Repp, R. and Shaw, R. Program status of NEWFIRM, the wide-field infrared camera system for the NOAO 4-m telescopes. In Moorwood, A. F. M. and Iye, M., eds., *Ground-based Instrumentation for Astronomy* (2004), vol. 5492 of Proc. SPIE, pp. 1716–1724.

Reid, I. N.; Hawley, S. L. and Gizis, J. E. The Palomar/MSU Nearby-Star Spectroscopic Survey. I. The Northern M Dwarfs - Bandstrengths and Kinematics. *The Astronomical Journal* **110** (1995).

Richer, H. B. and Crabtree, D. R. Luminous Late-Type Stars in a Field of M31. *The Astrophysical Journal* **298**, L13 (1985).

Richer, H. B.; Crabtree, D. R. and Pritchet, C. J. Luminous late-type stars in NGC 205. *The Astrophysical Journal* **287**, 138 (1984).

Riebel, D.; Srinivasan, S.; Sargent, B. and Meixner, M. The Mass-Loss Return From Evolved Stars To the Large Magellanic Cloud. VI. Luminosities and Mass-Loss Rates on Population Scales. *The Astrophysical Journal* **753**, 71 (2012).

Rosenfield, P. and Marigo, P. Evolution of thermally pulsing asymptotic giant branch stars iv.

constraining mass-loss & lifetimes of low mass, low metallicity AGB stars. *The Astrophysical Journal* **790** (2014).

Rowe, J. F.; Richer, H. B.; Brewer, J. P. and Crabtree, D. R. Carbon Stars and Other Luminous Stellar Populations in M33. AJ **129**, 729 (2005).

Rutledge, G. A.; Hesser, J. E.; Stetson, P. B.; Mateo, M.; Simard, L.; Bolte, M.; Friel, E. D. and Copin, Y. Galactic Globular Cluster Metallicity Scale from the Ca II Triplet I. Catalog. PASP **109**, 883 (1997).

Salaris, M.; Weiss, A.; Cassarà, L. P.; Piovan, L. and Chiosi, C. Detailed AGB evolutionary models and near infrared colours of intermediate-age stellar populations : Tests on star clusters. *Astronomy & Astrophysics* (2014).

Sanders, N. E.; Caldwell, N.; McDowell, J. and Harding, P. The metallicity profile of M31 from spectroscopy of hundreds of HII regions and PNe. *The Astrophysical Journal* **758**, 133 (2012).

Schlafly, E. F. and Finkbeiner, D. P. Measuring Reddening with Sloan Digital Sky Survey Stellar Spectra and Recalibrating SFD. *The Astrophysical Journal* **737**, 103 (2011).

Sharma, S.; Johnston, K. V.; Majewski, S. R.; Muñoz, R. R.; Carlberg, J. K. and Bullock, J. Group Finding in the Stellar Halo Using M-giants in the Two Micron All Sky Survey: An Extended View of the Pisces Overdensity? *The Astrophysical Journal* **722**, 750 (2010).

Shetrone, M. D.; Cote, P. and Stetson, P. B. The Nature of the Red Giant Branches in the Ursa Minor and Draco Dwarf Spheroidal Galaxies. PASP **113**, 8 (2001).

Sibbons, L. F.; Ryan, S. G. and Cioni, M. L. The AGB population of NGC 6822 : distribution and the C / M ratio from JHK photometry. *Astronomy & Astrophysics* **540**, 1 (2012).

Sirianni, A. M.; Jee, M. J.; Benítez, N.; Blakeslee, J. P.; Martel, A. R.; Meurer, G.; Clampin, M.; Marchi, G. D.; Ford, H. C.; Gilliland, R.; Hartig, G. F.; Illingworth, G. D.; Mack, J.; Mccann, W. J.; Sirianni, M. and BenÄś, N. The Photometric Performance and Calibration of the Hubble Space Telescope Advanced Camera for Surveys The Photometric Performance and Calibration of the Hubble Space Telescope Advanced Camera for Surveys. *Publications of the Astronomical Society of the Pacific* **117**, 1049 (2005).

Sloan, G. C.; Kraemer, K. E.; Wood, P. R.; Zijlstra, A. A.; Bernard-Salas, J.; Devost, D. and Houck, J. R. The Magellanic Zoo: Mid-Infrared Spitzer Spectroscopy of Evolved Stars and Circumstellar Dust in the Magellanic Clouds. *The Astrophysical Journal* **686**, 1056 (2008).

Sloan, G. C.; Matsuura, M.; Lagadec, E.; van Loon, J. T.; Kraemer, K. E.; McDonald, I.; Groenewegen, M. a. T.; Wood, P. R.; Bernard-Salas, J. and Zijlstra, a. a. Carbon-Rich Dust Production in Metal-Poor Galaxies in the Local Group. *The Astrophysical Journal* **752**, 140 (2012).

Sneden, C.; Ivans, I. I. and Kraft, R. P. Do AGB stars differ chemically from RGB stars in globular clusters ? Mem. Soc. Astron. Italiana **71**, 657 (2000).

Sohn, Y.; Kang, A.; Rhee, J.; Shin, M.; Chun, M. and Kim, H.-i. Near-IR photometry of asymptotic giant branch stars in the dwarf elliptical galaxy NGC 147. *Astronomy & Astrophysics* **445**, 69 (2006).

Srinivasan, S.; Boyer, M. L.; Kemper, F.; Meixner, M.; Sargent, B. A. and Riebel, D. The evolved-star dust budget of the Small Magellanic Cloud: the critical role of a few key players. MNRAS **457**, 2814 (2016).

Srinivasan, S.; Meixner, M.; Leitherer, C.; Vijh, U.; Volk, K.; Blum, R. D.; Babler, B. L.; Block, M.; Bracker, S.; Cohen, M.; Engelbracht, C. W.; For, B.-Q.; Gordon, K. D.; Harris, J.; Hora, J. L.; Indebetouw, R.; Markwick-Kemper, F.; Meade, M.; Misselt, K. A.; Sewilo, M. and Whitney, B. The Mass Loss Return from Evolved Stars to the Large Magellanic Cloud: Empirical Relations for Excess Emission at 8 and 24 μm. AJ **137**, 4810 (2009).

Stanek, K. Z. and Garnavich, P. M. Distance to M31 with the Hubble Space Telescope and HIPPARCOS Red Clump Stars. *The Astrophysical Journal Letters* **503**, L131 (1998).

Starkenburg, E.; Hill, V.; Tolstoy, E.; González Hernández, J.; Irwin, M.; Helmi, A.; Battaglia, G.; Jablonka, P.; Tafelmeyer, M.; Shetrone, M.; Venn, K. and de Boer, T. The NIR Ca II triplet at low metallicity. Searching for extremely low-metallicity stars in classical dwarf galaxies. *Aap* **513**, A34+ (2010).

Stephens, A. W.; Frogel, J. A.; DePoy, D. L.; Freedman, W.; Gallart, C.; Jablonka, P.; Renzini, A.; Rich, R. M. and Davies, R. The stellar content of the bulge of M31. *The Astronomical Journal* **125**, 2473 (2003).

Suda, T. and Fujimoto, M. Y. Evolution of low- and intermediate-mass stars with [Fe/H] <= -2.5. MNRAS **405**, 177 (2010).

S.V., M. The CaII triplet lines as diagnostics of luminosity, metallicity and chromospheric activity in cool stars. *Astronomy & Astrophysics Suplement Series* **124**, 359 (1997).

Tanaka, M.; Chiba, M.; Komiyama, Y.; Guhathakurta, P.; Kalirai, J. S. and Iye, M. Structure and Population of the Andromeda Stellar Halo From a Subaru/Suprime-Cam Survey. *The Astrophysical Journal* **708**, 1168 (2010).

Tinsley, B. M. Stellar lifetimes and abundance ratios in chemical evolution. *The Astrophysical Journal* **229**, 1046 (1979).

Tollerud, E. J.; Beaton, R. L.; Geha, M. C.; Bullock, J. S.; Guhathakurta, P.; Kalirai, J. S.; Majewski, S. R.; Kirby, E. N.; Gilbert, K. M.; Yniguez, B.; Patterson, R. J.; Ostheimer, J. C.; Cooke, J.; Dorman, C. E.; Choudhury, A. and Cooper, M. C. The Splash Survey: Spectroscopy of 15 M31 Dwarf Spheroidal Satellite Galaxies. *The Astrophysical Journal* **752**, 45 (2012).

Tollerud, E. J.; Geha, M. C.; Vargas, L. C. and Bullock, J. S. The Outer Limits of the M31 System: Kinematics of the Dwarf Galaxy Satellites and XXVIII & and XXIX. *The Astrophysical Journal* **768**, 50 (2013).

van Belle, G. T.; Lane, B. F.; Thompson, R. R.; Boden, A. F.; Colavita, M. M.; Dumont, P. J.; Mobley, D. W.; Palmer, D.; Shao, M.; Vasisht, G. X.; Wallace, J. K.; Creech-Eakman, M. J.; Koresko, C. D.; Kulkarni, S. R.; Pan, X. P. and Gubler, J. Radii and Effective Temperatures for G, K, and M Giants and Supergiants. AJ **117**, 521 (1999).

van Loon, J. T.; Cioni, M.-R. L.; Zijlstra, A. A. and Loup, C. An empirical formula for the

mass-loss rates of dust-enshrouded red supergiants and oxygen-rich asymptotic giant branch stars. A&A **438**, 273 (2005).

Vanderplas, J.; Connolly, A.; Ivezić, Ž. and Gray, A. Introduction to astroml: Machine learning for astrophysics. In *Conference on Intelligent Data Understanding (CIDU)* (2012), pp. 47 –54.

Vargas, L. C.; Geha, M. C. and Tollerud, E. J. The distribution of alpha elements in Andromeda dwarf galaxies. *The Astrophysical Journal* **797** (2014).

Veyette, M. J.; Williams, B. F.; Dalcanton, J. J.; Balick, B.; Caldwell, N.; Fouesneau, M.; Girardi, L.; Gordon, K. D.; Kalirai, J.; Rosenfield, P. and Seth, A. C. Panchromatic Hubble Andromeda Treasury. IX. A Photometric Survey of Planetary Nebulae in M31. *The Astrophysical Journal* **792**, 121 (2014).

Villaume, A.; Conroy, C. and Johnson, B. D. Circumstellar Dust around AGB Stars and Implications for Infrared Emission from Galaxies. *The Astrophysical Journal* **806**, 82 (2015).

Weisz, D. R.; Dolphin, A. E.; Skillman, E. D.; Holtzman, J.; Gilbert, K. M.; Dalcanton, J. J. and Williams, B. F. The Star Formation Histories of Local Group Dwarf Galaxies. I. Hubble Space Telescope /Wide Field Planetary Camera 2 Observations. *The Astrophysical Journal* **789**, 147 (2014).

Wenger, M.; Ochsenbein, F.; Egret, D.; Dubois, P.; Bonnarel, F.; Borde, S.; Genova, F.; Jasniewicz, G.; Laloë, S.; Lesteven, S. and Monier, R. The SIMBAD astronomical database. The CDS reference database for astronomical objects. A&AS **143**, 9 (2000).

Whitelock, P. a.; Feast, M. W.; Marang, F. and Groenewegen, M. a. T. Near-infrared photometry of carbon starsĚ. *Monthly Notices of the Royal Astronomical Society* **369**, 751 (2006).

Williams, B. F.; Dalcanton, J. J.; Dolphin, A. E.; Weisz, D. R.; Lewis, A. R.; Lang, D.; Bell, E. F.; Boyer, M. L.; Fouesneau, M.; Gilbert, K. M.; Monachesi, A. and Skillman, E. D. A Global Star Forming Episode in M31 2-4 Gyr Ago. *The Astrophysical Journal* **809**, 22 (2015).

Williams, B. F.; Lang, D.; Dalcanton, J. J.; Dolphin, A. E.; Weisz, D. R.; Bell, E. F.; Bianchi, L.; Byler, N.; Gilbert, K. M.; Girardi, L.; Gordon, K.; Gregersen, D.; Johnson, L. C.; Kalirai, J.; Lauer, T. R.; Monachesi, A.; Rosenfield, P.; Seth, A. and Skillman, E. The Panchromatic Hubble Andromeda Treasury. X. Ultraviolet To Infrared Photometry of 117 Million Equidistant Stars. *The Astrophysical Journal Supplement Series* **215**, 9 (2014).

Wing, R. F. A new system of narrow-band infrared photometry for late-type stars. *Contributions from the Kitt Peak National Observatory* **554**, 145 (1971).

Wing, R. F. Recognition and Classification of AGB Stars by Narrow-Band TiO / CN Photometry. In *Why Galaxies Care About AGB Stars* (2007), vol. 378, pp. 92–97.

Woods, P. M.; Oliveira, J. M.; Kemper, F.; van Loon, J. T.; Sargent, B. a.; Matsuura, M.; Szczerba, R.; Volk, K.; Zijlstra, a. a.; Sloan, G. C.; Lagadec, E.; McDonald, I.; Jones, O.; Gorjian, V.; Kraemer, K. E.; Gielen, C.; Meixner, M.; Blum, R. D.; SewiÅĆo, M.; Riebel, D.; Shiao, B.; Chen, C.-H. R.; Boyer, M. L.; Indebetouw, R.; Antoniou, V.; Bernard, J.-P.; Cohen, M.; Dijkstra, C.; Galametz, M.; Galliano, F.; Gordon, K. D.; Harris, J.; Hony,

S.; Hora, J. L.; Kawamura, a.; Lawton, B.; Leisenring, J. M.; Madden, S.; Marengo, M.; McGuire, C.; Mulia, a. J.; OâĂŹHalloran, B.; Olsen, K.; Paladini, R.; Paradis, D.; Reach, W. T.; Rubin, D.; Sandstrom, K.; SoszyÅĎski, I.; Speck, a. K.; Srinivasan, S.; Tielens, a. G. G. M.; van Aarle, E.; Van Dyk, S. D.; Van Winckel, H.; Vijh, U. P.; Whitney, B. and Wilkins, a. N. The SAGE-Spec Spitzer Legacy programme: the life-cycle of dust and gas in the Large Magellanic Cloud - Point source classification I. *Monthly Notices of the Royal Astronomical Society* **411**, 1597 (2011).

Yip, C. W.; Connolly, A. J.; Berk, D. E. V.; Ma, Z.; Frieman, J. A.; Subbarao, M.; Szalay, A. S.; Richards, G. T.; Hall, P. B.; Schneider, D. P.; Hopkins, A. M.; Trump, J. and Brinkmann, J. Spectral classification of quasars in the Sloan Digital Sky Survey: Eigenspectra, redshift, and luminosity effects. *The Astronomical Journal* **128**, 2603 (2004).

Zaritsky, D.; Kennicutt, R. C. and Huchra, J. P. HII Regions and the Abundance Properties of Spiral Galaxies. *The Astrophysical Journal* **420**, 87 (1994).

Zhong, J.; Lépine, S.; Li, J.; Chen, L.; Hou, J.-L.; Yang, M.; Li, G.-W.; Zhang, Y. and Hou, Y.-H. M-giant star candidates identified in LAMOST DR 1. *Research in Astronomy and Astrophysics* **15**, 1154 (2015).

Zucker, D. B.; Kniazev, A. Y.; Martínez-Delgado, D.; Bell, E. F.; Rix, H.-W.; Grebel, E. K.; Holtzman, J. A.; Walterbos, R. A. M.; Rockosi, C. M.; York, D. G.; Barentine, J. C.; Brewington, H.; Brinkmann, J.; Harvanek, M.; Kleinman, S. J.; Krzesinski, J.; Long, D.; Neilsen, Jr., E. H.; Nitta, A. and Snedden, S. A. Andromeda X, a New Dwarf Spheroidal Satellite of M31: Photometry. *The Astrophysical Journal Letters* **659**, L21 (2007).